Circuits and Passive Components for Radio-Frequency Power Conversion

by

Yehui Han

B.S., Tsinghua University (2000)

M.S., Tsinghua University (2002)

Submitted to the Department of Electrical Engineering and Computer Science
in partial fulfillment of the requirements for the degree of

Doctor of Philosophy

at the

MASSACHUSETTS INSTITUTE OF TECHNOLOGY

February 2010

Author_____
Department of Electrical Engineering and Computer Science
December 21, 2009

Certified by_____
David J. Perreault
Associate Professor of Electrical Engineering
Thesis Supervisor

Accepted by_____
Terry Orlando
Chairman, Department Committee on Graduate Students

Circuits and Passive Components for Radio-Frequency Power Conversion

by
Yehui Han

Submitted to the Department of Electrical Engineering and Computer Science
on December 21, 2009, in partial fulfillment of the
requirements for the degree of
Doctor of Science

Abstract

THIS THESIS focuses on developing technology for high efficiency power converters operating at very high frequencies. The work in the thesis involves two aspects of such converters: rf (radio-frequency) power circuit design techniques and magnetic material characterization and application. In the aspect of circuit design techniques, the thesis investigates a new class of matching networks that overcomes a major limitation of rf converter circuits - their high sensitivity to loading condition. These networks, which are termed resistance compression networks, serve to substantially decrease the variation in effective resistance seen by a tuned rf inverter as loading conditions change. The thesis explores the operation, performance characteristics, and design of these networks, and present experimental results demonstrating their performance. The thesis also presents analysis and design considerations for lumped (inductor and capacitor) matching networks operating at high efficiency ($> 95\%$). Formulas for calculating matching network efficiency are given and used to evaluate the optimum number of matching stages as a function of conversion ratio. Both simulation and experimental results are presented that validate the analytical formulation.

In the aspect of magnetic materials and applications, the thesis investigates the loss characteristics of several commercial rf magnetic materials for power conversion applications in the 10 MHz to 100 MHz range. A measurement method is proposed to identify loss characteristics of different commercial rf magnetic core materials. The loss characteristics of these materials, which have not previously been available, are illustrated and compared in tables and figures. Based on results in characterization of magnetic materials, the thesis describes a procedure for magnetic components design with low permeability magnetic materials that is for very high frequency power conversion applications. This procedure provides a method to compare and evaluate different magnetic materials for given specifications of a magnetic-core inductor. Some important information, e.g. quality factor and size of the inductor can be predicted before the final design. The thesis also investigates some problems such as optimization of a magnetic-core inductor.

Thesis Supervisor: David J. Perreault
Title: Associate Professor of Electrical Engineering

Dedication

To Xin Wang

Acknowledgements

I still remember the first day I came to MIT six years ago. In a rainy afternoon, I was led by Marilyn Pierce, our graduate administrator, walked through the underground maze from the building 38 to building 10, and met my thesis advisor, Prof. David Perreault, in his office. At that time, facing a totally different environment, I was afraid of not only getting lost at MIT buildings, but also getting lost of the direction of my PhD study. Dave's great enthusiasm, tremendous knowledge and wonderful ideas in power electronics led me walk through the maze and helped me to continue my career in academics. I feel extremely blessed to be working with such a caring advisor. I want to thank Dave for his guidance, patience and support during this academic journey.

I would like to thank my thesis committee: Prof. John Kassakian, Prof. Steve Leeb, and Prof. Charlie Sullivan. This thesis would not have been possible without their advice and support. I would also like to thank Prof. Tomas Palacios, who gave me a lot of knowledge about compound devices, and Prof. Markus Zahn, who lent his Ansoft software to me.

Many thanks go to my sponsors who made this thesis possible: DARPA, General Electric, Sheila and Emmanuel Landsman, National Science Foundation, National Semiconductor, the MIT Automotive Consortium, and the MIT Center for Integrated Circuits and Systems (CICS).

I would like to show my gratitude to alumni, students and staff from LEES and our group including Al-Thaddeus Avestruz, Grace Cheung, David Giuliano, Jingying Hu, David Jackson, Olivia Leitermann, Wei Li, Vivan Mizuno, Timothy Neugebauer, Joshua Phinney, Brandon Pierquet, Robert Pilawa, Yihui Qiu, Juan Rivas, Wayne Ryan, Anthony Sagneri, Riccardo Signorelli, Makiko Wada, Jiankang Wang, and many others.

Thanks to students that took 6.334 during the spring semesters of 2004, 2006 and 2007.

Thanks to my colleagues at MIT and Tsinghua University and my friends in America and China. I would like to single out for special thanks Guang Han, roommate in college, best man at my wedding, and a great engineer.

Finally, I owe my deepest gratitude to my parents. I would not be where I am today, without their love, encouragement and support. It is my wife Xin Wang that this thesis is dedicated. I am grateful to express my gratitude to her that has been with me throughout this academic journey, providing love, support, and joyful company.

Contents

List of Figures

List of Tables

Chapter 1

Introduction

1.1 Background and Motivations

A PRINCIPAL means for improving performance and reducing the size of power electronics is through increasing the switching frequency. An increased switching frequency can lower the requirement of passive components for a certain power level, and both the value and size of passive components may be reduced [3]. Resonant dc/dc power converters enable much higher switching frequencies than can be achieved with conventional pulse-width modulated circuits, due to their natural soft-switched operation and ability to absorb and utilize circuit parasitics in the conversion process. For example, efficient resonant dc/dc power conversion has been demonstrated at frequencies in excess of 100 MHz, and operation at much higher switching frequencies is clearly feasible [4–7]. Further development of resonant power converter technology is thus of great potential value.

Figure 1.1 shows a basic structure for a high-frequency resonant dc/dc converter, comprising an inverter stage, a transformation stage, and a rectifier stage [4,5,8–15]. The inverter stage draws dc input power and delivers ac power to the transformation stage. Inverters suitable for extremely high frequencies operate resonantly, and take advantage of the characteristics of the load to achieve zero-voltage switching (ZVS) of the semiconductor device(s) [16–23].

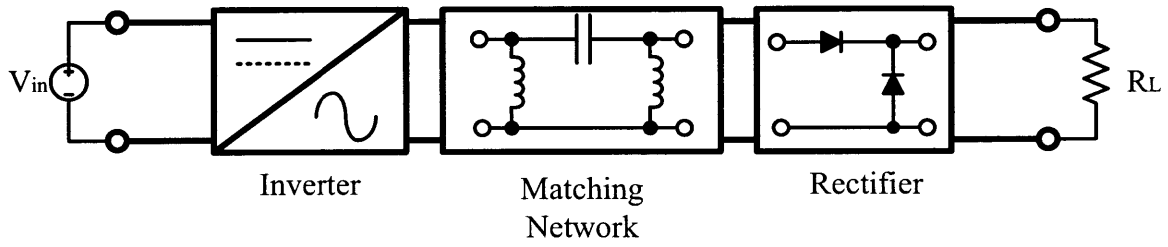

Figure 1.1: Structure of the power stage of a resonant dc/dc converter. The converter comprises an inverter (dc/ac) circuit, a transformation/matching circuit, and a rectifier (ac/dc) circuit.

The rectifier stage takes ac power from the transformation stage and delivers dc power to the output. In addition to conventional rectifier topologies, resonant converters can take advantage of a variety of resonant rectifiers (e.g. [24,25]). The system may be designed such that the rectifier stage appears resistive in a describing function sense (e.g., [4, 15, 24, 25]) and is matched to the inverter by the action of the transformation stage.

Depending on the details of the converter design, the functions of the transformation stage may include matching impedances, transforming voltage and current, providing electrical isolation and providing filtering. For some high-frequency resonant inverter topologies which are highly sensitive to loading conditions, the transformation may also serve to reduce the load sensitivity of the resonant inverter [26, 27]. The transformation stage can be realized using conventional transformers and/or resonant transformers [28], transmission-line transformers [29–31], matching networks [32–34], or other similar means. In realizing these functions, a transformation circuit should ideally have a high efficiency ($> 90\%$), require fewer passive components and have a small profile.

Power or output control of resonant converters can be achieved through a number of means, including frequency modulation [8,10], on/off control [4,6,7,35–43], and extensions of these techniques [4, 35, 44]. Fixed-frequency control techniques are preferable for systems using resonant gating [4, 36, 37, 39, 40, 45] and in circuit implementations with high-order tuned tanks or narrow-band transformation stages. This thesis focuses primarily on designs with fixed-frequency on/off control operation.

Resonant converters utilize magnetic components (inductors and transformers) to realize intermediate energy storage, impedance transformation, soft switching, resonant rectification, and filtering. These magnetic components are operating at high flux levels, and often under large flux swings. Moreover, it would be desirable to have improved magnetic components for rf circuits such as matching networks [32–34, 46, 47].There is thus a need for magnetic materials and components suitable for operation under high flux swings at frequencies above 10 MHz. Small, high efficiency magnetic components are required to realize rf power converters, and there is a particular need to achieve high quality factor at radio frequencies for resonant magnetic elements.

1.2 Challenges of Radio-Frequency Power Conversion

The subject of this thesis is the miniaturization of power electronics. Increasing switching frequency dramatically is a substantial means to improve size and performance of power electronics systems. However, the switching frequency is difficult to increase because there

are many challenging issues in aspects of circuit design and passive components, especially magnetics. These challenges are outlined in this section.

A major limitation of resonant converter circuits is the sensitivity of the inverter stage to the variations of load. It has been reported that switched-mode rf inverters suitable for ultra-high frequencies (e.g., classes DE, E, F, Φ and so forth) are highly sensitive to the effective impedance of the load. For example, conventional class E inverters only operate under the desired ZVS condition over about a factor of two in load resistance [26,27]. While acceptable in communications applications (in which the load resistance is relatively constant), this is problematic for many dc-dc power converter applications, where the effective resistance [15] presented by the matching stage and rectifier varies greatly with input/output voltage and current. This problem is particularly severe in applications in which the voltage conversion ratio varies substantially; such applications include charging systems where the converter must deliver constant power over a wide output voltage range and regulating converters where the converter must operate over a wide input voltage range. This thesis introduces a new circuit technique that overcomes one of the major limitations of resonant dc/dc converters at extremely high frequencies, and expands the range of applications for which resonant conversion is effective.

A matching network is a passive two-port circuit designed to provide narrow-band impedance, current and voltage transformation between the two ports. While most widely associated with communications applications [32, 33, 46], matching networks also find useful application in resonant inverters, rectifiers, and dc-dc converters. Most analytical descriptions of matching networks are based on the assumption of no loss. Where efficiency is considered [4], it is typically treated as secondary to other performance goals, in accordance with the needs of communications applications. Moreover, literature focusing on the design of matching networks for very high efficiencies (e.g., 95%) appears to be lacking. In the thesis, the author presents analysis and design considerations for high efficiency ($> 95\%$) lumped-element matching networks.

While coreless magnetics can be used at rf frequencies [47], cored magnetics offer the possibility of smaller size and better shielding. High frequency, low loss magnetic materials are thus of great potential value. Unfortunately, most magnetic materials exhibit unacceptably high losses at frequencies above a few Megahertz. Good rf magnetic materials, however, are not common. Moreover, the few available bulk magnetic materials which are potentially suitable for frequencies above 10 MHz are typically only characterized for small-signal drive conditions, and not under the high flux-density conditions desired for power electronics. In particular, there is a lack of information about core loss characteristics at high flux swing for such materials. This motivates better characterization of magnetic materials for high frequency power conversion applications.

Besides of characterization of magnetic materials, it appears to be lacking of a fast and convenient inductor design procedure with low permeability magnetic material. For the same design specification, different magnetic materials may be operating under different ac flux density and their permeability and loss characteristics are significantly different. Without a fast and convenient design procedure, an individual inductor has to be designed for each magnetic material and each available core size before their final performance can be compared. If there are hundreds of material core size combinations available, there will be a lot work for the designer.

1.3 Thesis Objectives and Contributions

The thesis mainly focuses on developing technology for high efficiency power converters operating at very high frequencies. The research work in the thesis involves two aspects of such converters: rf power circuit design techniques and magnetic material characterization and application. In the aspect of circuit design techniques, the author investigates a new class of matching networks that greatly reduces the load sensitivity of resonant inverters and rf power amplifiers. These networks, which are termed resistance compression networks, serve to substantially decrease the variation in effective resistance seen by a tuned rf inverter as loading conditions change. Compression networks ideally act without loss, such that all energy provided at the input port is transformed and transferred to the resistive load. Although resistance compression networks are a kind of matching network and can provide impedance transformation, the main purpose of these networks is for compressing the effective load resistance range as operating conditions vary. This effect can be used to overcome one of the major deficiencies of tuned rf circuits for power applications and expand the range of applications for which high-frequency resonant power conversion is viable. In the thesis, the author explores the operation, performance characteristics, and design of these networks, and presents experimental results demonstrating their performance. Their combination with rectifiers to form rf-to-dc converters having narrow-range resistive input characteristics is also treated. The application of resistance compression in resonant power conversion is demonstrated in a dc-dc power converter operating at 100 MHz.

The use and limitations of matching networks to realize voltage and current transformation in resonant circuits is also explored. Formulas for calculating matching network efficiency are developed and it is shown that matching network efficiency can be expressed as a function of inductor quality factor, capacitor quality factor, and transformation ratio. The thesis also introduces formulas used to evaluate the optimum number of L-section matching stages as a function of conversion ratio. Both simulation and experimental results are presented that validate the analytical formulation.

In the aspect of magnetic materials and applications, the author investigates the measurement, evaluation and characterization of different commercial rf frequency magnetic materials. As part of this, an experimental method is proposed to characterize the loss properties of rf magnetic materials under large-signal ac flux conditions for frequencies above 10 MHz. This method is applied to evaluate the loss characteristics of a number of commercially available rf magnetic materials at high flux densities and frequencies, yielding important design information which was not previously available.

The author proposes an inductor design procedure with commercial low permeability magnetic cores. This method is based on Steinmetz parameters extracted in characterization of magnetic materials. This procedure is particularly suited for very high frequency inductor design. By this procedure, different magnetic materials are compared fairly and conveniently, and both the quality factor and the size of a magnetic-core inductor can be evaluated before the final design. Some problems, such as the size scaling and optimization of a magnetic-core inductor are also investigated.

1.4 Organization of Thesis

Chapter 2 describes the general attributes of resistance compression networks for radio frequency power conversion. The operation, performance, and design of these networks are explored and experimental results are presented to confirm their performance. To demonstrate the use of resistance compression to benefit very high frequency dc-dc power converters, a prototype dc-dc converter operating at 100 MHz was developed by the author and colleagues [2, 26, 27, 38, 39]. The author also considers other behavior of resistance compression networks in this chapter, including "phase compression" of the load impedance.

Chapter 3 presents analysis and design considerations for lumped (inductor and capacitor) matching networks operating at high efficiency (95%). Formulas for calculating matching network efficiency are given, and it is shown that efficiency can be expressed as a function of inductor quality factor, capacitor quality factor, and transformation ratio. These formulas are used to evaluate the optimum number of L-section matching stages as a function of conversion ratio. Both simulation and experimental results are presented that validate the analytical formulation.

Chapter 4 investigates the loss characteristics of several commercial rf magnetic materials for power conversion applications in the 10 MHz to 100 MHz range. A measurement method is proposed that provides a direct measurement of inductor quality factor Q_L as a function of inductor current at rf frequencies, and enables indirect calculation of core loss as a function

of flux density. Possible sources of error in measurement and calculation are evaluated and addressed. The proposed method is used to identify loss characteristics of different commercial rf magnetic core materials. The loss characteristics of these materials, which have not previously been available, are illustrated and compared in tables and figures. The use of the method and data are demonstrated in the design of a magnetic-core inductor, which is applied in a 30 MHz inverter. The results of this chapter are thus useful for design of magnetic components for very high frequency (VHF) applications.

Chapter 5 presents an inductor design procedure for inductors with ungapped low-permea -bility cores that is based on Steinmetz parameters of magnetic materials. With this procedure, different magnetic materials are compared fairly and fast, and both the quality factor Q_L and the size of a magnetic-core inductor can be predicted before the final design. Some problems, such as optimization of magnetic-core inductors are also investigated.

Finally, Chapter 6 concludes the whole thesis and give suggestions about future work in this area.

Chapter 2

Resistance Compression Networks for Radio-Frequency Power Conversion

A LIMITATION of many high-frequency resonant inverter topologies is their high sensitivity to loading conditions. This chapter introduces a new class of matching networks that greatly reduces the load sensitivity of resonant inverters and radio frequency power amplifiers. These networks, which are termed resistance compression networks, serve to substantially decrease the variation in effective resistance seen by a tuned rf inverter as loading conditions change. We explore the operation, performance characteristics, and design of these networks, and present experimental results demonstrating their performance. Their combination with rectifiers to form rf-to-dc converters having narrow-range resistive input characteristics is also treated. The application of resistance compression in resonant power conversion is demonstrated in a dc/dc power converter operating at 100 MHz.

2.1 Background

A major limitation of resonant converter circuits is the sensitivity of the inverter stage to loading conditions. Switched-mode rf inverters suitable for extreme high frequencies (e.g., classes DE, E, F, Φ, and so forth) exhibit high sensitivity to the effective impedance of the load. For example, conventional class E inverters only operate under soft switched conditions over about a factor of two in load resistance. While acceptable in communications applications (in which the load resistance is relatively constant), this is problematic for many dc/dc power converter applications, where the effective resistance presented by the matching stage and rectifier varies greatly with output voltage and current (e.g., [15]). This problem is particularly severe in applications in which the voltage conversion ratio varies substantially; such applications include charging systems where the converter must deliver constant power over a wide output voltage range and regulating converters where the converter must operate over a wide input voltage range and/or the same converter design must be capable of supporting a range of output voltages.

This chapter introduces a new class of matching/transformation networks that greatly reduce the load sensitivity of tuned rf power inverters. These networks, which are termed resistance compression networks, serve to greatly reduce the variation in effective resistance seen by a tuned rf inverter as loading conditions change.

Compression networks ideally act without loss, such that all energy provided at the input port is transformed and transferred to the resistive load. In effect, the load resistance range appears compressed when looking through a resistance compression network. This effect can be used to overcome one of the major deficiencies of tuned radio-frequency circuits for power applications and expand the range of applications for which high-frequency resonant power conversion is viable.

Section 2.2 of the chapter introduces resistance compression networks, including their fundamental principles of operation and performance characteristics. Experimental results demonstrating their performance are also presented. Section 2.3 shows how resistance compression networks can be paired with appropriate rectifiers to yield high-performance rf-to-dc converters with resistive input characteristics. Section 2.4 addresses design considerations for resistance compression networks and resistance compressed rectifiers. Application of this approach to the design of a 100 MHz dc/dc power converter is presented in Section 2.5. Section 2.6 considers the behavior of the compression networks when the (matched) load impedances are not purely resistive and illustrates "phase compression" effect of the load impedance. Section 2.7 concludes the chapter.

2.2 Resistance Compression Networks

Here we introduces circuits that provide the previously described resistance compression effect. These circuits operate on two matched load resistances whose resistance values, while equal, may vary over a large range. As will be shown in Section 2.3, a variety of rectifier topologies can be modeled as such a matched resistor pair.

Two simple linear circuits of this class that exhibit resistance compression characteristics are illustrated in Fig. 2.1. When either of these circuits is driven at the resonant frequency $\omega_0 = \frac{1}{\sqrt{LC}}$, of its LC tank, it presents a resistive input impedance R_{in} that varies only a small amount as the *matched* load resistances R vary across a wide range. For example, for the circuit of Fig. 2.1(a), the input resistance is:

$$R_{in} = \frac{2R}{1 + \left(\frac{R}{Z_0}\right)^2} \tag{2.1}$$

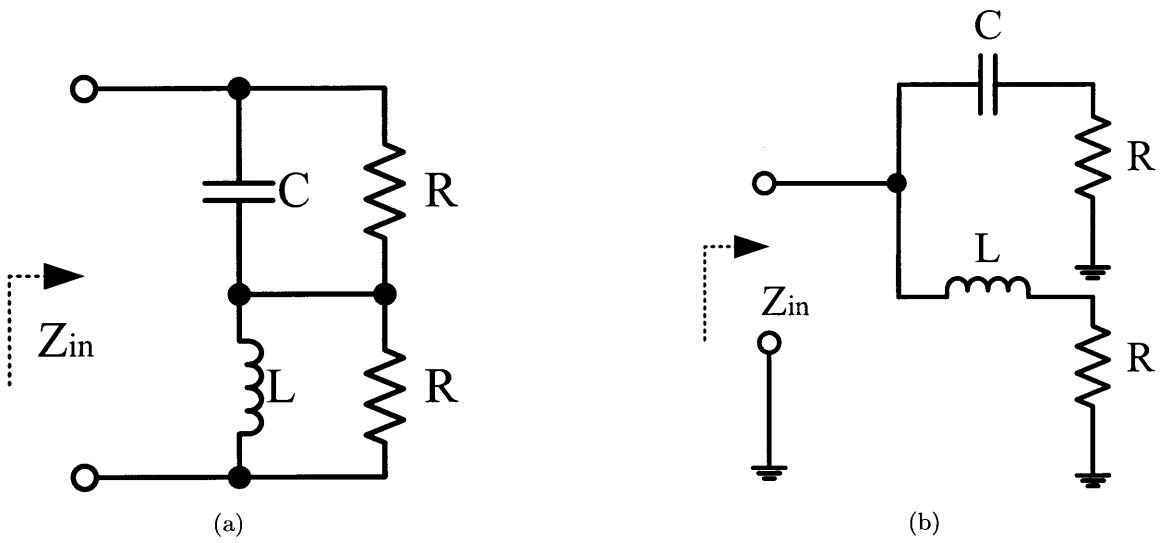

Figure 2.1: Resistance compression circuits. Each of these circuits provides a compression in apparent input resistance. At the resonant frequency of the LC tank the input resistance R_{in} varies over a narrow range as the matched resistors R vary over a wide range (geometrically centered on the tank characteristic impedance). The circuits achieve lossless energy transfer from the input port to the resistors R.

Table 2.1: Characteristics of the resistance compression network of Fig. 2.1(a).

Ratio of R range	Range of R	Ratio of R_{in} range	Range of R_{in}
100 : 1	$0.1Z_0$ to $10Z_0$	5.05 : 1	$0.198Z_0$ to Z_0
10 : 1	$0.316Z_0$ to $3.16Z_0$	1.74 : 1	$0.575Z_0$ to Z_0
4 : 1	$0.5Z_0$ to $2Z_0$	1.25 : 1	$0.8Z_0$ to Z_0
2 : 1	$0.707Z_0$ to $1.41Z_0$	1.06 : 1	$0.94Z_0$ to Z_0

in which $Z_0 = \sqrt{\frac{L}{C}}$ is the characteristic impedance of the tank. For variations of R over a range having a geometric mean of Z_0 (that is, $R \epsilon \left[\frac{Z_0}{c}, cZ_0\right]$, where c is a constant that defines the span of the resistance range) the variation in input resistance R_{in} is smaller than the variation in load resistance R. The amount of "compression" that is achieved for this case (around a center value of impedance $Z_c = Z_0$) is illustrated in Table 2.1. For example, a 100 : 1 variation in R around the center value results in only a 5.05 : 1 variation in R_{in}, and a 10 : 1 variation in load resistance results in a modest 1.74 : 1 variation in R_{in}. Furthermore, because the reactive components are ideally lossless, all energy driven into the resistive input of the compression network is transformed in voltage and transferred to the load resistors. Thus, the compression network can efficiently function to match a source to the load resistors, despite large (but identical) variations in the load resistors.

For the circuit of Fig. 2.1(b), the input resistance at resonance is:

$$R_{in} = \frac{Z_0^2}{2R}\left[1 + \left(\frac{R}{Z_0}\right)^2\right] \tag{2.2}$$

which represents the same degree of compression as R varies about Z_0.

More generally, the compression networks of Fig. 2.1 may be designed with generalized reactive branch networks as shown in Fig. 2.2. The reactive branch networks in Fig. 2.2 are designed to have the specified reactance X at the designed operating frequency. For example, at this frequency the input impedance of the network in Fig. 2.1(a) will be resistive with a value:

$$R_{in} = \frac{2R}{1 + \left(\frac{R}{X}\right)^2} \tag{2.3}$$

which provides compression of the matched load resistances about a center value of impedance $Z_c = X$. The impedances of these branches at other frequencies of interest (e.g. dc or at harmonic frequencies) can be controlled by how the branch reactances are implemented. Likewise, the resistance for the network of Fig. 2.1(b) will be:

$$R_{in} = \frac{X^2}{2R}\left[1 + \left(\frac{R}{X}\right)^2\right] \tag{2.4}$$

Considerations regarding implementation of the branch networks are addressed in Section 2.4.

It should be noted that these networks can be cascaded to achieve even higher levels of resistance compression. For example, the resistances R in Fig. 2.2 can each represent the input resistance of subsequent resistance compression stage. An *"N-stage"* compression network would thus ideally have 2^N load resistances that vary in a matched fashion. However, the efficacy of many-stage compression is likely to be limited by a variety of practical considerations.

Figure 2.3 shows simulated and experimental results from a compression network of the type shown in Fig. 2.1(a) with component values shown in Table 2.2. The network has a resonant frequency of 85.15 MHz and a characteristic impedance of 57.35 Ω (slightly lower than nominal due to small additional parasitics). The anticipated compression in input resistance is achieved, and in all cases the measured reactive impedance at the operating frequency is negligible. The compression network of Fig. 2.2(b) is the network dual of that shown in Fig. 2.2(a). In the network of Fig. 2.2(b), the input and load resistors share a common ground, which can be useful in applications such as the one developed in Section 2.5.

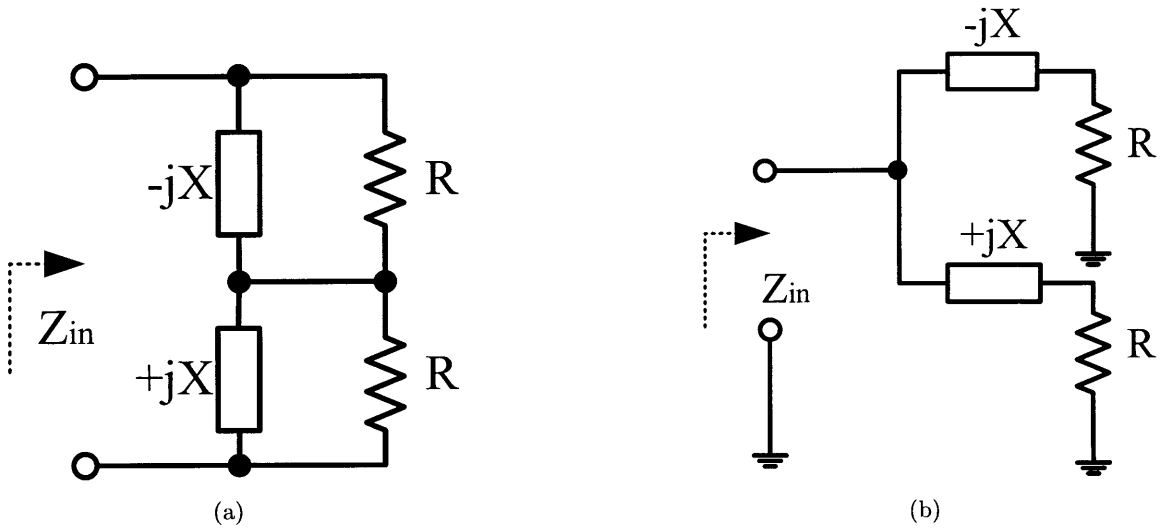

Figure 2.2: Structure of the two basic resistance compression networks introduced in the chapter. The impedance of the reactive networks is specified at the desired operating frequency. Implementation of the reactive networks may be selected to provide desired characteristics at frequencies away from the operating frequency.

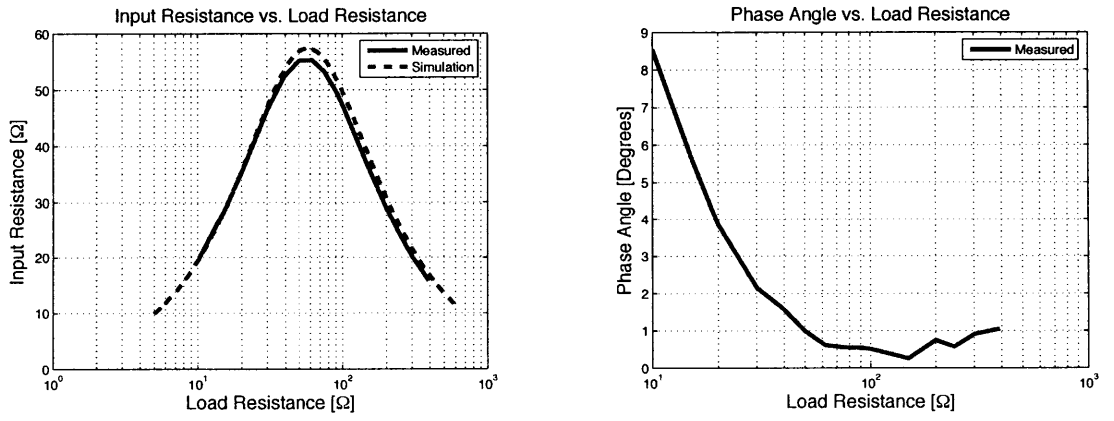

(a) Input Resistance $\Re e\{Z_{in}\}$ vs. R

(b) Phase Angle of the Input Impedance vs. R

Figure 2.3: Magnitude of the input resistance $\Re\{Z_{in}\}$ and phase of the input impedance (experimental and simulated) of the compression network shown in Fig. 2.1(a) as a function of R. L is a Coilcraft 100 nH coreless inductor plus 7.2 nH of parasitic inductance while C is a 33 pF mica capacitor. Measurements made at 85.15 MHz.

Table 2.2: Components used to obtain data in Fig. 2.3.

Component Name	Nominal Value	Manufacturer and Part Style	Part Number
C	33 pF	CDE Chip Mica 100 V	MC08FA330J
L	100 nH	Coilcraft	1812SMS-R10

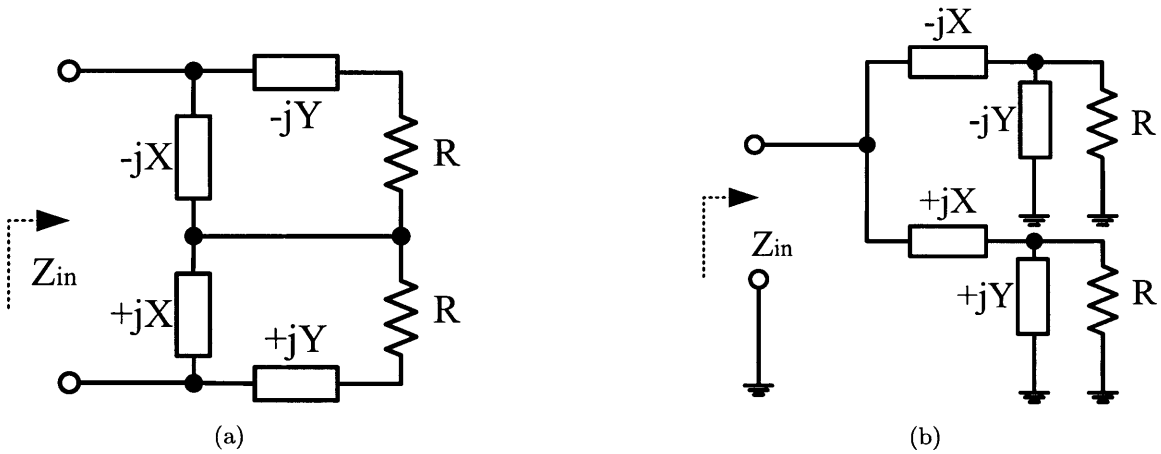

Figure 2.4: Four element compression networks. These networks can provide both resistance compression and impedance transformation.

The networks of Fig. 2.2 provide resistance compression about a specified value. In many applications where resistance compression is useful, a transformation in the center value of the impedance is also desirable. These functions can be combined in a higher-order compression network. Figure 2.4 shows two structures of four element compression / transformation networks. These networks can be designed to achieve both resistance compression and transformation of the resistance up or down by an amount only limited by efficiency requirements, component quality factor, and precision. As with the two-element networks, the input impedance remains entirely resistive over the whole load-resistance range.

Four-element resistance compression networks provide an additional degree of design freedom that can be used to implement resistance transformation along with resistance compression. Consider the four-element compression network of Fig. 2.4(a), where the values X and Y are the reactances of the network branches at the desired operating frequency. Straightforward analysis shows that the input impedance of this network at the specified

frequency is resistive, with a value

$$R_{in} = \frac{X^2}{(X+Y)^2} \cdot \frac{2R}{1+\left(\frac{R}{X+Y}\right)^2} \tag{2.5}$$

Examining this equation we can identify a center impedance $Z_c = X + Y$ about which compression of the matched resistances occurs. Moreover, we can identify a transformation factor K_T, defined as:

$$K_T = \frac{X^2}{(X+Y)^2} \tag{2.6}$$

K_T can be observed to be an additional factor by which the input impedance R_{in} is scaled (transformed) as compared to the two element matching network of Fig. 2.2(a). That is,

$$K_T = \left.\frac{R_{in}}{Z_c}\right|_{R=Z_c} \tag{2.7}$$

There are two distinct possibilities with this four element matching network. If reactances X and Y have the same sign (that is, both reactances are inductive or both are capacitive at the operating frequency) then K_T will be less than one, and there will be a downward transformation from Z_c to R_{in}. Conversely, if X and Y have opposite sign (one is inductive and the other capacitive) K_T will be greater than one, and there will be an upward impedance transformation from Z_c to R_{in}.

The four element compression network of Fig. 2.4(b) can similarly provide transformation along with compression. In particular the input resistance presented by this network is:

$$R_{in} = \frac{1}{2R} \cdot X^2 \cdot \left[1+\left(\frac{R}{X \parallel Y}\right)^2\right] \tag{2.8}$$

The center impedance about which compression will occur is $Z_c = X \parallel Y$. The transformation ratio K_T is:

$$K_T = \frac{X^2}{(X \parallel Y)^2} \tag{2.9}$$

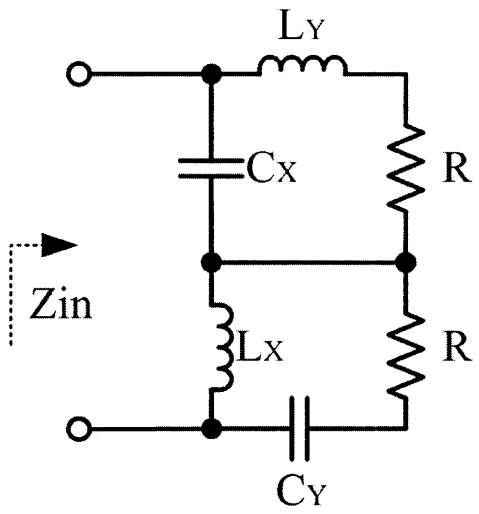

Figure 2.5: Four element compression network used to obtain experimental data. Layout of this circuit is illustrated in Appendix A.

Figure 2.7 shows simulation and experimental measurement of a four element impedance compression network operating at a frequency of 97.4 MHz which provides both compression and transformation (Fig. 2.6, Table 2.3). The load resistance is swept between 5 Ω and 500 Ω and presents a resistive input impedance over the whole range that varies between 50 Ω and 290 Ω[1].

In practice, the resistors loading the compression network may not be perfectly matched. Consider the resistance compression network circuit in Fig. 2.8. The load resistors are

[1]The author's colleague Olivia Leitermann performed the layout of the PCB, built the prototype and carried out the measurements.

Table 2.3: Components used to obtain data in Fig. 2.7.

Component Name	Nominal Value	Manufacturer and Part Style	Part Number
C_X	15 pF	CDE Chip Mica 100 V	MC08EA150J
C_Y	8 pF +2 pF +1 pF	CDE Chip Mica 100 V	MC08CA080C MC08CA020D MC08CA010D
L_X	169 nH	Coilcraft	132-12SM-12
L_Y	246 nH	Coilcraft	132-15SM-15

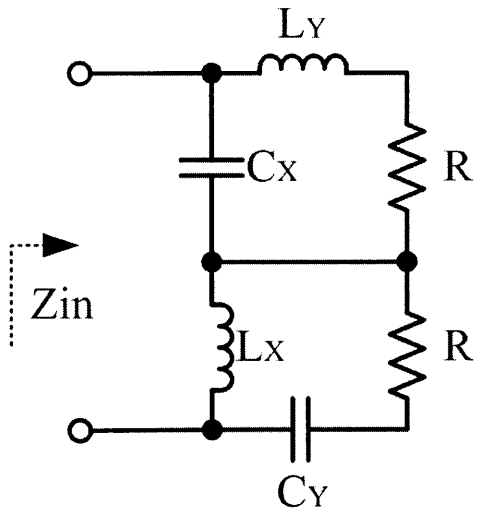

Figure 2.6: Four element compression network used to obtain experimental data. Layout of this circuit is illustrated in Appendix A.

mismatched by $2\Delta R$. Assuming $\Delta R \ll R$ and ignoring higher order ΔR terms, the input impedance Z_{in} is:

$$Z_{in} = |Z_{in}|\angle\theta = \frac{2R}{1+\left(\frac{R}{X}\right)^2} + j\frac{4RX^3}{\left(R^2+X^2\right)^2}\Delta R \tag{2.10}$$

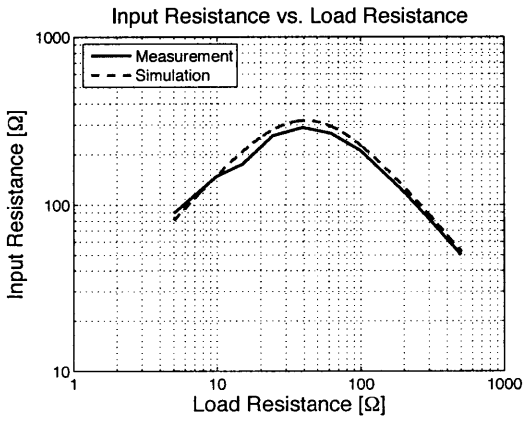

(a) Input Resistance ($\Re\{Z_{in}\}$) vs. R

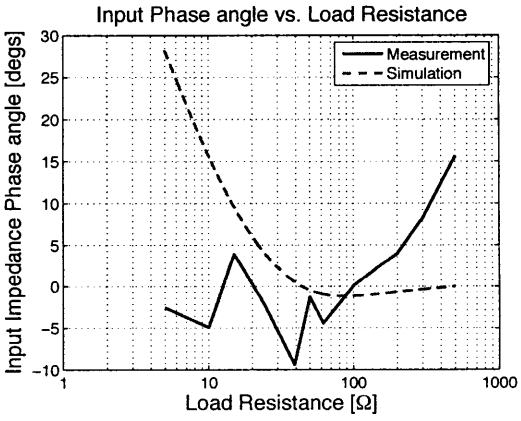

(b) Phase Angle of the Input Impedance vs. R

Figure 2.7: Input resistance ($\Re\{Z_{in}\}$) and impedance phase (experimental and simulated) of the four element compression network shown in Fig. 2.6 as a function of R. $C_X = 15$ pF, $L_X = 169$ nH, $C_Y = 11$ pF, $L_Y = 246$ nH; measurements made at 97.4 MHz.

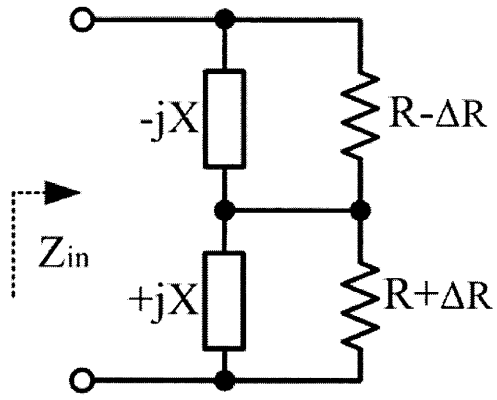

Figure 2.8: A resistance compression network with unequal loads. The load resistors are mismatched by $2\Delta R$, assuming $\Delta R \ll R$.

The magnitude and phase of the input impedance Z_{in} are:

$$|Z_{in}| = \frac{2R}{1+\left(\frac{R}{X}\right)^2}[1+\frac{2X^2}{(R^2+X^2)^2}\Delta R^2] \tag{2.11}$$

$$\theta = \arctan\left(\frac{2X}{R^2+X^2}\Delta R\right) \approx \frac{2X}{R^2+X^2}\Delta R \tag{2.12}$$

As can be seen from Eq. 2.11 and 2.12, the resulting deviation in impedance magnitude is proportional to ΔR^2, while the deviation in phase is proportional to ΔR. So for small deviations ΔR the phase of the input impedance is more sensitive to load resistance mismatch than is the magnitude. This is also true for four element compression networks. It can be seen in Fig. 2.3 and Fig. 2.7 that the match between theory and experiment is better for magnitude than for phase. Moreover, in Fig. 2.7, the network achieves impedance compression and transformation through resonant action, working at high quality factor over some of the operating range. As with other high-quality factor networks operated near resonance, the phase is more sensitive to both deviations in frequency and in component values (e.g. parasitics) than is the magnitude. Thus, small unmodeled parasitics can easily lead to the observed differences in phase. Nevertheless, the performance observed is quite acceptable for many practical applications.

The compression networks of Fig. 2.2 also have an interesting effect when the matched load impedances are not perfectly resistive. In fact, as shown in Section 2.6, these networks can provide substantial "phase compression" of the input impedance (towards zero phase) for matched loads having an impedance magnitude near X but varying phase.

The results presented in both the two element and four element resistance compression networks show the potential for marked improvement in the performance of load-sensitive power converters. This effect is described in detail in Section 2.6.

2.3 Resistance-Compressed Rectifiers

A resistance compression network can be combined with an appropriate set of rectifiers to yield an rf-to-dc converter with narrow-range resistive input characteristics. In order to obtain the desired compression effect, the rectifier circuits must effectively act as a matched pair of resistances when connected to a compression network of the kind described in Section 2.2. A purely resistive input impedance can be achieved with a variety of rectifier structures. For example, in many diode rectifiers the fundamental ac voltage and current at the rectifier input port are in phase, though harmonics may be present [15].

One example of this kind of rectifier structure is an ideal half bridge rectifier driven by a sinusoidal current source of amplitude I_{in} and frequency ω_s, and having a constant output voltage $V_{dc,out}$, as shown in Fig. 2.9. The voltage at the input terminals of the rectifier $v_x(t)$ will be a square wave having a fundamental component of amplitude $V_{x1} = \frac{2V_{dc,out}}{\pi}$ in phase with the input current $i_{in}(t)$, as shown in Fig. 2.10. The electrical behavior at the fundamental frequency ω_s (neglecting harmonics) can be modelled as a resistor of value $R_{eq} = \frac{2}{\pi}\frac{V_{out}}{I_{in}}$. Similarly, a full wave rectifier with a constant voltage at the output can be modelled at the fundamental frequency as a resistor $R_{eq} = \frac{4}{\pi}\frac{V_{dc,out}}{I_{in}}$. There are many other types of rectifier topologies that present the above mentioned behavior; another example is the resonant rectifier of [24]. This rectifier also presents a resistive impedance characteristic at the fundamental frequency; furthermore, it requires only a single semiconductor device and incorporates the necessary harmonic filtering as part of its structure. Such a rectifier, when connected to a constant output voltage, presents a resistive equivalent impedance of the same magnitude as that of the full wave rectifier, $R_{eq} = \frac{4}{\pi}\frac{V_{dc,out}}{I_{in}}$. Still another type of rectifier providing this type of behavior is the resonant rectifier used in the dc/dc converter of Fig. 2.16 [24].

Driving this type of rectifier with a tuned network suppresses the harmonic content inherent in its operation and results in a resistive impedance characteristic at the desired frequency. This equivalent resistance can be represented by $R_{eq} = \frac{k_{rect}}{|i_1|}V_{dc,out}$, where k_{rect} depends on the specific rectifier structure and $|i_1|$ is the fundamental component of the drive current. As shown below, when two identical such rectifiers feed the same dc output and are driven via reactances with equal impedance magnitudes (e.g., as in the circuits of Fig. 2.2), they act as matched resistors with values that depend on the dc output. Thus, a pair of such rectifiers

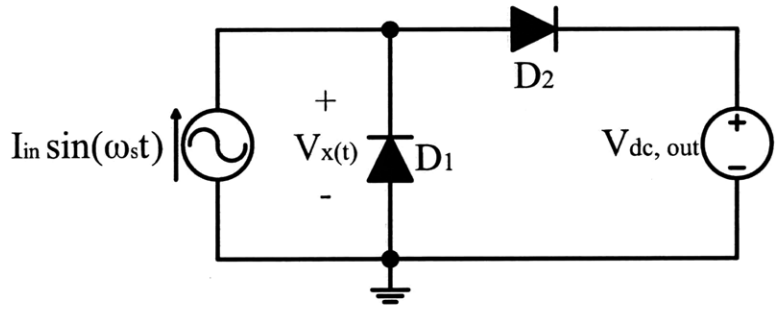

Figure 2.9: Half-wave rectifier with constant voltage load and driven by a sinusoidal current source.

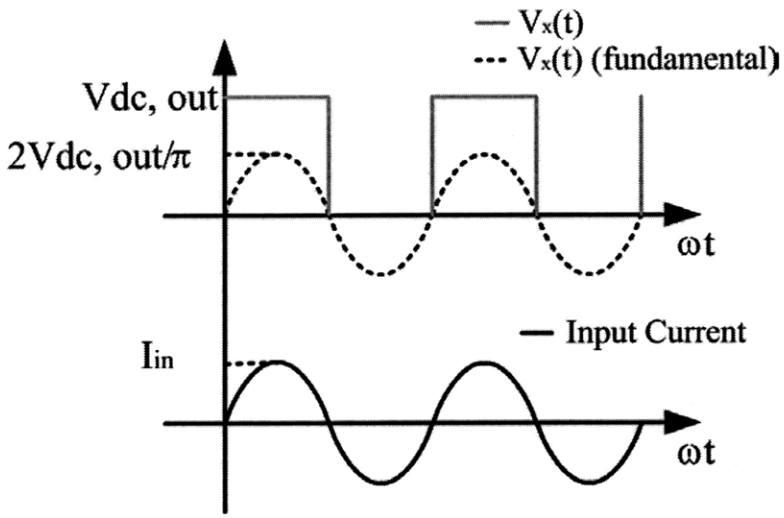

Figure 2.10: Characteristic waveforms of the half-wave rectifier shown in Fig. 2.9. The input current and the fundamental of the input voltage are in phase.

can be used with a compression network to build a rectifier system having a resistive ac-side (input) characteristic that varies little as the dc-side operating conditions change. This type of compression network/rectifier combination can be modelled as shown in Fig. 2.11.

We can express the magnitude of the current i_1 as:

$$|i_1| = \frac{V_{ac}}{\sqrt{X^2 + R_{eq}^2}} \tag{2.13}$$

By replacing R_{eq} with its corresponding value $R_{eq} = \frac{k_{rect}}{|i_1|} V_{dc,out}$ we obtain

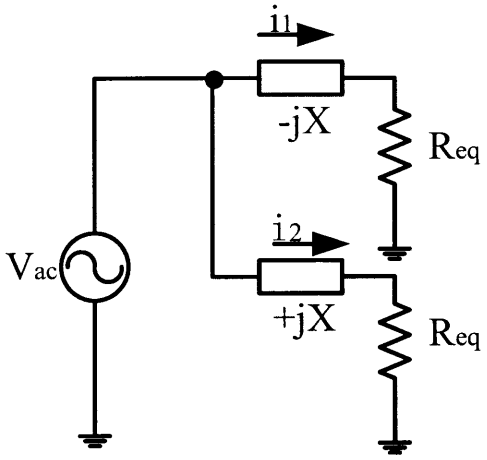

Figure 2.11: A two element compression network with reactive branches represented by impedances evaluated at the operating frequency

$$|i_1| = \frac{V_{ac}}{\sqrt{X^2 + \frac{k_{rect}^2}{|i_1|^2} V_{dc,out}^2}} \tag{2.14}$$

Rearranging:

$$|i_1|^2 X^2 + k_{rect}^2 V_{dc,out}^2 = V_{ac}^2 \tag{2.15}$$

Solving for $|i_1|$:

$$|i_1| = \sqrt{\frac{V_{ac}^2 - k_{rect}^2 V_{dc,out}^2}{X^2}} \tag{2.16}$$

From this expression we can see that the branch current magnitude $|i_1|$ depends on the dc output voltage and the reactance magnitude. The branch carrying $|i_2|$ has the same reactance magnitude and output voltage, so both branches present identical effective load resistances.

For all the rectifier structures that can be represented by an equivalent resistance of value $R_{eq} = \frac{k_{rect}}{|i_1|} V_{dc,out}$, we can express the equivalent resistances loading each branch as:

$$R_{eq} = \frac{k_{rect}V_{dc,out}}{\sqrt{\frac{V_{ac}^2 - k_{rect}^2 V_{dc,out}^2}{X^2}}} = X\sqrt{\frac{1}{\left(\frac{V_{ac}}{k_{rect}V_{dc,out}}\right)^2 - 1}} \tag{2.17}$$

The net input resistance of the resistance-compressed rectifier set at the specific frequency will be determined in Eq. 2.4 where R_{eq} for the rectifier replaces R.

Looking from the dc side of the resistance compressed rectifier we also see interesting characteristics. For a given ac-side drive, a resistance-compressed rectifier will act approximately as a constant power source, and will drive the output voltage and/or current to a point where the appropriate amount of power is delivered.

2.4 Design Considerations for Resistance Compression Networks

In designing resistance compression networks and resistance compressed rectifiers there are some subtle considerations that must be taken into account. The first consideration is how the compression network processes frequencies other than the operating frequency. When a compression network is loaded with rectifiers, the rectifiers typically generate voltage and/or current harmonics that are imposed on the compression network. It is often desirable to design the compression network to present high or low impedances to dc and to the harmonics of the operating frequency in order to block or pass them. Moreover, in some cases it may be important for the impedances of the two branches to be similar at harmonic frequencies in order to maintain balanced operation of the rectifiers or selected so as to provide resistance compression at one or more harmonic frequencies. To achieve this, it is often expedient to use multiple passive components to realize each of the reactances in the network (i.e., reactances $\pm jX$ in Fig. 2.2.) This strategy was employed in the compression network of the system in Fig. 2.16 described in the following section.

A second design consideration is that of selecting a center impedance Z_C for the compression. Typically, one places the center impedance at the geometric mean of the load resistance range to maximize the amount of compression. However, in some cases one might instead choose to offset the center impedance from the middle of the range. This might be done to make the input resistance of the compression network vary in a particular direction as the power level changes. Also, in systems that incorporate impedance or voltage transformation, different placements of the compression network are possible, leading to different possible values of Z_C. For example, one might choose to place a transformation stage before the

compression network, on each branch after the compression network, or both. The flexibility to choose Z_C in such cases can be quite valuable, since centering the compression network at too high or too low an impedance level can lead to component values that are either overly large or so small that they are comparable to parasitic elements.

A third major consideration is circuit quality factor and frequency sensitivity. Since compression networks operate on resonant principles, they tend to be highly frequency selective. This fact requires careful component selection and compensation for circuit parasitics in the design and layout of a compression network. Moreover, as with matching networks that realize large transformation ratios [32], compression networks realizing large degrees of compression require high quality-factor components. Component losses typically limit the practical load range over which useful compression may be achieved.

2.5 Motivation and Example Application: a 100 MHz dc/dc Converter

The resistance compression networks described in Section 2.2 and resistance-compressed rectifiers described in Section 2.3 have many potential applications, including radio-frequency rectifiers (e.g., for rectennas, or rectified antennas [24, 48]), dc/dc converters operating at VHF and microwave frequencies, and energy recovery in rf power amplifier [49]. Here this section describes some motivations for their use in resonant dc/dc converters, and provide a practical example of a resistance compressed rectifier in a 100 MHz dc/dc converter.

2.5.1 Motivation

The motivation for resistance compression networks in rf-to-dc conversion applications is straightforward: The compression network allows the rectifier system to appear as an approximately constant-resistance load independent of ac drive power or dc-side conditions. In rectenna applications this can be used to improve matching between the antenna and the rectifier. As will be shown, this is also useful for preserving efficient operation of resonant dc/dc converters as operating conditions change.

As described in Section 1.1, resonant dc/dc power converters can be constructed with a resonant inverter, a rectifier, and a transformation stage to provide the required matching between the rectifier and the inverter. An inherent limitation of most resonant inverters suitable for VHF operation is their high sensitivity to loading conditions. This sensitivity arises because of the important role the load plays in shaping converter waveforms.

Consider, for example, a class E inverter designed to operate efficiently at a nominal load resistance. As the load resistance deviates substantially from its design value, the converter waveforms rapidly begin to deteriorate. As seen in the example drain-source waveforms of Fig. 2.12, the peak switch voltage rises rapidly when the resistance deviates in one direction[2]. Moreover, zero-voltage turn-on of the device is rapidly lost for deviations in either direction (c.f. Fig. 2.12, [1, Fig. 5]).

There are at least three reasons why maintaining near zero-voltage switch turn on is important in very high frequency power converters. First, the turn-on loss associated with the discharge of the capacitance across the switch is undesirable and eliminating this loss is often important for achieving acceptable efficiency. Second, a rapid drain voltage transition at turn on can affect the gate drive circuit through the Miller effect, increasing gating loss and possibly increasing switching loss due to the overlap of switch voltage and current. This issue can be of particular concern in circuits employing resonant gate drives, and in cases where the gate drive transitions are a significant fraction (e.g., 5%) of the switching cycle. Finally, zero-voltage switching avoids electromagnetic interference (EMI) and capacitive noise injection generated by rapid drain voltage transitions.

In view of the above considerations, there exist substantial limits on allowable load variations. In the example of Fig. 2.12, even if the maximum switch off-state voltage is allowed to increase and the switch voltage magnitude at turn on is allowed to be as large as the dc input voltage (a substantial deviation from zero-voltage switching), the permissible load resistance range is only a factor of approximately 3 : 1 (a range of 6 Ω to 2 Ω in Fig. 2.12). Requiring a closer approximation to zero-voltage turn on will necessitate maintaining a still narrower resistive load range.

This limitation in load range is further exacerbated in resonant dc/dc converters. As shown in Section 2.3, the effective resistance presented to the inverter typically depends on both ac drive levels (and hence on input voltage) and on the dc output of the rectifier. These dependencies pose a challenge to the design of resonant dc/dc converters at very high frequencies.

[2]This effect is somewhat mitigated in circuits where the switch has an intrinsic or external antiparallel diode. However, the diode introduces loss and parasitic effects of its own, so such operation is still not desirable.

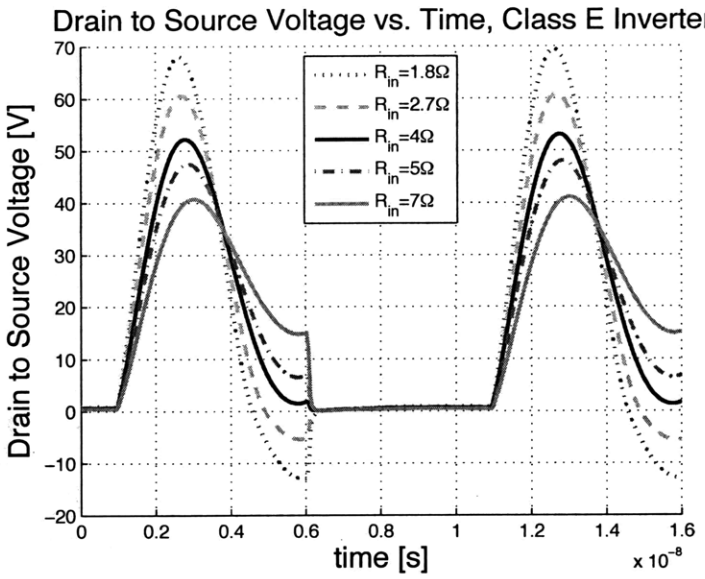

Figure 2.12: Drain to source voltage for a class E inverter for different values of resistance. Using the notation in [1] $L_1 = 538$ nH, $L_2 = 24.2$ nH, $C_1 = 120$ pF (non-linear), $C_2 = 163.5$ pF, $1.8\ \Omega \leq R \leq 7\ \Omega$. Optimal zero-voltage switching (ZVS) occurs at $R = 4\ \Omega$. When the resistor deviates from its nominal value ZVS is not achieved.

2.5.2 Example Application

The high sensitivity of radio-frequency converters such as the class E inverter to variations in load resistance is a significant limitation, and motivates the development of circuit techniques to compensate for it.

To demonstrate the use of resistance compression to benefit very high frequency dc/dc power converters, a prototype dc/dc converter operating at 100 MHz was developed. The circuit consists of a class E inverter with self-oscillating gate drive [3], a matching network, a resistance compression network of the type shown in Fig. 2.2(b), and a set of two resonant rectifiers which have a resistive characteristic at the fundamental frequency. The switching frequency for the converter is 100 MHz, the input voltage range is 11 V $\leq V_{\text{in,dc}} \leq$ 16 V and the maximum output power capability ranges from 11.4 W at $V_{in,dc} = 11$ V to 24.5 W at $V_{in,dc} = 16$ V. The detailed schematic of the circuit implementation is shown in Fig. 2.16 and the components used are listed in Table 2.4. A photograph of the prototype converter is shown in Fig. 2.17, and detailed layout information for the resistance compressed rectifier is provided in Fig. A.2 and appendix A.

[3] The author's colleagues David Jackson and Juan Rivas designed the inverter and gate drive; more details about the overall design can be found in [2, 38, 39].

In order to minimize the gating losses of the LDMOSFET, a self-oscillating multi-resonant gate drive was used. This gate driver is conceptually similar to the converter circuits presented in [50], resulting in a gate to source voltage with a pseudo-square wave characteristic that provides fast and efficient commutation of the main semiconductor device without driving the gate-source voltage negative. The average power dissipated in the resonant driver was found to be 350mW; through subsequent work we have been able to reduce this substantially [39].

Each of the two resonant rectifiers in Fig. 2.16 are designed to appear resistive in the sense that the fundamental ac voltage at the rectifier input is largely in phase with the drive current when the rectifier is driven from a sinusoidal current. (The compression network reactances are designed to block the voltage harmonics created by the rectifiers.) The instantaneous power level of the converter varies with input voltage (as expected for a class E inverter). At $V_{dc,out} = 12$ V, each rectifier is designed to present an equivalent resistance (at the fundamental) ranging from 12 Ω (at an output power of 13.8 W) to 27.4 Ω (at an output power of 5.75 W). These values were arrived at through simulations of the rectifier network over a range corresponding to the approximate instantaneous power levels expected (see Fig. 2.15) [2, 39]. The rectifier impedance is determined by rectifier output voltage, instantaneous rectifier power (as determined by the input voltage) and resonant components. In this design, we only need to consider operation for an output voltage of 12 V, independent of load resistance. This is because the converter is designed to run under on/off control [4, 35]. In this approach, the entire converter is modulated on and off (at frequencies orders of magnitude lower than the switching frequency) such that the output is always maintained at 12 V. Hence, the rectifier input impedance depends on the input voltage (and instantaneous power as illustrated in Fig. 2.15), but not on the converter load.

The compression network is designed for a nominal operating frequency of 100 MHz and a center impedance $Z_c = 20$ Ω. Simulations predict a compressed resistance ranging from 21 Ω down to 20 Ω and back up to 22.7 Ω as power ranges from minimum to maximum. Moreover, the compression network is designed to present a high impedance to dc and harmonics of the fundamental.

To enable the compression network and rectifiers to operate at a convenient impedance level, an L-section matching network is used. This network comprises shunt inductance L_1, with the capacitive portion of the L-section network absorbed as part of the resonant capacitor C_R.

Experimental results support the efficacy of the compression network for providing a desired narrow-range impedance to the inverter as the power level varies with input voltage. Figure 2.13 shows experimental waveforms for the converter running at $V_{in,dc} = 11$ V and

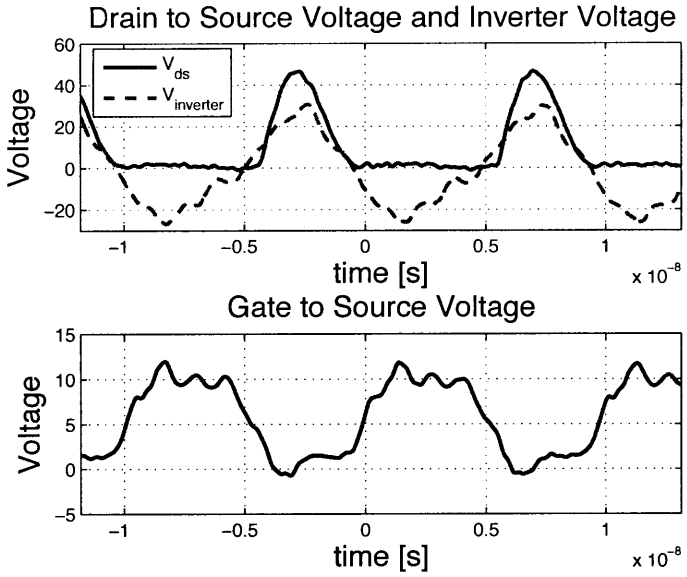

Figure 2.13: Drain to source voltage, inverter output voltage, and gate to source voltage of the prototype converter

$V_{out,dc} = 12$ V. Shown in the figure are the voltage at the gate of the MOSFET, the drain to source voltage of the device and the voltage at the input of the compression network. It can be appreciated from the figure that zero-voltage turn-on of the LDMOSFET is achieved, indicating a proper impedance match.

Figure 2.14 shows V_{ds} at input voltages of 11 V, 13.5 V, and 16 V. As can be appreciated from the respective figures, the zero-voltage condition is achieved over the whole input voltage range: a situation that would not occur without the resistance compression network operating as desired.

Figure 2.15 shows the output power and the efficiency of the prototype converter. It can be appreciated that the output power has a characteristic roughly proportional to the square of the input voltage, another indication that the compression network is functioning to keep the effective load resistance constant as operating conditions change.

The simulation results for output power match the experimental results well at low input voltage, but depart somewhat as input voltage is increased. We attribute this to the parasitic components and coupling which are not fully modeled in our simulations and which are difficult to measure with sufficient precision to model appropriately. The nonlinear device drain capacitance and resonant inductance (and parasitics at those locations) seem to be particularly important in this regard. Variations in Schottky diode performance with power level may also account for some of the deviation. It is not surprising that the deviation

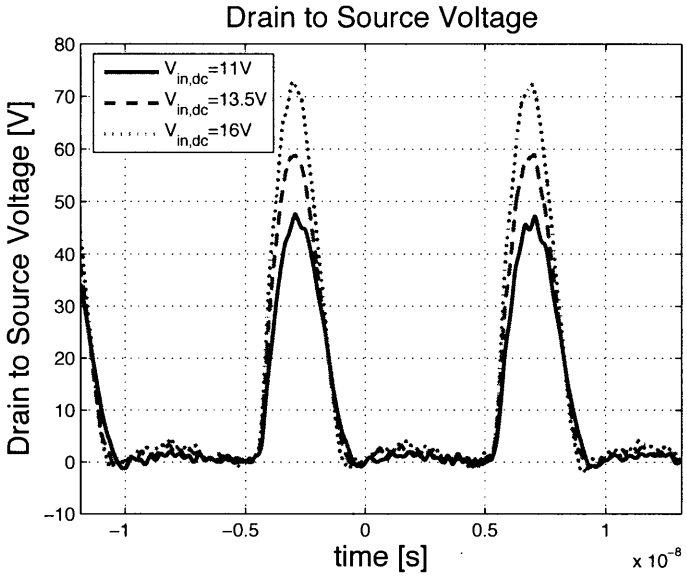

Figure 2.14: Drain to source voltage for different input voltages in the range 11 V $\leq V_{in,dc} \leq$ 16 V. The inverter is seen to maintain soft switching over the full range.

increases at high voltage, given that both the modeled and actual power behavior are approximately proportional to V_{in}^2. (In the ideal class E inverter, power is proportional to V_{in}^2, with a proportionality constant depending on frequency, duty ratio, resonant component values and load impedance [51].) The effects of any deviations thus scale up rapidly with voltage. Likewise, the simple simulation model does not account for some loss mechanisms (e.g., conduction losses in traces and interconnects) and so slightly overestimates converter efficiency. Nevertheless, the observed behavior is consistent with proper operation of the compression network, and is acceptable for practical purposes.

2.6 Behavior of "Phase Compression" Effect

This section considers the behavior of the compression networks of Fig. 2.2 when the (matched) load impedances are not purely resistive.

As will be shown, if the matched loads are both resistive and reactive, the resistance compression network can serve to transform the load impedances in a manner that makes the network impedance more resistive than the loads, thus providing "phase compression" of the load impedance.

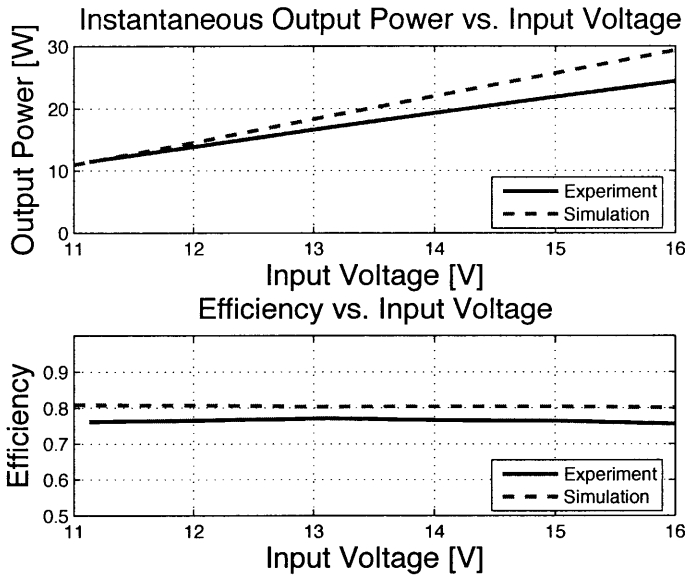

Figure 2.15: Experimental and simulated output power and efficiency vs. input voltage. Simulations were carried out using PSPICE. The MOSFET was modeled as switched resistor in parallel with a nonlinear capacitor, and the on-state of the diode was modeled with a constant voltage drop plus a series of resistance. Inductor ac and dc ESR values were modeled, while capacitors were treated as ideal.

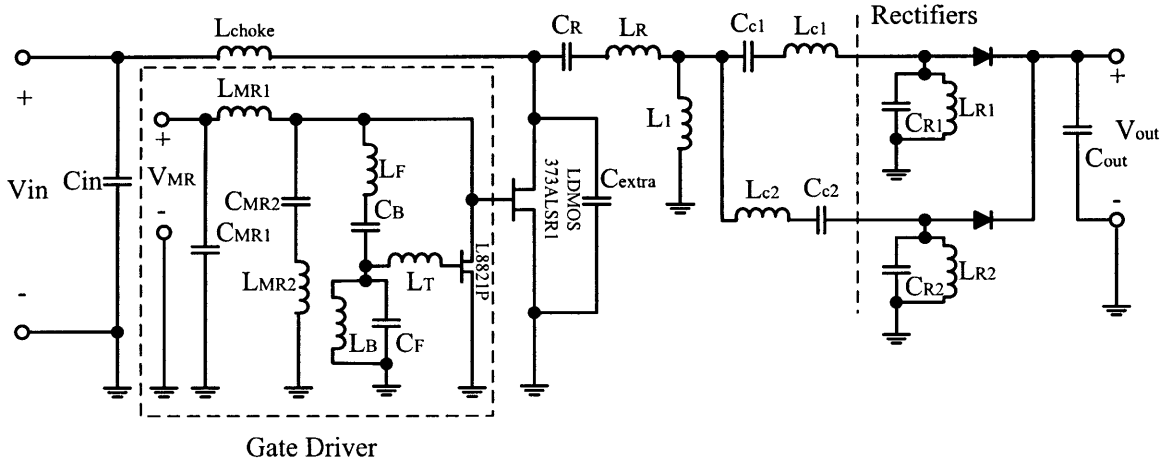

Figure 2.16: A 100 MHz dc/dc power converter incorporating a resistance compression network.

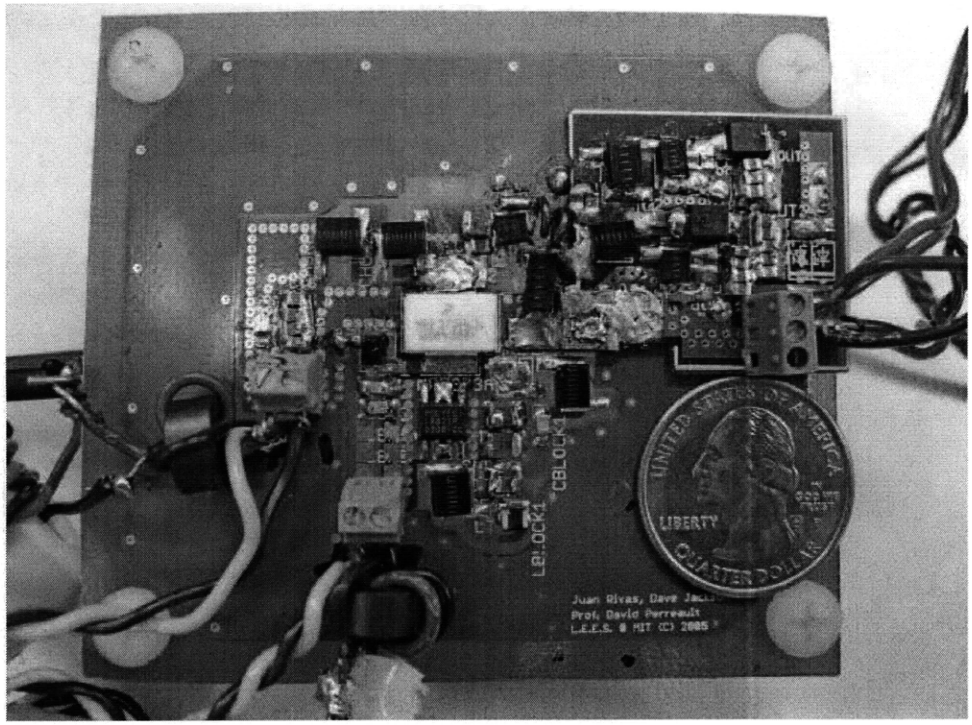

Figure 2.17: Prototype dc/dc power converter.

Figure 2.18 shows the compression networks of Fig. 2.2, with the load resistances replaced by complex impedances.

For example, in Fig. 2.18(a), the load impedance can be expressed as:

$$Z_L = R_L + jX_L = |Z_L|\angle\alpha \qquad \text{at} \qquad \omega = \omega_0 \tag{2.18}$$

$$|Z_L| = \sqrt{R_L^2 + X_L^2} \qquad \text{and} \qquad \tan\alpha = \frac{X_L}{R_L} \tag{2.19}$$

The input impedance at $\omega = \omega_0$ can be expressed as:

$$Z_{in} = |Z_{in}|\angle\theta = \frac{2X^2[R_L(X^2 + |Z_L|^2) + jX_L(X^2 - |Z_L|^2)]}{[R_L^2 + (X_L + X)^2][R_L^2 + (X_L - X)^2]} \tag{2.20}$$

$$\tan\theta = \frac{X_L}{R_L}\left[\frac{X^2 - |Z_L|^2}{X^2 + |Z_L|^2}\right] = \tan\alpha\left[\frac{X^2 - |Z_L|^2}{X^2 + |Z_L|^2}\right] \tag{2.21}$$

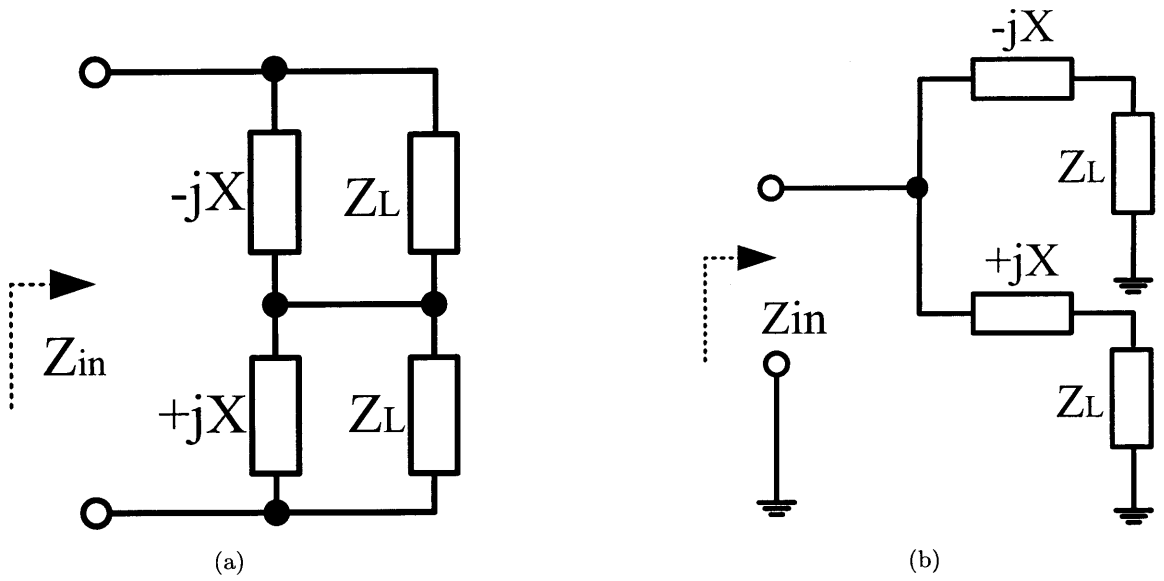

Figure 2.18: Impedance compression networks terminated in matched non-resistive loads

Since $\left|\frac{X^2-|Z_L|^2}{X^2+|Z_L|^2}\right| < 1$, we find $|\theta| < |\alpha|$. That is, the magnitude of the input impedance phase angle θ is less than the magnitude of the load phase angle α, thus providing "phase compression".

$$\frac{\tan\theta}{\tan\alpha} = \frac{X^2 - |Z_L|^2}{X^2 + |Z_L|^2} \tag{2.22}$$

If the magnitude of the matched load impedances equals that of the compression network reactances ($|Z_L| = X$), the input impedance is totally resistive for any load phase angle, which means the load reactive component is eliminated. As the magnitude of the matched load impedances deviates from those of the compression network, the compression effect decreases. The amount of phase angle compression achieved for several load impedances is illustrated in Table 2.5.

Figure 2.19 plots the normalized magnitude and phase of Z_{in} as a function of load impedance phase α for the circuit of Fig. 2.18(a). The compression in input impedance magnitude and phase achieved with different load impedance magnitudes can be observed.

The input impedance for the compression network of Fig. 2.18(b) is:

$$Z_{in} = |Z_{in}|\angle\theta = \frac{R_L(|Z_L|^2 + X^2) + jX_L(|Z_L|^2 - X^2)}{2|Z_L|^2} \tag{2.23}$$

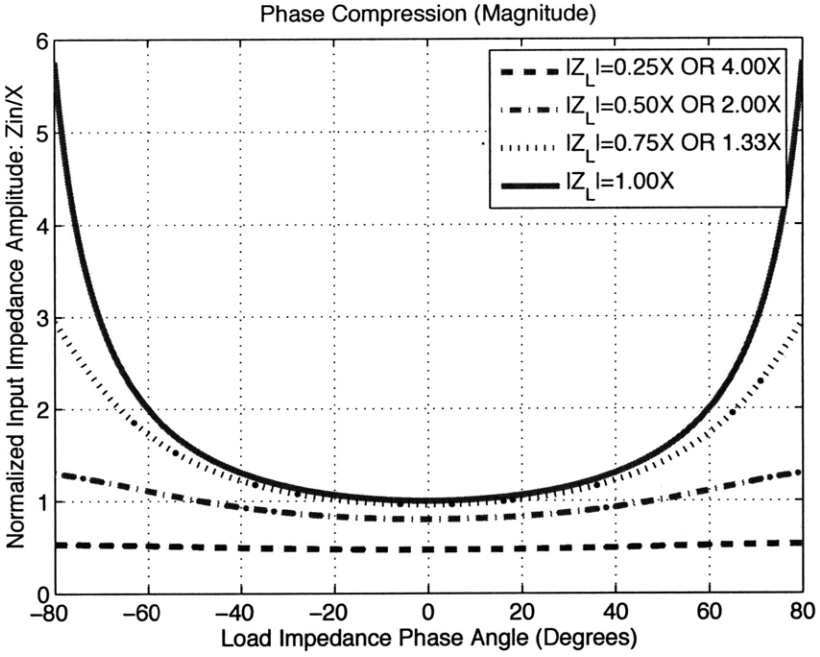

(a)

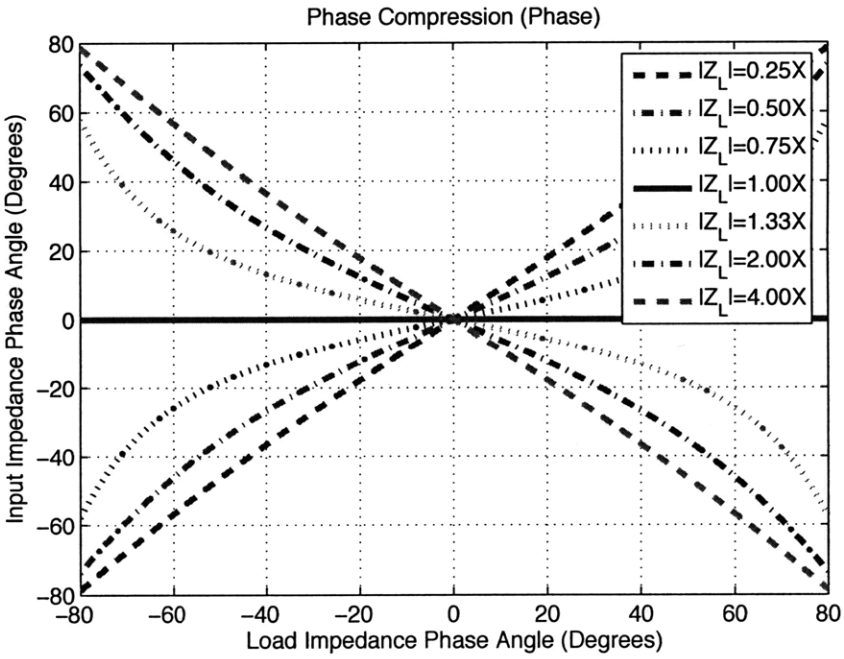

(b)

Figure 2.19: Z_{in} vs load impedance phase α, parameterized in load impedance magnitude $|Z_L|$ for the topology of Fig. 2.18(a)

This circuit likewise provides compression of the input impedance angle, with a measure of compression given by:

$$\frac{\tan\theta}{\tan\alpha} = \frac{|Z_L|^2 - X^2}{X^2 + |Z_L|^2} \tag{2.24}$$

Figure 2.20 shows the normalized magnitude and phase of Fig. 2.18(b) as load impedance angle varies. The anticipated compression in load phase angle is achieved with different loads.

As detailed above, the compression networks of Fig. 2.18 can provide a limited degree of compensation for non-resistive characteristics of the matched loads. The input impedance of the compression network will be more closely resistive than that of the loads. This effect is quite pronounced for load impedance magnitudes near the impedance magnitude of the compression network.

In order to verify the phase compression calculation of Eq. 2.23 and 2.24, measurements were carried out using the compression network type in Fig. 2.18(b). The tested compression networks have the topologies indicated in Fig. 2.21 and are implemented on printed circuit boards. The loads are purely resistive in Fig. 2.21(a). The complex load impedance Z_{L1} and Z_{L2} in Fig. 2.21(b) and Fig. 2.21(c) are achieved via parallel combinations of resistors and reactive components. Table 2.6 shows component values corresponding to the topologies in Fig. 2.21. All these values were measured with an impedance analyzer at a frequency of 100 MHz. The pairs of components such as C_X and L_X, L_{R1} and L_{R2}, C_{R1} and C_{R2}, R_1 and R_2 are carefully selected to make them as matched as possible.

Table 2.7 shows calculated and measured input impedances at a frequency of 100 MHz. The values of X_{LX} and X_{CX} are the reactances of L_X and C_X in Table 2.6. Z_{L1} and Z_{L2} are load impedances. The load phase angles are approximately 0°, 57° and −57° in Fig. 2.21 (a), (b) and (c). $Z_{in}(Cal)$ is the input impedance calculated by Eq. 2.23, letting $X \approx X_{LX} \approx X_{CX}$ and $Z_L \approx Z_{L1} \approx Z_{L2}$. Because $X \approx |Z_L|$ in Table 2.7, the calculated input impedance $Z_{in}(Cal)$ has approximate zero phase angle by Eq. 2.24. Z_{in} is the input impedance measured with an impedance analyzer. Z_{in} is close to $Z_{in}(Cal)$. The measured input impedance phases are within approximately 9° of the predicted values, successfully demonstrating the predicted phase compression. The small differences of magnitude and phase between Z_{in} and $Z_{in}(Cal)$ are believed to arise mainly due to parasitic components of the printed circuit board and the limited precision with which were able to model the components.

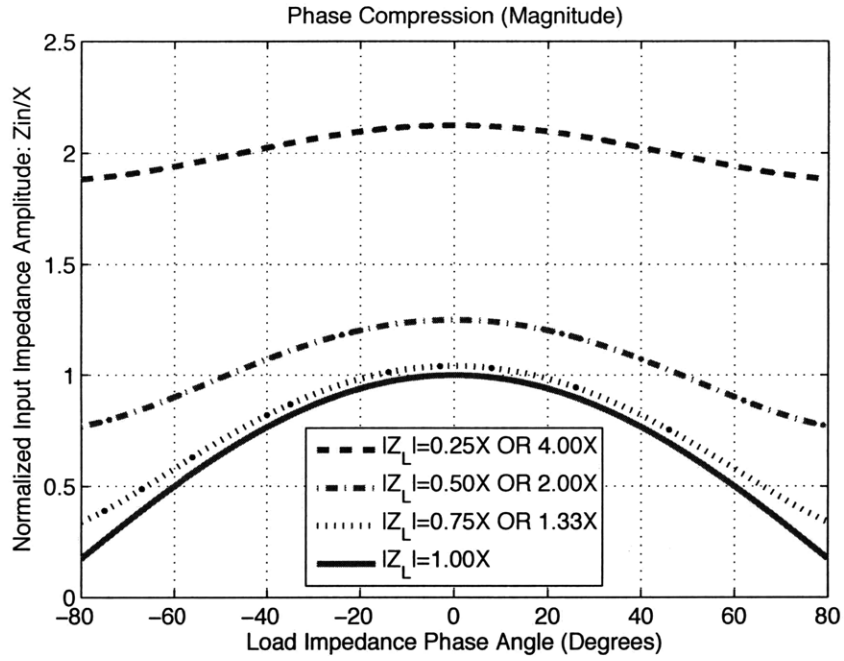

(a)

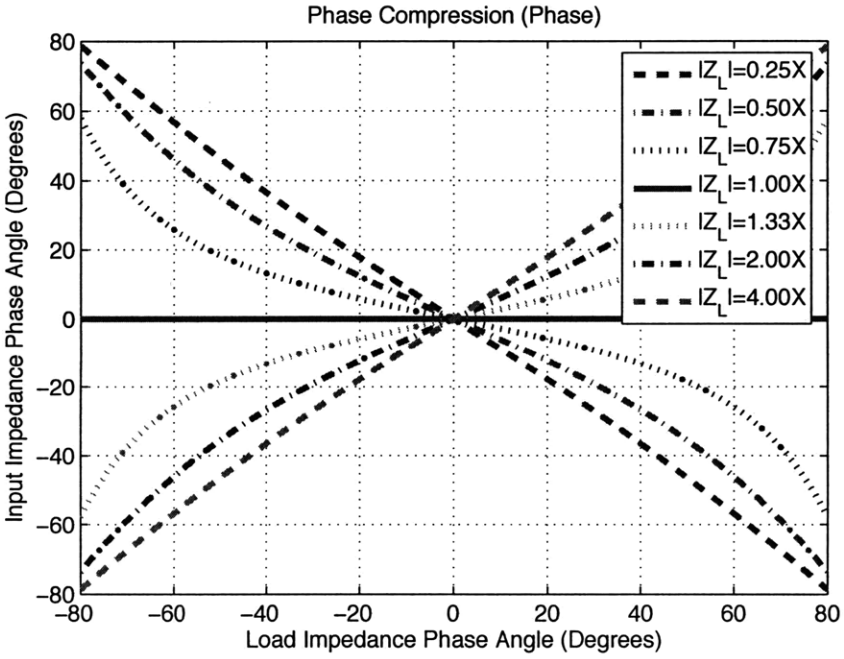

(b)

Figure 2.20: Z_{in} vs load impedance phase α, parameterized in load impedance magnitude $|Z_L|$ for the topology of Fig. 2.18(b)

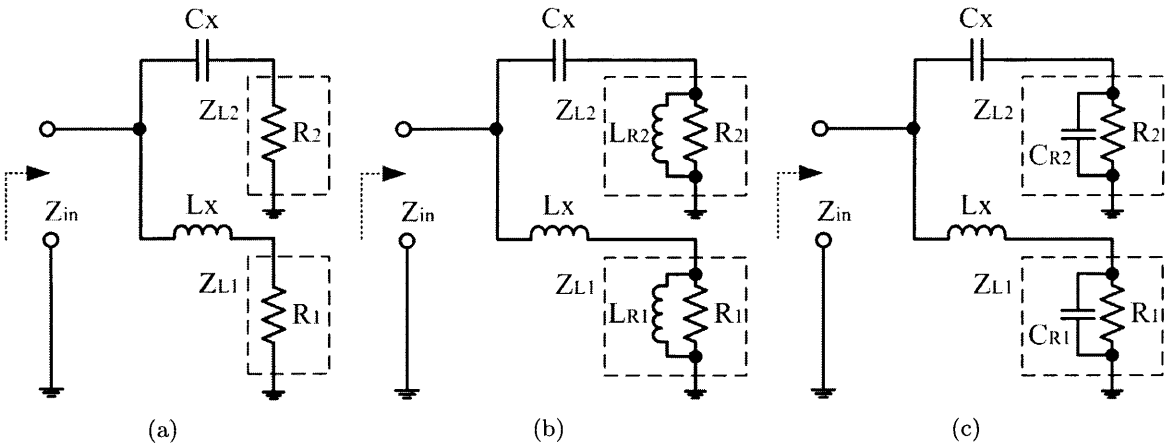

Figure 2.21: Topologies of experimental compression networks for testing phase compression effects. The load impedances are purely resistive in (a). Complex load impedances Z_{L1} and Z_{L2} in (b) and (c) are achieved by parallel combinations of resistors and reactive components.

2.7 Conclusion

This chapter proposes a new class of matching networks that promise a significant reduction in the load sensitivity of resonant converters and rf amplifiers. These networks, which are termed resistance compression networks, serve to greatly decrease the variation in effective resistance seen by a tuned rf inverter as loading conditions change. The operation, performance, and design of these networks are explored. The application of resistance compression is demonstrated in a 100 MHz dc/dc converter. Experimental results from this converter confirm the effectiveness of compression networks for reducing load sensitivity of resonant dc/dc converters. This technique is also described in the author's publications [26, 34] and in U.S. Patent 7,535,133, [52] which covers aspects of this technique. It is anticipated that the proposed approach will allow significant improvements in the performance of very high frequency power converters.

Table 2.4: Components used in 100 MHz dc/dc converter of Fig. 2.16.

Component Name	Nominal Value	Manufacturer and Part Style	Part Number	Measured Value
C_{C1}	18 pF +15 pF	CDE Chip-Mica 100 V MC08EA150J	MC08EA180J	36.22 pF
C_{C2}	56 pF +7 pF	CDE Chip-Mica 100 V MC08CA070C	MC12FA560J	66.5 pF
C_{extra}	10 pF × 2	CDE Chip-Mica 100 V	MC08CA100D	
C_{in}	2.2 μF +0.68 μF +0.047 μF × 12	Tantalum 35 V Tantalum 35 V Ceramic 50 V	PCT6225CT PCT6684CT Kemet	
C_R	82 pF +2 pF	CDE Chip-Mica 100 V MC08CA020D	MC12FA8205	
C_{R1}, C_{R2}	15 pF × 2	CDE Chip-Mica 100 V	MC08EA150J	$C_{R1} = 32.6$ pF $C_{R2} = 32$ pF
C_{out}	0.1 μF × 19	Kemet Ceramic 50 V	C0805C104M5UAC	
D_1, D_2	Schottky Power Diode	ON Semi 60 V, 2.0 A	MBRS260T3	
L_1	17.5 nH	Coilcraft	B06T6	
L_{C1}	33 nH	Coilcraft	1812SMS-33N	38.1 nH
L_{C2}	68 nH	Coilcraft	1812SMS-68N	69.9 nH
L_{choke}	120 nH × 2	Coilcraft	1812SMS-R12G	
LDMOS		Freescale 70 V (max V_{ds})	MRF373ALSR1	
L_R	12.5 nH + Two-turn magnet wire coil +8.9 nH board parasitic	Coilcraft	A04TJ 18 AWG	Approx. 22 nH
L_{R1}, L_{R2}	18.5 nH	Coilcraft	A05T	$L_{R1} = 18.9$ nH $L_{R2} = 18.7$ nH

Table 2.5: The θ ranges for different $|Z_L|$ values and α ranges.

	$-30° \leq \alpha \leq 30°$	$-45° \leq \alpha \leq 45°$	$-60° \leq \alpha \leq 60°$
$\|Z_L\| = X$	$\theta = 0°$	$\theta = 0°$	$\theta = 0°$
$\|Z_L\| = 0.75X$ or $1.33X$	$-9.2° \leq \theta \leq 9.2°$	$-15.6° \leq \theta \leq 15.6°$	$-25.9° \leq \theta \leq 25.9°$
$\|Z_L\| = 0.5X$ or $2X$	$-19.1° \leq \theta \leq 19.1°$	$-31.0° \leq \theta \leq 31.0°$	$-46.1° \leq \theta \leq 46.1°$

Table 2.6: The values of components used to obtain data in Table 2.7

	L_X	C_X	L_{R1} or C_{R1}	L_{R2} or C_{R2}	R_1	R_2
Fig. 2.21(a)	47.4 nH	54.0 pF			$29.9\angle 1.7°\ \Omega$	$29.9\angle 1.9°\ \Omega$
Fig. 2.21(b)	47.4 nH	54.0 pF	56.5 nH	56.2 nH	$54.5\angle 1.4°\ \Omega$	$54.5\angle 1.1°\ \Omega$
Fig. 2.21(c)	47.4 nH	54.0 pF	45.7 pF	45.5 pF	$54.5\angle 1.4°\ \Omega$	$54.5\angle 1.1°\ \Omega$

Table 2.7: Calculated and measured impedances at a frequency of 100 MHz

	X_{LX}	X_{CX}	Z_{L1}	Z_{L2}	Z_{in}	$Z_{in}(Cal)$
Fig. 2.21(a)	$29.8\ \Omega$	$29.5\ \Omega$	$29.9\angle 1.7°\ \Omega$	$29.9\angle 1.9°\ \Omega$	$30.5\angle 0°\ \Omega$	$29.6\angle 0.1°\ \Omega$
Fig. 2.21(b)	$29.8\ \Omega$	$29.5\ \Omega$	$29.4\angle 57.3°\ \Omega$	$29.4\angle 57.4°\ \Omega$	$17.1\angle 7.6°\ \Omega$	$15.9\angle -0.4°\ \Omega$
Fig. 2.21(c)	$29.8\ \Omega$	$29.5\ \Omega$	$29.7\angle -57.0°\ \Omega$	$29.7\angle -57.0°\ \Omega$	$17.9\angle 8.9°\ \Omega$	$16.2\angle 0.2°\ \Omega$

Chapter 3

Analysis and Design of High Efficiency Matching Networks

THIS chapter presents analysis and design considerations for lumped (inductor and capacitor) matching networks operating at high efficiency ($> 95\%$). Formulas for calculating matching network efficiency are given, and it is shown that efficiency can be expressed as a function of inductor quality factor Q_L, capacitor quality factor Q_C and transformation ratio. These formulas are used to evaluate the optimum number of L-section matching stages as a function of conversion ratio. Both simulation and experimental results are presented that validate the analytical formulation.

3.1 Background

A matching network is a passive two-port circuit designed to provide narrow-band impedance and voltage transformation between the two ports. While most widely associated with communications applications (e.g., [32,33,46]), matching networks also find useful application in resonant inverters, rectifiers, and dc-dc converters. Most analytical descriptions of matching networks are based on the assumption of no loss. Where efficiency is considered [53], it is typically treated as secondary to other performance goals, in accordance with the needs of communications applications. Moreover, literature focusing on the design of matching networks for very high efficiencies (e.g., $> 95\%$) appears to be lacking. This chapter presents analysis and design considerations for high efficiency lumped-element matching networks.

In Section 3.2, some possible topologies for matching networks are identified, and formulas to calculate their efficiency are developed. In Section 3.3, the implications of the results of Section 3.2 are discussed, and the analytical results are compared to Pspice simulations. Strong agreement between analysis and simulation is demonstrated. Section 3.4 presents experimental results validating the efficiency calculations of Section 3.2. Finally, Section 3.5 concludes the chapter.

3.2 Matching Network Design and Efficiency Analysis

Two basic matching network topologies are shown in Fig. 3.1. Fig. 3.1(a) and Fig. 3.1(b) are low-pass and high-pass single-stage L-section matching networks. These networks can be used to step a load impedance up or down, depending upon which port is connected to the load and which is connected to the source [33]. They can each be used to transform a load resistance of value R_s connected to the right-hand port to a resistance R_p seen from the left-hand port, or to transform a load resistance of value R_p connected at the left-hand port down to a resistance R_s seen from the right-hand port. T and Π matching networks could also be used as basic matching networks. However, they invariably have lower efficiency than an equivalent L-section network [32] and are thus not considered here. Inductor parasitic resistance R_L and capacitor parasitic resistance R_C are shown as explicit circuit elements in each network of Fig. 3.1. V_p and V_s are the peak voltages at the left-hand and right-hand ports. I_p and I_s are the peak currents in the shunt and series legs.

Design of the matching networks of Fig. 3.1 (neglecting R_L, R_C, and the loss associated with them) is well understood [32, 33, 46] and may be carried out as follows. Starting with a desired resistance transformation ratio

$$\frac{R_p}{R_s} = \frac{V_p^2}{V_s^2} \tag{3.1}$$

we can define an associated transformation quality factor

$$Q_T = \sqrt{\frac{R_p}{R_s} - 1} \tag{3.2}$$

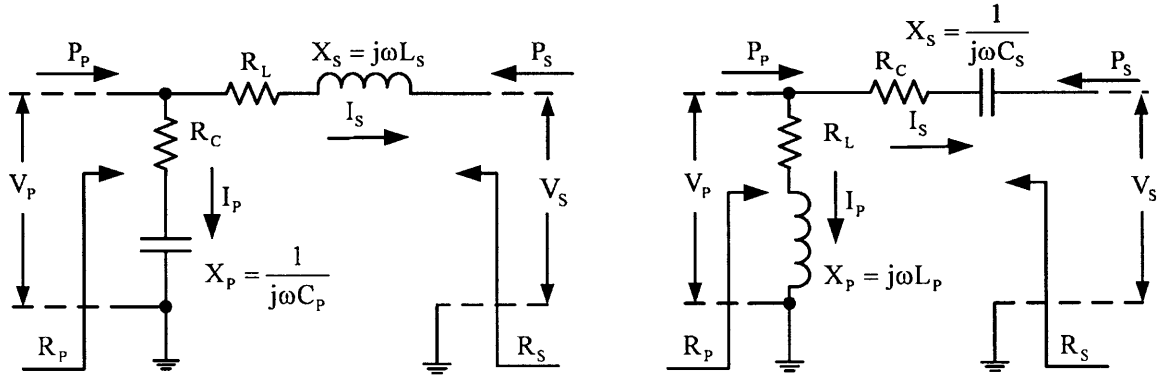

(a) Low-Pass (b) High-Pass

Figure 3.1: L-section matching networks with inductor parasitic resistance shown explicitly.

a series-leg quality factor

$$Q_s = \frac{|X_s|}{R_s} \tag{3.3}$$

and a shunt-leg quality factor

$$Q_p = \frac{R_p}{|X_p|} \tag{3.4}$$

As shown in Fig. 3.1, Q_s is the quality factor of the series leg (where the external network resistances are included and matching network loss is neglected) and Q_p is the quality factor of the shunt leg; R_p is the matched shunt resistance; X_p is the shunt reactance; R_s is the matched series resistance and X_s is the series reactance. To achieve the desired transformation neglecting loss, the matching network reactances are selected such that $Q_s = Q_p = Q_T$.

Losses in high-efficiency matching networks can be computed using the following approximation: the circuit is designed and the circuit currents are calculated on a no-loss basis; the inductor and capacitor losses and circuit efficiency are then calculated based on the losses induced by the calculated currents flowing through inductor resistance R_L and capacitor resistance R_C. This calculation thus assumes that the branch currents are not affected by the presence of small resistive components [32].

Shown in Fig. 3.1, P_s is the power entering the matching network from the right, P_p is the power entering the matching network from the left. We get:

$$|P_s| = \frac{1}{2} I_s^2 R_s \tag{3.5}$$

$$|P_p| = \frac{V_p^2}{2R_p} \tag{3.6}$$

P_{lossC} is the loss power in the capacitor, P_{lossL} is the loss power in the inductor, P_{loss} is the total loss power in the matching network and equal to $P_{lossC} + P_{lossL}$.

Consider, first, the low-pass matching network shown in Fig. 3.1(a). $Q_L = \frac{\omega L_s}{R_L} = \frac{|X_s|}{R_L}$ is the quality factor of the inductor, $Q_C = \frac{1}{\omega C_p R_C} = \frac{|X_p|}{R_C}$ is the quality factor of the capacitor, and η represents the efficiency of the matching network. From Fig. 3.1(a) and above definitions, we have:

$$P_{lossL} = \frac{1}{2} R_L I_s^2 = \frac{|X_s|}{2Q_L} I_s^2 = \frac{Q_T}{Q_L} |P_s| \tag{3.7}$$

$$P_{lossC} = \frac{1}{2} R_C I_p^2 = \frac{|X_p|}{2Q_C} \left(\frac{V_p}{|X_p|} \right)^2 = \frac{V_p^2}{2Q_C |X_p|} = \frac{Q_T}{Q_C} |P_p| \tag{3.8}$$

If the left port is connected to the source and the right port is connected to the load, P_p is positive and P_s is negative:

$$|P_p| = |P_s| + P_{lossL} + P_{lossC} = |P_s| + \frac{Q_T}{Q_L}|P_s| + \frac{Q_T}{Q_C}|P_p| \tag{3.9}$$

$$\eta = \frac{|P_s|}{|P_p|} = \frac{1 - \frac{Q_T}{Q_C}}{1 + \frac{Q_T}{Q_L}} \tag{3.10}$$

If the left port is connected to the load and the right port is connected to the source, P_p is negative and P_s is positive:

$$|P_s| = |P_p| + P_{lossL} + P_{lossC} = |P_p| + \frac{Q_T}{Q_L}|P_s| + \frac{Q_T}{Q_C}|P_p| \tag{3.11}$$

$$\eta = \frac{|P_p|}{|P_s|} = \frac{1 - \frac{Q_T}{Q_L}}{1 + \frac{Q_T}{Q_C}} \tag{3.12}$$

Next consider the high-pass matching network shown in Fig. 3.1(b). The inductor quality factor $Q_L = \frac{\omega L_p}{R_L} = \frac{|X_p|}{R_L}$ and the capacitor quality factor $Q_C = \frac{1}{\omega C_s R_C} = \frac{|X_s|}{R_C}$. From Fig. 3.1(b) and above definitions, we have:

$$P_{lossC} = \frac{1}{2}R_C I_s^2 = \frac{|X_s|}{2Q_C} I_s^2 = \frac{Q_T}{Q_C}|P_s| \tag{3.13}$$

$$P_{lossL} = \frac{1}{2}R_L I_p^2 = \frac{|X_p|}{2Q_L}\left(\frac{V_p}{|X_p|}\right)^2 = \frac{V_p^2}{2Q_L|X_p|} = \frac{Q_T}{Q_L}|P_p| \tag{3.14}$$

If the left port is connected to the source and the right port is connected to the load, P_p is positive and P_s is negative:

$$|P_p| = |P_s| + P_{lossC} + P_{lossL} = |P_s| + \frac{Q_T}{Q_C}|P_s| + \frac{Q_T}{Q_L}|P_p| \tag{3.15}$$

$$\eta = \frac{|P_s|}{|P_p|} = \frac{1 - \frac{Q_T}{Q_L}}{1 + \frac{Q_T}{Q_C}} \tag{3.16}$$

If the left port is connected to the load and the right port is connected to the source, P_p is negative and P_s is positive:

$$|P_s| = |P_p| + P_{lossC} + P_{lossL} = |P_p| + \frac{Q_T}{Q_C}|P_s| + \frac{Q_T}{Q_L}|P_p| \tag{3.17}$$

$$\eta = \frac{|P_p|}{|P_s|} = \frac{1 - \frac{Q_T}{Q_C}}{1 + \frac{Q_T}{Q_L}} \tag{3.18}$$

When $\frac{Q_T}{Q_L} \ll 1$ and $\frac{Q_T}{Q_C} \ll 1$ (i.e., for the case of high efficiency), we can approximate Eq. 3.10, 3.12, 3.16 and 3.18 by neglecting products of these small quantities. In each case, this yields:

$$\eta \approx 1 - \frac{Q_T}{Q_L} - \frac{Q_T}{Q_C} \tag{3.19}$$

Notice we get the same efficiency for the low-pass and high-pass matching networks if $\frac{Q_T}{Q_L} \ll 1$ and $\frac{Q_T}{Q_C} \ll 1$ (i.e. for the case of high efficiency). Moreover, for most cases of practical interest, $Q_C \gg Q_L$, inductor loss far exceeds capacitor loss and is the only loss component that needs to be considered. In this case:

$$\eta \approx 1 - \frac{Q_T}{Q_L} = 1 - \frac{\sqrt{\frac{R_p}{R_s} - 1}}{Q_L} \tag{3.20}$$

It is important to observe that the matching network efficiency depends only on the inductor quality factor and the transformation ratio if $Q_C \gg Q_L$. For a given inductor quality factor, there is an upper bound on the efficiency of a single-stage matching network as expressed in Eq. 3.20.

One route towards higher performance that is sometimes recommended is the use of a multi-stage matching network comprising a cascade of individual L-sections [32]. This can benefit both efficiency and bandwidth. Consider the n-stage matching network illustrated in Fig. 3.2. Using Eq. 3.20 and assuming that all inductors' Q_L are identical, we get:

$$\eta = (1 - \frac{Q_{T1}}{Q_L})(1 - \frac{Q_{T2}}{Q_L})....(1 - \frac{Q_{Tn}}{Q_L}) = \prod_{i=1}^{n}(1 - \frac{Q_{Ti}}{Q_L}) \tag{3.21}$$

where Q_{Ti} is the transformation quality factor of the n^{th} stage (corresponding to the transformation ratio of one stage in Eq. 3.1 and 3.2). For high efficiency of each stage we require $\frac{Q_{Ti}}{Q_L} \ll 1$, and find:

$$\eta \approx 1 - \frac{Q_{T1} + Q_{T2}....Q_{Tn}}{Q_L} = 1 - \frac{\sum_{i=1}^{n} Q_{Ti}}{Q_L} \leqslant 1 - \frac{n\,(\prod_{i=1}^{n} Q_{Ti})^{\frac{1}{n}}}{Q_L} \tag{3.22}$$

and from the formulas in [54], it can be shown that

$$\eta \approx 1 - \frac{n\,(\prod_{i=1}^{n} Q_{Ti})^{\frac{1}{n}}}{Q_L} \quad \textit{only when} \quad Q_{T1} = Q_{T2} = ... = Q_{Tn} \tag{3.23}$$

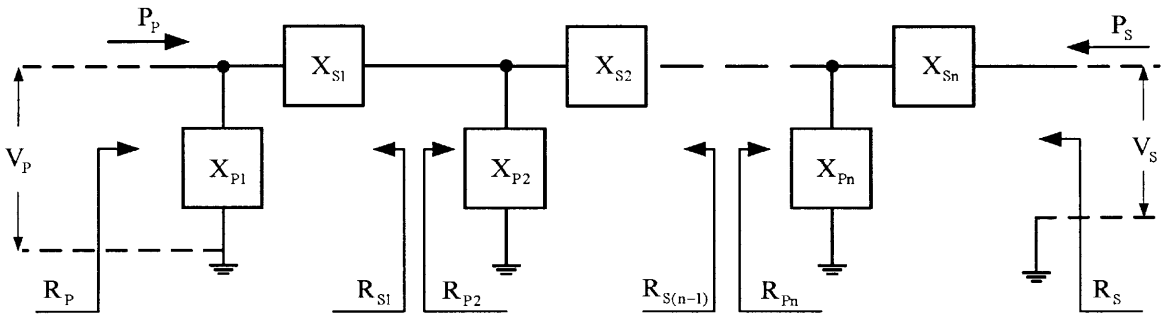

Figure 3.2: A multi-stage matching network.

Thus, for the optimal case of identical transformation ratios for each L-section stage, the transformation quality factors of all the stages is selected as

$$Q_{Ti} = \sqrt{\left(\frac{R_p}{R_s}\right)^{\frac{1}{n}} - 1} = \sqrt{\left(\frac{V_p}{V_s}\right)^{\frac{2}{n}} - 1} \tag{3.24}$$

and achieve an overall efficiency of

$$\eta \approx 1 - \frac{n}{Q_L}\sqrt{\left(\frac{R_p}{R_s}\right)^{\frac{1}{n}} - 1} \tag{3.25}$$

Considering Eq. 3.25, there is clearly an optimum number of stages n to maximize efficiency. This number is a function of the transformation ratio but not a function of inductor quality factor Q_L, assuming all inductors have an identical specified Q_L. Figure 3.3 plots the optimum number of L-section stages n_{opt} as a function of the voltage transformation ratio $\frac{V_p}{V_s}$. As transformation quality factor Q_T increases, the optimum number of stages approaches

$$n_{opt} \rightarrow \lceil \ln Q_T \rceil \tag{3.26}$$

and the efficiency approaches

$$\eta_{max} = 1 - \frac{nQ_T^{\frac{1}{n}}}{Q_L} \tag{3.27}$$

where Q_T is as defined in Eq. 3.2. These results indicate that using multi-stage design may improve the efficiency, especially when the desired transformation ratio is very large. But the efficiency reaches its maximum at a certain number of stages and will decrease for more stages.

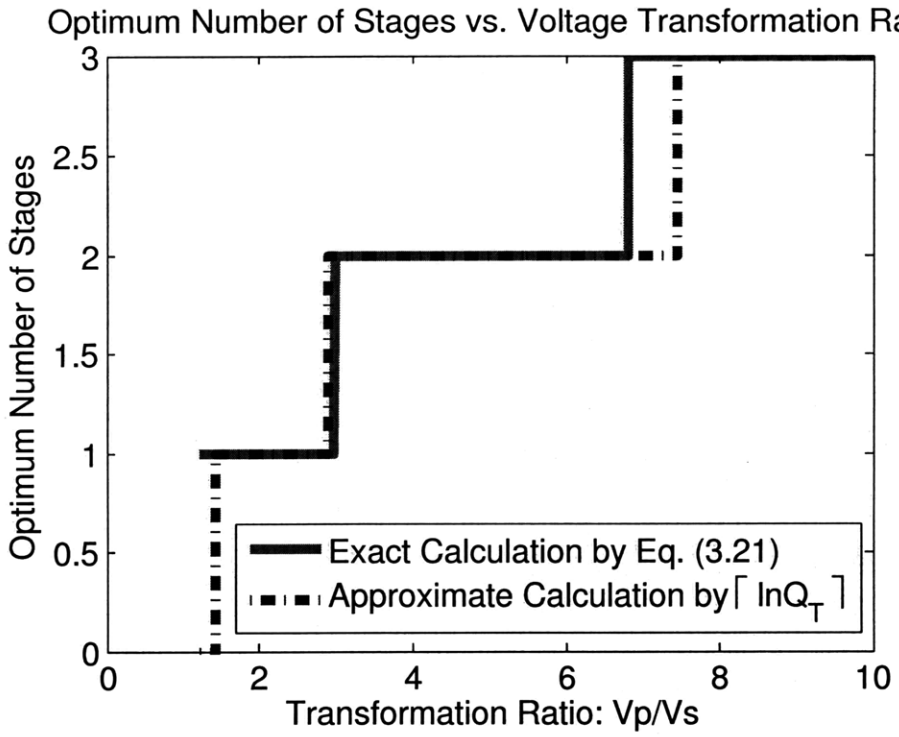

Figure 3.3: Optimum number of stages vs. transformation ratio.

3.3 Calculation and Simulation Results

The previous section showed that matching network efficiency can be expressed as a function of inductor quality factor Q_L and transformation ratio. To illustrate the implication, Fig. 3.4 plots predicted matching network efficiency vs. transformation ratio for three different inductor quality factors used in one-, two-, and three-stage designs. In all cases, matching network efficiency decreases with increasing transformation ratio, and decreases more rapidly with lower inductor quality factor. This is to be expected, given the forms of Eq. 3.20 and 3.25.

Figure 3.4 also illustrates how the optimal number of matching network stages changes with transformation ratio for a specified inductor Q_L. Consider the one, two and three-stage design curves for $Q_L = 60$. For a voltage transformation ratio of 2, a single-stage design has the highest efficiency. At a voltage transformation ratio of 5, a two-stage design has a significant advantage ($\sim$ 1.5%) in efficiency over a single-stage, and at a voltage transformation ratio of 8, the three-stage design is developing a marginal advantage over a two-stage design. Considering the tradeoffs at a voltage conversion ratio of 8, it can also be seen that if the space required to construct the three inductors for the three-stage

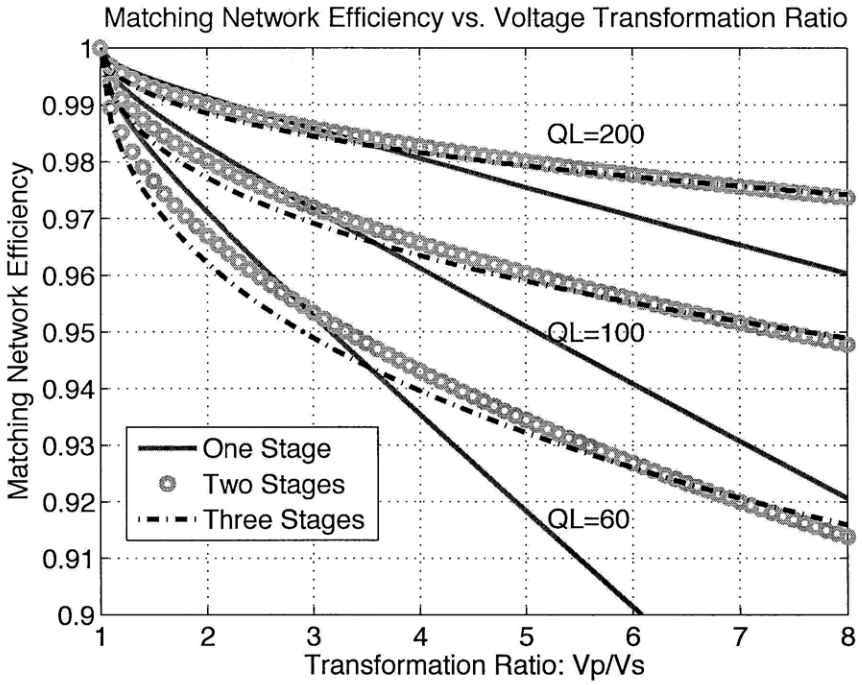

Figure 3.4: Matching network efficiency vs. transformation ratio V_p/V_s.

$Q_L = 60$ design can be employed to build a higher Q_L inductor for a single-stage design (e.g., $Q_L = 100$), then a single-stage design may still be preferable.[1] Thus, the optimal number of stages specified in Fig. 3.4 and Eq. 3.25 should only be considered an upper bound.

Figure 3.5 illustrates the predicted efficiency of a matching network for a typical voltage transformation ratio of 4 as a function of inductor quality factor Q_L (parameterized by the number of stages). In each curve, percentage loss is inversely proportional to Q_L (c.f. Eq. 3.20 and 3.25), leading to the observed asymptotic behavior. Thus, for a single-stage design, doubling quality factor Q_L from 100 to 200 yields an efficiency improvement from (approximately) 96% to 98%, and doubling Q_L again to 400 changes efficiency from 98% to 99%. Still greater loss reductions require proportionally higher inductor quality factors, and under those conditions the capacitor quality factor starts to be a consideration (limiting efficiency) as indicated in Eq. 3.19. Nevertheless, it may be concluded that for a $4:1$ voltage transformation ratio, it is possible to achieve high efficiency with inductors of reasonable quality factor. To further illustrate component sizing and efficiency, consider the design of matching networks having a voltage transformation ratio of $V_p : V_s = 4 : 1$. We assume $P_{in} = 25\ W$, $R_p = 50\ \Omega$, and $R_s = \frac{R_p}{16} = 3.125\ \Omega$.

[1] we address some inductor size and Q_L scaling issues in Chapter 5.

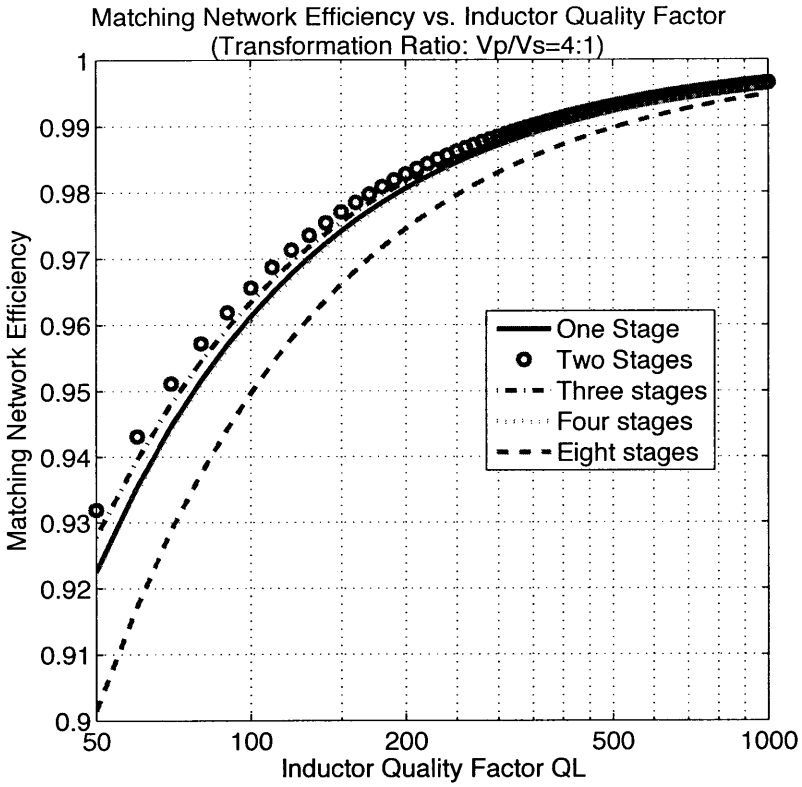

Figure 3.5: Matching network efficiency vs. inductor quality factor.

The component values for the matching networks of Fig. 3.1(a) and Fig. 3.1(b) are shown in Table 3.1 for frequencies of 25 MHz, 50 MHz and 100 MHz. For the multi-stage network in Fig. 3.2, we assume that the shunt components are all inductors, the series components are all capacitors, and the Q_i for each stage is the same. The component values for two- and four-stage designs are shown in Table 3.2.

Table 3.1: Component values for the matching networks of Fig. 3.1(a) and Fig. 3.1(b) for $R_p = 50\ \Omega$ and $R_s = 3.125\ \Omega$.

	Matching network in Fig. 3.1(a)		Matching network in Fig. 3.1(b)	
Frequency	L_s	C_p	L_p	C_s
25 MHz	77.1 nH	493 pF	82.2 nH	526 pF
50 MHz	38.5 nH	247 pF	41.1 nH	263 pF
100 MHz	19.3 nH	123 pF	20.6 nH	132 pF

Table 3.2: Component values for the multi-stage matching network in Fig. 3.2 for $R_p = 50\ \Omega$ and $R_s = 3.125\ \Omega$.

Matching network in Fig. 3.2, $n = 2$				
Frequency	L_{p1}	C_{s1}	L_{p2}	C_{s2}
25 MHz	184 nH	294 pF	45.9 nH	1176 pF
50 MHz	91.9 nH	147 pF	23.0 nH	588 pF
100 MHz	45.9 nH	73.5 pF	11.5 nH	294 pF

Matching network in Fig. 3.2, $n = 4$								
Frequency	L_{p1}	C_{s1}	L_{p2}	C_{s2}	L_{p3}	C_{s3}	L_{p4}	C_{s4}
25 MHz	318 nH	255 pF	159 nH	509 pF	79.6 nH	1019 pF	39.8 nH	2037 pF
50 MHz	159 nH	127 pF	79.6 nH	255 pF	39.8 nH	509 pF	19.9 nH	1019 pF
100 MHz	79.6 nH	63.7 pF	39.8 nH	127 pF	19.9 nH	255 pF	9.95 nH	509 pF

Efficiency results are listed in Table 3.3 for both calculated values using Eq. 3.20 and 3.21 and for simulations of the circuits in PSPICE . The simulation results show excellent agreement with the calculations. The maximum efficiency is about 98% when $Q_L = 200$ and approximately 93% when $Q_L = 60$. As expected, multi-stage matching networks don't provide a significant advantage (especially given the additional components required) because the required transformation ratio is not very large.

Table 3.3: Calculated and simulated results for the matching networks in Fig. 3.1 and Fig. 3.2.

		Fig. 3.1(a)		Fig. 3.1(b)		Fig. 3.2 n=2		Fig. 3.2 n=4	
Frequency	Q_L	$\eta_{sim}(\%)$	$\eta_{cal}(\%)$	$\eta_{sim}(\%)$	$\eta_{cal}(\%)$	$\eta_{sim}(\%)$	$\eta_{cal}(\%)$	$\eta_{sim}(\%)$	$\eta_{cal}(\%)$
25 MHz	60	93.6	93.6	93.6	93.6	94.1	94.3	93.2	93.5
	100	95.9	96.1	95.9	96.1	96.3	96.6	95.7	96.1
	200	97.7	98.1	97.7	98.1	97.9	98.3	97.6	98.0
50 MHz	60	93.6	93.6	93.6	93.6	94.1	94.3	93.2	93.5
	100	95.9	96.1	95.9	96.1	96.3	96.6	95.7	96.1
	200	97.7	98.1	97.7	98.1	97.9	98.3	97.6	98.0
100 MHz	60	93.6	93.6	93.6	93.6	94.1	94.3	93.2	93.5
	100	95.9	96.1	96.0	96.1	96.3	96.6	95.7	96.1
	200	97.7	98.1	97.7	98.1	97.9	98.3	97.6	98.0

3.4 Experimental Results

In order to verify the theoretical calculations of Eq. 3.20 and 3.25, experiments were carried out using the experimental setup of Fig. 3.6 (equipment indicated in Table 3.4). The test setup is designed to measure the performance of back-to-back connections of identical matching networks which transform impedance away from 50 Ω and back to 50 Ω. Cascading matching networks in this manner provides an increased loss which is easier to measure than that of a single network. Moreover, this method enables all power measurements to be made at 50 Ω with a single power meter, thus providing for more accurate calculation of efficiency than could be obtained otherwise.

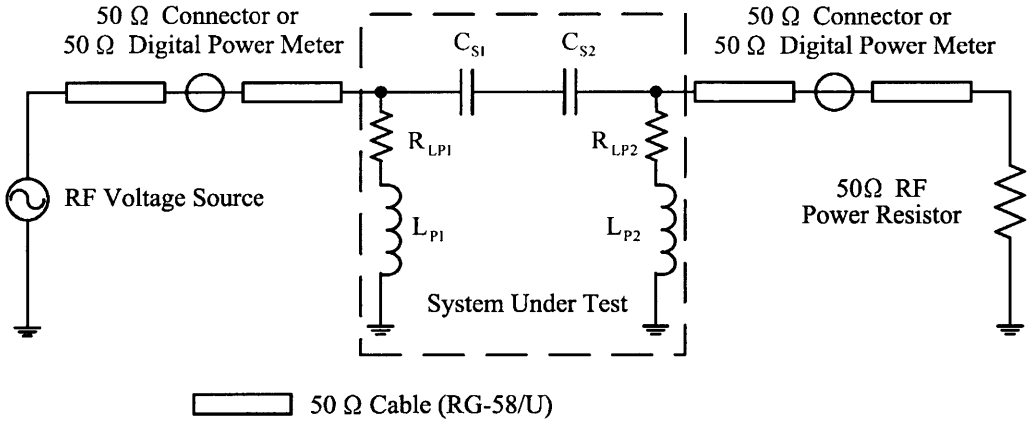

Figure 3.6: Experimental setup for validating matching network efficiency calculations. Equipment and component values are detailed in Tables 3.4 and 3.5. The 50 Ω power meter can be placed in either location indicated, as described in the experimental methods.

Table 3.4: Equipment used in the experimental setup of Fig. 3.6.

Equipment	Model
RF Voltage Source	Agilent 33250A Waveform Generator plus AR 150A100B Power Amplifier
Digital Power Meter	BIRD Digital RF Power Meter Model 5000-EX with Series 5010 Thruline Directional Power Sensor and 25 – 60 MHz DPM sense elements.
50 Ω RF Power Resistor	BIRD Termaline Coaxial Resistor 8401

To find matching network efficiency, the forward and reflected powers are measured, with the same power meter, as at each of the two locations indicated in Fig. 3.6, and it is verified that the reflected power is low, indicating a good impedance match. (A 50 Ω through connector is utilized in whichever location the power meter is not used.) The efficiency of

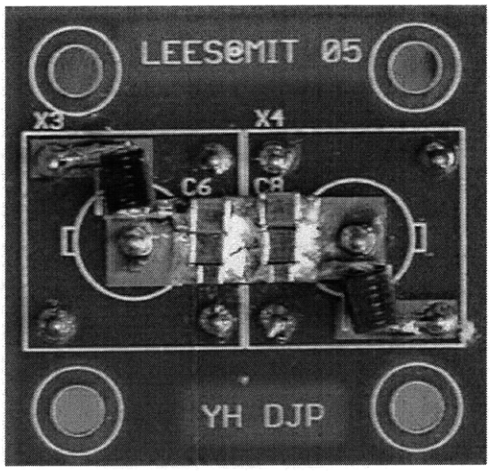

Figure 3.7: Experimental back-to-back matching network cascade used in the setup of Fig. 3.6. The illustrated circuit has a voltage transformation ratio to the intermediate node of 4.27 : 1. (Layout information for this circuit is presented in Appendix B.)

the matching network cascade is calculated as the ratio of the net power flow, forward minus reflected, measured at the load side to that measured at the source side. This measurement and calculation procedure eliminates scale factor errors in the power measurements, e.g., due to limits on absolute accuracy of the power meter.

Figure 3.7 shows a back-to-back matching network cascade for the test setup of Fig. 3.6. The matching network cascade has the topology indicated in Fig. 3.6 and is implemented on a printed circuit board with 50 Ω BNC connectors mounted on the back side of the board. Two such matching network cascades were developed, each designed for a matched input and output resistance of 50 Ω at 50 MHz. The first was designed for a voltage transformation ratio (to the intermediate node) of $V_p/V_s = 3.0$, while the second was designed for a voltage transformation ratio of 4.27 (selected for the ready availability of inductor values). Nominal and measured inductor and capacitor values are indicated in Table 3.5 along with measured circuit board parasitics.

The expected efficiency of the matching network cascade can be calculated as in Eq. 3.21:

$$\eta = (1 - \frac{Q_T}{Q_{LP1}})(1 - \frac{Q_T}{Q_{LP2}}) \tag{3.28}$$

For the matching network cascade with voltage transformation ratio to the intermediate node of $V_p/V_s = 3.0$, $Q_T = 2.83$ by Eq. 3.1 and 3.2. From Table 3.5, $Q_{LP1} = \omega L_{P1}/R_{LP1} = 85.88$, and $Q_{LP2} = \omega L_{P2}/R_{LP2} = 83.98$. This results in a calculated efficiency $\eta_{cal} = 93.44\%$. Note that this corresponds to an expected efficiency of each 3:1 stage of approximately 96.66%. Likewise, for the design with $V_p/V_s = 4.27$, $Q_T = 4.15$ by Eq. 3.1

and 3.2. From Table 3.5, $Q_{LP1} = \omega L_{P1}/R_{LP1} = 83.69$, and $Q_{LP2} = \omega L_{P2}/R_{LP2} = 81.93$, resulting in $\eta_{cal} = 90.21\%$.

Table 3.5: Component types and values for the experimental matching network cascade used in the test setup of Fig. 3.6. Measured values for circuit-board parasitics are also indicated. All measured values were obtained at a frequency of 50 MHz using an Agilent 4395A network/spectrum/impedance analyzer.

Component Values for Transformation Ratio $V_p/V_s = 3.00$					
Component Name	Nominal Value	Manufacturer and Part Style	Part Number	Measured Value	PCB Parasitic Capacitance Value
L_{P1}	56 nH	Coilcraft	1812SMS-56N	55.59 nH	$\approx$ 2.4 pF
R_{LP1}				0.197 Ω	
L_{P2}	56 nH	Coilcraft	1812SMS-56N	55.40 nH	$\approx$ 2.4 pF
R_{LP2}				0.201 Ω	
C_{S1}	100 pF × 2	CDE	MC12FA101J MC12FA101J	99.91 pF + 100.18 pF	$\approx$ 1.4 pF
C_{S2}	100 pF × 2	CDE	MC12FA101J MC12FA101J	101.82 pF + 100.42 pF	$\approx$ 1.4 pF
Component Values for Transformation Ratio $V_p/V_s = 4.27$					
Component Name	Nominal Value	Manufacturer and Part Style	Part Number	Measured Value	PCB Parasitic Capacitance Value
L_{P1}	39 nH	Coilcraft	1812SMS-39N	37.86 nH	$\approx$ 2.4 pF
R_{LP1}				0.139 Ω	
L_{P2}	39 nH	Coilcraft	1812SMS-39N	38.03 nH	$\approx$ 2.4 pF
R_{LP2}				0.143 Ω	
C_{S1}	100 pF × 2 + 68 pF + 6 pF	CDE	MC12FA101J MC12FA101J MC12FA680J MC08CA060D	99.86 pF + 102.02 pF + 69.64 pF + 5.99 pF	$\approx$ 1.4 pF
C_{S2}	100 pF × 2 + 68 pF + 6 pF	CDE	MC12FA101J MC12FA101J MC12FA680J MC08CA070D	99.84 pF + 102.27 pF + 69.67 pF + 6.91 pF	$\approx$ 1.4 pF

Table 3.6: Experimental results for the matching network cascade with an intermediate voltage transformation Ratio $V_p/V_s = 3.00$.

$P_{Fwd}(W)$	$P_{Ref}(W)$	$P_{in}(W) = P_{Fwd} - P_{Ref}$	$P_{out}(W)$	$\eta_{exp}(\%) = P_{out}/P_{in}$	$\eta_{cal}(\%)$
5.15	0	5.15	4.85	94.18	93.44
10.60	0	10.60	9.80	92.45	
15.40	0	15.40	14.40	93.51	
20.20	0.04	20.16	18.60	92.26	
26.30	0.05	26.25	24.50	93.33	
30.20	0.07	30.13	28.00	92.93	
35.90	0.08	35.82	33.45	93.38	
42.30	0.10	42.20	39.30	93.13	
46.45	0.12	46.33	43.30	93.46	
50.00	0.13	49.87	46.50	93.24	
Average $\eta_{exp}(\%)$				93.29	

The experimental results for the two designs are shown in Tables 3.6 and 3.7. All data were measured with the rf digital power meter. P_{Fwd} is the input forward power to the matching network cascade. Due to the component tolerances and printed circuit board parasitics, there is a small amount of mismatch between the 50 Ω cable and the matching network input, resulting in a small reflected power measured by the power meter. The net input power is calculated as $P_{in} = P_{Fwd} - P_{Ref}$. Because the load is a tightly specified 50 Ω resistor and it matches well with the cable, there is no measured reflected power from the load resistor. Ten groups of data at different power levels were acquired for each design. The efficiencies are averaged to reduce the effects of sensor limitations. The average experimental efficiencies η_{exp} are very close to the theoretical results η_{cal}. η_{cal} is a little higher, at least in part, because the capacitor losses aren't considered in Eq. 3.28. From the capacitor data sheet, capacitor quality factor is roughly 1000, which accounts for 0.3% efficiency loss ($V_p/V_s = 3.00$) and 0.4% efficiency loss ($V_p/V_s = 3.00$) in a single-stage matching network accounting for much of the small differences between calculated and experimental results. Still more accurate calculation results can be achieved by Eq. 3.16 and 3.18. Experimental measurements thus confirm the accuracy of the models for matching network efficiency introduced in Section 3.2.

It is also useful to consider the difference between the experimental results with a 3 : 1 and a 4.27 : 1 (intermediate) voltage transformation ratio. The design for the 4.27 : 1 case resulted in a higher percentage of reflected power at the matching network input, corresponding to a larger mismatch between the desired 50 Ω and the driving point impedance provided by the matching network cascade. This may be attributed both to the higher losses and the higher transformation quality factor Q_T in the 4.27 : 1 case. As Q_T increases, the design

Table 3.7: Experimental results for the matching network cascade with an intermediate voltage transformation ratio $V_p/V_s = 4.27$.

$P_{Fwd}(W)$	$P_{Ref}(W)$	$P_{in}(W) = P_{Fwd} - P_{Ref}$	$P_{out}(W)$	$\eta_{exp}(\%) = P_{out}/P_{in}$	$\eta_{cal}(\%)$
5.40	0.24	5.16	4.60	89.15	90.21
10.60	0.49	10.11	9.15	90.50	
15.80	0.75	15.05	13.50	89.71	
20.48	0.98	19.50	17.30	88.72	
25.00	1.20	23.80	21.41	89.96	
30.35	1.47	28.88	26.03	90.13	
34.36	1.66	32.70	29.61	90.56	
40.66	1.98	38.68	34.68	89.67	
45.55	2.22	43.33	38.95	89.89	
50.65	2.48	48.17	43.34	89.97	
Average $\eta_{exp}(\%)$				89.92	

provides an increasingly narrow frequency band over which the desired impedance match is provided, and the impedance match becomes more sensitive to component tolerances. This suggests that the use of higher-order matching networks may be motivated by concerns other than efficiency if large transformation ratios are desired.

3.5 Conclusion

This chapter (based on the author's publication [34]) presents analysis and design considerations for lumped (inductor and capacitor) matching networks operating at high efficiency ($> 95\%$). Formulas (c.f. Eq. 3.19, 3.20 and 3.25) for calculating matching network efficiency are given, and it is shown that efficiency can be expressed as a function of inductor quality factor Q_L, capacitor quality factor Q_C and transformation ratio. These formulas are used to evaluate the optimum number of L-section matching stages as a function of conversion ratio. Both simulation and experimental results are presented that validate the analytical formulation. For a typical required voltage transformation ratio of $3 - 5$ (e.g., for a resonant dc/dc power converter design), one can expect to achieve matching network efficiencies between 96% and 98.5% for inductor quality factors of $100 - 200$. Efficiency can be improved through higher quality factor magnetics, but efficiencies exceeding 99% are likely to be challenging to achieve with this approach.

Chapter 4

Evaluation of Magnetic Materials for Very High Frequency Power Applications

---

THIS chapter investigates the loss characteristics of rf magnetic materials for power conversion applications in the 10 MHz to 100 MHz range. A measurement method is proposed that provides a direct measurement of inductor quality factor Q_L as a function of inductor current at rf frequencies, and enables indirect calculation of core loss as a function of flux density. Possible sources of error in measurement and calculation are evaluated and addressed. The proposed method is used to identify loss characteristics of several commercial rf magnetic core materials. The loss characteristics of these materials, which have not previously been available, are illustrated and compared in tables and figures. The use of the method and data are demonstrated in the design of a magnetic-core inductor, which is applied in a 30 MHz inverter. The results of this chapter are thus useful for design of magnetic components for very high frequency (VHF) applications.

4.1 Background

There is a growing interest in switched-mode power electronics capable of efficient operation at very high switching frequencies (e.g., 10 – 100 MHz). Power electronics operating at such frequencies include resonant inverters [1, 11, 18, 21, 38, 55–59] (e.g., for heating, plasma generation, imaging, and communications) and resonant dc-dc converters [8, 10–13, 15, 38, 41, 60–63] (which utilize high frequency operation to achieve small size and fast transient response.) These designs utilize magnetic components operating at high flux levels, and often under large flux swings. Moreover, it would be desirable to have improved magnetic components for rf circuits such as matching networks [32–34, 46, 53]. There is thus a need for magnetic materials and components suitable for operation under high flux swings at frequencies above 10 MHz.

Unfortunately, most magnetic materials exhibit unacceptably high losses at frequencies above a few megahertz. Moreover, the few available bulk magnetic materials which are potentially suitable for frequencies above 10 MHz are typically only characterized for small-

signal drive conditions, and not under the high flux-density conditions desired for power electronics. This motivates better characterization of magnetic materials for high-frequency power conversion applications.

This chapter investigates the loss characteristics of several commercial rf magnetic materials under large-signal ac flux conditions for frequencies above 10 MHz. A measurement method is proposed that provides a direct, accurate measurement of inductor quality factor Q_L as a function of ac current amplitude at rf frequencies. This method also yields an accurate measurement of loss density of a core material as a function of flux density at rf frequencies. We use this technique to identify the loss characteristics of several different rf magnetic materials at frequencies up to 70 MHz.

Section 4.2 of the chapter introduces a method for accurately measuring the quality factor of rf inductors under large signal drive conditions. Section 4.3 shows how to utilize these measurements to identify core loss characteristics as a function of flux density and frequency. In Section 4.4, we employ these techniques to identify the loss characteristics of several commercial rf magnetic-core materials. These loss characteristics, which have not previously been available except to the authors, are presented and compared in tables and figures. Section 4.5 illustrates the application of this data in the design of a resonant inductor, which is applied in a 30 MHz resonant inverter. Finally, Section 4.6 concludes the chapter.

4.2 Measuring the Quality Factor of RF Inductors

4.2.1 Measurement Circuit and Principles

The quality factor Q_L of a magnetic-core inductor is a function of both operating frequency and ac current (or flux) level. We utilize a measurement circuit that enables Q_L to be determined at a single specified frequency across a wide range of drive levels. Inductor quality factor is simply determined as the ratio of amplitudes of two ground-referenced voltages in a resonant circuit. A schematic of the measurement circuit is shown in Fig. 4.1. L, R_{cu} and R_{core} model the inductor to be evaluated: L is its inductance, R_{cu} represents its copper loss and R_{core} represents its core loss at a single frequency. R_C and C model a resonant capacitor selected to resonate with the inductor at the desired frequency. C is its capacitance and R_C represents its equivalent series resistance. The input voltage V_{in} should ideally be a pure sinusoidal wave, and is generated by a signal generator and a rf power amplifier. The amplitude and frequency of V_{in} can be tuned by the signal generator.

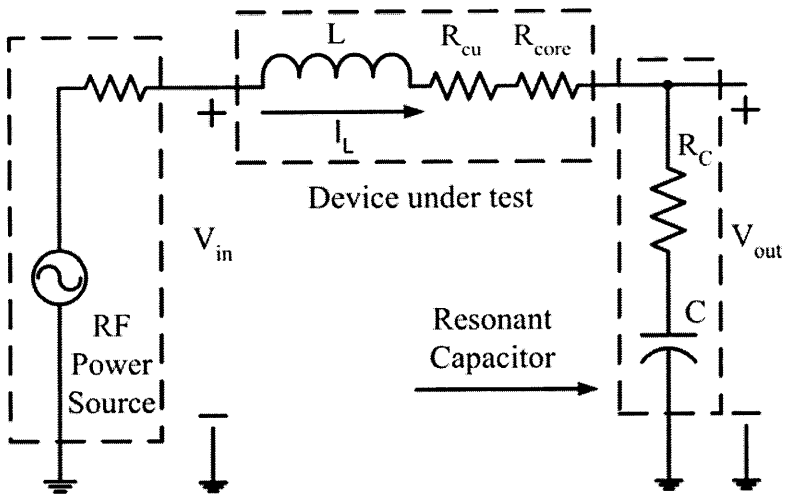

Figure 4.1: Schematic of the circuit for measuring inductor quality factor, which can be calculated as the amplitude ratio V_{out-pk} over V_{in-pk}.

To understand how this circuit enables direct measurement of inductor Q_L , consider that at the resonant frequency:

$$f_s = \frac{\omega_s}{2\pi} = \frac{1}{2\pi\sqrt{LC}} \tag{4.1}$$

the ratio between the output voltage amplitude V_{out-pk} and the input voltage amplitude V_{in-pk} is:

$$\frac{V_{out-pk}}{V_{in-pk}} = \left|\frac{V_{out}(j\omega_s)}{V_{in}(j\omega_s)}\right| = \left|\frac{R_C + \frac{1}{j\omega_s C}}{R_{core} + R_{cu} + R_C}\right| \approx \frac{\omega_s L}{R_{core} + R_{cu}} = Q_L \tag{4.2}$$

The final approximation in Eq. 4.2 is accurate for the case in which R_C is small compared to $R_{cu} + R_{core}$ and to $\frac{1}{j\omega_s C}$, and becomes precisely true when $R_C = 0$. The above equation shows that the ratio of V_{out-pk} and V_{in-pk} is approximately equal to the quality factor of the inductor at the resonant frequency. Probing the two voltages enables direct determination of inductor Q_L . Drive level can be adjusted by varying the amplitude of the rf source. The current of the inductor is equal to the capacitor current and can be calculated from the output voltage and the known capacitor impedance. (These considerations motivate the use of high-precision low loss capacitors such as mica or porcelain capacitors. In experiments, we have employed microwave porcelain multilayer capacitors from American Technical Ceramics.)

One subtlety with this measurement method is the challenge of knowing the precise resonant frequency (for which Eq. 4.1 and 4.2 apply). Given the small values of inductance that are typically of interest in the 10 – 100 MHz range (e.g., inductances of tens to hundreds of

nanoHenries [6,38,64]), and the correspondingly small values of resonant capacitances (tens to hundreds of picoFarads), parasitic capacitances of the measurement circuit and voltage probes can have a significant impact on the resonant frequency. Considering these influences, the resonant frequency may have up to a 5% deviation from its calculated theoretical value.

To address this issue, we pre-calculate the capacitor value to achieve the approximate resonant frequency, then adjust the frequency around the calculated resonant frequency to find the frequency point f_s' where $\frac{V_{out-pk}}{V_{in-pk}}$ has the maximum value. Let $R_L = R_{cu} + R_{core}$ represent the total source of loss in the inductor. R_C is ignored in Eq. 4.3, 4.4 and 4.5 as it is usually much smaller than R_L. From (4.2), the derivative of $\frac{V_{out-pk}}{V_{in-pk}}$ with respect to frequency is:

$$\frac{d}{d\omega}\left(\frac{V_{out-pk}}{V_{in-pk}}\right) = -\omega C \frac{CR_L^2 + 2L(\omega^2 LC - 1)}{[\omega^2 C^2 R_L^2 + (\omega^2 LC - 1)^2]^{1.5}} \tag{4.3}$$

Setting $\frac{d}{d\omega}\left(\frac{V_{out-pk}}{V_{in-pk}}\right) = 0$, we find that $\frac{V_{out-pk}}{V_{in-pk}}$ reaches its maximum value at a frequency:

$$f_s' = \frac{\omega_s'}{2\pi} = \frac{1}{2\pi}\sqrt{\frac{1}{LC} - \frac{R_L^2}{2L^2}} \tag{4.4}$$

From (4.1) and (4.2),

$$f_s' = f_s\sqrt{1 - \frac{1}{2Q_L^2}} \tag{4.5}$$

As $Q_L \gg 1$ for all cases of interest, this actual operating frequency f_s' is approximately equal to the resonant frequency f_s. (The effect of the difference in frequency will be addressed in Section 4.3)

4.2.2 Measurement Procedures

Before beginning the measurements, an inductor is fabricated based on the frequencies and the range of flux density amplitude B_{pk} of interest. The step-by-step measurement procedures are as follows:

1. Measure the inductance: At the resonant frequency f_s, both the inductance L and the quality factor Q_L of the fabricated inductor are measured (under small-signal conditions) using an impedance analyzer. From the measured L, the resonant capacitor value can be calculated. From the measured small-signal Q_L, the expected quality factor under high-power conditions (which should be smaller than the measured small signal Q_L) can be estimated. Though the measurement is under very low drive conditions, the core loss

can't be ignored for some materials, so this small-signal Q_L measurement may reflect both core and copper loss.

2. Calculate the relative permeability μ_r: Though most core companies will specify the relative permeability μ_r of the material, μ_r should be measured and calculated to get an accurate value. Assuming that the inductor core is toroidal, from [47]we gets:

$$\mu_r \approx \frac{2\pi L}{N^2 h \mu_0 \ln\left(\frac{d_o}{d_i}\right)} \tag{4.6}$$

where L is the inductance measured in step 1), h, d_o and d_i are the height, the outer diameter and the inner diameter of the inductor, and N is the number of turns of the inductor. To minimize the error caused by the inductance of a single turn loop [47] and leakage flux, N should be as large as possible in a single layer. (In our experiments, we often fabricate and measure another inductor with the same core but a high turns number (> 20) specifically to reduce the single turn inductance error and get an accurate value of μ_r.)

3. Select resonant capacitor: The resonant capacitor value C can be calculated from Eq. 4.1. C should be much larger than the potential parasitic capacitance and the probe capacitance. The precise value C and ESR R_C of the capacitor is also measured using an impedance analyzer. Q_C can be calculated from C and R_C. We assume Q_C is constant during all the measurements. When Q_C is 1000 or higher, it may be difficult to accurately measure its value. In this case, Q_C may be estimated based on data sheet values. Q_C should be ten times larger than Q_L to minimize its influence on the Q_L measurement and the loss extraction.

4. Fabricate the resonant circuit: The printed circuit board should be designed carefully to minimize parasitic inductance and capacitance. A transformer or a low-pass filter of the drive input may be needed to reduce the distortion of the input voltage V_{in}. Layout of the resonant circuit is illustrated in Appendix C.

5. Calculate the required V_{out}: The inductor current amplitude I_{L-pk} can be calculated from B_{pk} and the inductors parameters. For example, the I_{L-pk} of a toroidal inductor can be calculated as:

$$I_{L-pk} = \frac{\pi(d_o + d_i)B_{pk}}{2\mu_r \mu_0 N} \tag{4.7}$$

where B_{pk} is the flux density amplitude in the toroidal core. I_{L-pk} is also the current amplitude of the resonant capacitor. The output voltage amplitude V_{out-pk} can be calculated from I_{L-pk} and the impedance of the resonant capacitor:

$$V_{out-pk} = \frac{I_{L-pk}}{2\pi f_s C} = \frac{(d_o + d_i)B_{pk}}{4 f_s C \mu_r \mu_0 N} \tag{4.8}$$

Using Eq. 4.7 and 4.8 to calculate I_{L-pk} and V_{out-pk} might not be accurate if μ_r varies significantly with flux density. In such cases, given that there are probes on voltage on both sides of the inductor, inductor voltage could be calculated and integrated to get flux linkage and thus a flux density measurement independent of permeability. In our measurements, we found μ_r to be almost constant across drive level because the actual operating frequency f_s' changed very little ($< 1\%$) with flux density variation (see Step 7). So the variation of permeability with flux density was not an issue in our data set.

6. Set up the experiment: The experimental setup comprises a signal generator, a rf power amplifier, and an oscilloscope in addition to the fabricated resonant circuit. The signal generator drives the power amplifier to produce a sinusoidal voltage with a variable amplitude and a tunable frequency. In the system, we employ an Agilent 33250A signal generator and an AR 150A100B rf power amplifier. The output of the amplifier is connected to the input of the resonant circuit by a matched cable, with any impedance transformation and/or filtering applied at the resonant circuit input. In the system, we typically employ an AVTECH AVX-M4 transmission line transformer (50 : 3 impedance transformation ratio) to better match the 50 Ω power amplifier to the low-impedance resonant circuit. we also often incorporate a low-pass filter (RC) to reduce the voltage distortion at the resonant circuit input.

   Note that the capacitance of the probe that measures the output voltage should be as small as possible, as it adds to the resonant capacitor value. The capacitance of the probe to measure the input voltage doesn't influence the measurement results.

7. Measure a set of V_{in-pk} and V_{out-pk}: The signal frequency is initially set to the calculated value of the resonant frequency f_s. However, due to parasitics, probe capacitance and component errors, this frequency is not exactly equal to the resonant frequency f_s. While adjusting the circuit to maintain the designed V_{out-pk} according to Eq. 4.8, tune the input signal frequency finely and search for the minimum V_{in-pk}. The frequency where V_{in} reaches its minimum is f_s' which is close to f_s when Q_L is high.

   Because the resonant circuit is highly tuned, the output voltage will be a very good sinusoidal waveform. However, because both the input power and input voltage V_{in} are small, the power amplifier may work in a nonlinear region and a distorted V_{in} may be observed. In this case, a transformer or a low-pass filter at the resonant circuit input can help to reduce the distortion. If the distortion can't be ignored, the amplitude of V_{in} at f_s' can be calculated numerically by Fourier analysis. Using the tuning characteristics, we can also determine if μ_r varies significantly with current level. If μ_r changes, the inductance will change and the tuned resonant frequency f_s' will also change. If this happens, the inductance L and the relative permeability μ_r need to be recalculated based on the resonant capacitor value C and the tuned f_s' . Knowing V_{in-pk} and V_{out-pk}, Q_L can be calculated from Eq. 4.2.

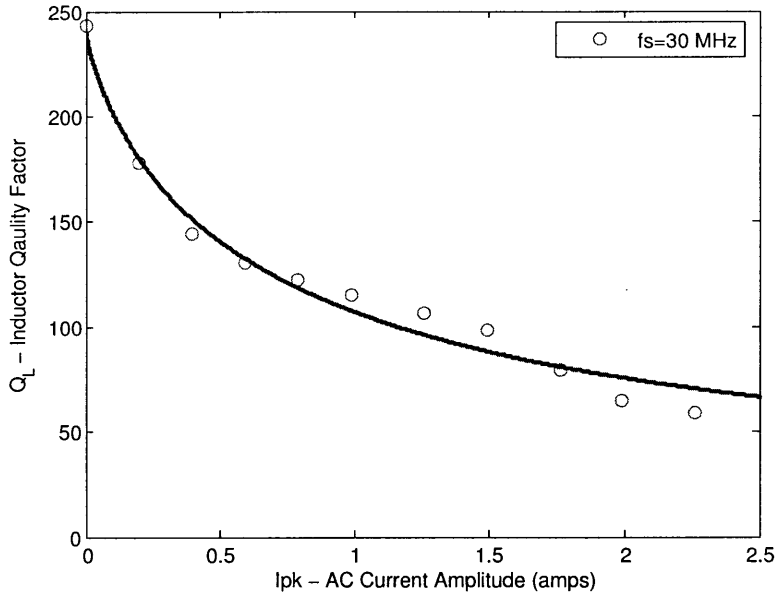

Figure 4.2: The Q_L of an inductor fabricated with an M3 toroidal core (OD = 12.7 mm, ID = 7.82 mm, Ht = 6.35 mm) with $N = 5$ turns of 116 mil wide and 4 mil thick foil, and $L = 190$ nH.

Fig. 4.2 shows a representative curve of Q_L vs. current drive level at 30 MHz for a 190 nH inductor wound with 5 turns of foil (0.116 in wide and 4 mil thick) on an M3 ferrite core. The strong variation of Q_L with ac current level (owing to core loss) is readily observed.

4.3 Extraction of Loss Characteristics of Commercial RF Magnetic Cores

In this section we show how the quality factor measurements of Section 4.2 can be adapted to identify core loss characteristics of magnetic materials. We do not seek to identify or model the underlying cause of core losses [65, 66]. Rather, we focus on quantitatively identifying the power loss density of a given magnetic material as a function of flux density under sinusoidal excitation at a specified frequency. Numerous works illustrate how this information can be used in the design of magnetic components, even for systems with complex excitations [67–69].

Methods and guidelines exist for direct measurement of core loss through voltage and current measurements made on multi-winding structures [70–72]. However, these methods rely on very accurate measurement of phase relationships between voltages and currents, which becomes increasingly hard to do as frequency increases. Instead, we exploit an indirect

method: Starting with an accurate measurement of total inductor loss (from accurate measurement of inductor Q_L), we seek to extract the portion of loss owing to the magnetic core. In the subsections that follow, we describe preparations and measurements of single-layer, foil-wound toroids (of materials to be tested), from which core loss information can be extracted.

4.3.1 Design and Fabrication of Low-loss Inductors with Toroidal Cores

To identify the loss characteristics of a magnetic-core material, the quality factors of inductors fabricated with appropriate magnetic cores are measured under large-signal drive conditions. We focus on ungapped toroidal magnetic cores due to the availability of these cores, the simplicity and uniformity of the calculations, and the magnetic self shielding provided by this core type. Also, the core loss to winding loss ratio is higher in this core type than in other available geometries.

The fabricated inductor should have as small a copper loss as possible compared to its core loss in order to minimize error. For this reason, we utilize a single-layer copper foil winding on the toroidal core. (Even more sophisticated construction techniques are possible [47], but are not used here.)

The copper foil is cut in the shape of a narrow strip. The following equations show the parameters of the copper strip and fabricated inductor.

$$N \approx \sqrt{\frac{2\pi L}{h\mu_r\mu_0 \ln\left(\frac{d_o}{d_i}\right)}} \tag{4.9}$$

where N is the number of turns, L is the inductance, μ_r is the relative permeability of the magnetic material, μ_0 is the permeability of free space, and h , d_i and d_o are the height, inner diameter and outer diameter of the toroidal core. Note that the thickness t_{cu} of the foil should be much larger than a skin depth in order to get the minimum resistance:

$$t_{cu} > \delta = \sqrt{\frac{\rho_{cu}}{\pi\mu_0 f_s}} \tag{4.10}$$

where ρ_{cu} is the electrical conductivity of copper.

The width of the copper foil is selected as:

$$w_{cu} \approx \frac{\pi d_i}{N} \tag{4.11}$$

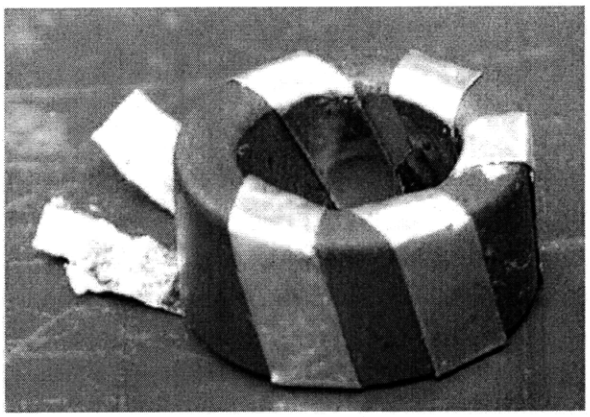

Figure 4.3: An example of an inductor fabricated from copper foil and a commercial magnetic core.

to achieve the desired number of turns. In fabrication, a value of w_{cu} is a little smaller than the above value is employed to leave a space between the turns of the foil winding.

The foil winding length is approximately:

$$l_{cu} = N(2h + d_o - d_i) \tag{4.12}$$

where the length l_{cu} of foil does not include the length of extra copper terminals to be soldered on the PCB pad. Because the relative permeability μ_r of the magnetic core is high (> 4) and the toroidal inductor is self-shielded, we assume that most of the flux is inside the core. Fig. 4.3 shows an inductor fabricated by the above method. The core is M3-998 from National Magnetics Group.

4.3.2 The Extraction of Core Loss Characteristics from the Measurement Results

The core loss characteristics can be extracted from the measured value of Q_L (based on V_{in-pk}, V_{out-pk} and f_s'). The measured quality factor Q_L provides a measure of the total loss. By subtracting out an estimate of the copper loss, we are left with an estimate of the core loss (and core loss density).

Referring to Fig. 4.1, we have:

$$Q_L \approx \frac{V_{out-pk}}{V_{in-pk}} = \frac{2\pi f_s L}{R_{core} + R_{cu} + R_C} \tag{4.13}$$

and

$$R_{core} = \frac{2\pi f_s L V_{in-pk}}{V_{out-pk}} - R_C - R_{cu} \tag{4.14}$$

The resistance of the resonant capacitor R_C can be measured by an impedance analyzer or acquired through the data sheet. It is more difficult to establish the exact value of R_{cu}. We employ the following method estimate the value for R_{cu}. We fabricate a coreless inductor with the same dimension and measure its R_{cu} using an impedance analyzer. From finite element simulation results in Appendix D, this value is close to the R_{cu} of a magnetic-core inductor for $\mu_r < 4$. When $\mu_r \geq 4$, the value of R_{cu} for a coreless inductor can be lower than the R_{cu} of a magnetic-core inductor by up to 30%. So we consider that this estimation of Rcu has up to 30% error. In our experiments, the core loss is controlled to be at least 5 times larger than the copper loss to reduce the error caused by R_{cu}.

With a value for R_{core}, the average core loss can be calculated. We express our results as core loss per unit volume as a function of flux density.

$$P_V = \frac{I_{L-pk}^2 R_{core}}{2V_L} \tag{4.15}$$

where V_L is the volume of the core. Because B_{pk} is specified, one data point of P_V (mW/cm^3) versus B_{pk} (Gauss) is acquired.

4.3.3 The Estimation of Errors

Possible errors in this procedure are discussed below:

1. Error caused by the capacitor ESR: As indicated in Eq. 4.2, capacitor ESR influences the voltage ratio, making it deviate from the desired Q_L value. Capacitor ESR R_C can be measured by an impedance analyzer. When R_C is too small to be measured accurately (e.g., $Q_L > 1000$), the error due to R_C can be estimated. For example, if $Q_L = 100$ and $Q_C > 1000$ by measurement, we estimate Q_C as about 2000 and the error in Q_L caused by R_C will be approximately 5%.

2. Error caused by circuit parasitics: As described preciously, the values of the resonant capacitor and the inductor are controlled to be much larger than the circuit parasitic capacitance or inductance to minimize their influence on the resonant frequency f_s. However, the parasitics can have a very poor Q, (i.e., relatively a high series ac resistance and low parallel ac resistance) which add extra losses. The error can be further reduced by a careful layout. The pads of the resonant inductor should be as close as possible to the

pads of the resonant capacitor and the measurement points to reduce the trace inductance and resistance. The resonant capacitor should be also connected to the ground tightly to reduce parasitic series resistance and inductance. With sufficient effort, error due to these parasitics can be made negligibly small and is not considered further.

3. The error caused by copper loss: The error caused by the copper loss (represented by resistance R_{cu}) can be a severe problem if $R_{core} \leq R_{cu}$. An exact value for the winding resistance R_{cu} is hard to determine. However, if $R_{core} \gg R_{cu}$, the error introduced by inaccuracies in the estimated value of R_{cu} is small. For example, if $R_{core} \geq 5R_{cu}$ and an error of up to 30% in the estimate of R_{cu} occurs, the R_{core} error caused by R_{cu} will be less than 5%.

4. Error caused by the actual operating frequency f_s': Though the difference between f_s' and f_s is small when Q_L is high, the error should be analyzed carefully. Assume the error between the resonant frequency f_s and actual operating frequency f_s' is 1%. While V_{out-pk} is constant, the error of the inductors current is about 1% and the error of the flux density in the inductor core is 1%. If $P_V \propto f_s^{\xi} B_{pk}^{\beta}$, and both ξ and β are about 2.6 to 2.8, the error of P_V will be less than 5.6%. However, the error can be compensated for by knowing f_s' and the approximate value of Q_L.

5. Error caused by uneven flux density: The flux density in a toroidal core is not even, which means the inner part of the core has more power loss than the outer part. This error depends on the dimensions of the core, mainly determined by the ratio of d_o and d_i. For $d_o = 2d_i$ and $\beta = 2.8$, the error is about 10%. However, the error can be also compensated (see [70], for example).

6. The total error: Considering all these error factors, the total error will be less than 20% if the inductor and the circuit are well designed and fabricated, $R_{core} \ll R_{cu}$, and the measurement is done carefully.

4.4 Core Loss Measurements in Commercial Magnetic Materials

Here we apply the proposed methods to identify the large signal loss characteristics of several commercial rf magnetic materials. The loss characteristics of these materials under large flux-swing condition have not been previously available, and are expected to be useful for design of rf power magnetic components. Table 4.1 shows the magnetic materials for which data will be provided. The loss characteristics of the materials listed in Table 4.1 are plotted in Figs. 4.4 to 4.8. At 20 MHz, the core loss of -17 material is too small to be measured and extracted. Moreover, it has a useful range extending to higher frequencies.

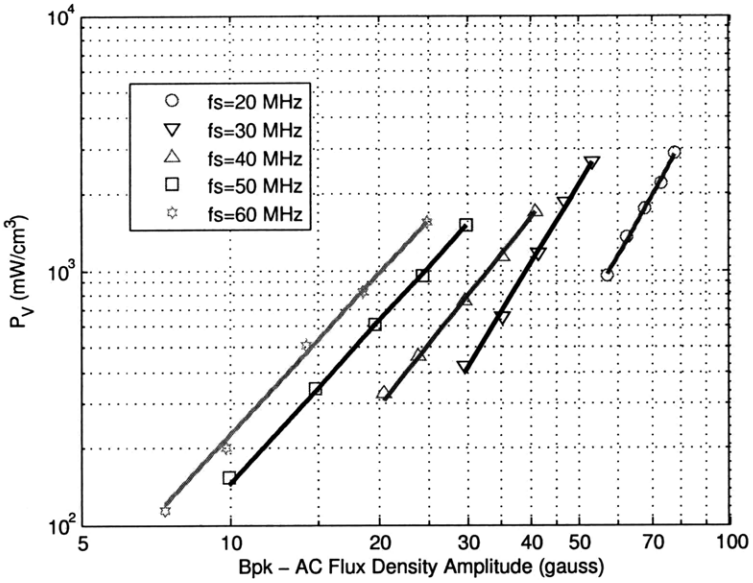

Figure 4.4: M3 material core loss vs ac flux density.

Thus we measured it in a somewhat different range. In Figs. 4.4 to 4.8, the Steinmetz equation $P_V = KB_{pk}^{\beta}$ for B_{pk} in Gauss and P_V in mW/cm^3 is used to fit the data. Table 4.2 shows K and β for each of these materials.

4.5 Application Example

To demonstrate application of the measurement techniques, methods and evaluated magnetic materials in rf power conversion, a magnetic-core inductor has been designed and fabricated to replace the original coreless resonant inductor L_S in a VHF (very high frequency) $\Phi 2$ inverter [55]. Fig. 4.9 shows the inverter topology [55]. The switching frequency of the inverter is 30 MHz, and operation is demonstrated with an input voltage of 100 V and an output power of 100 W.

Table 4.1: Materials, suppliers and specifications

Material	Type	Supplier	Permeability
M3	NiZn	National Magnetics Group	12
P	CoNiZn	Ferronics	40
67	NiZn	Fair-rite	40
N40	NiZn	Ceramic Magnetics	15
-17	Powered Iron	Micrometals	4

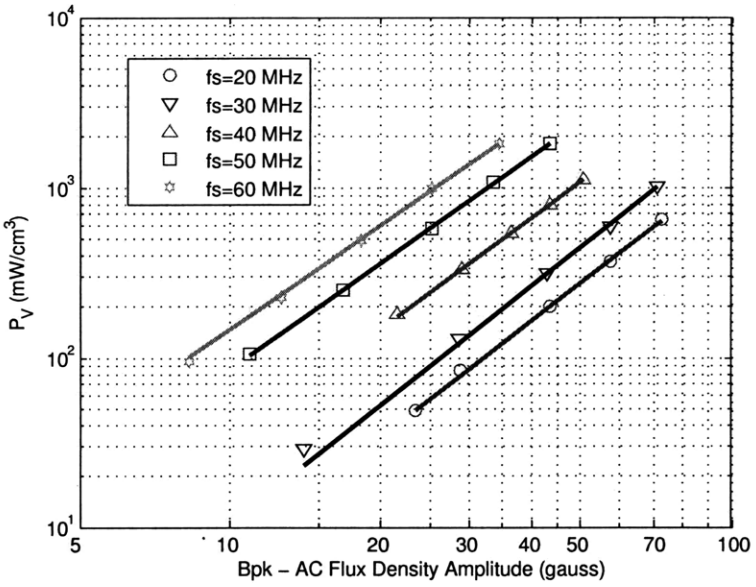

Figure 4.5: P material core loss vs ac flux density.

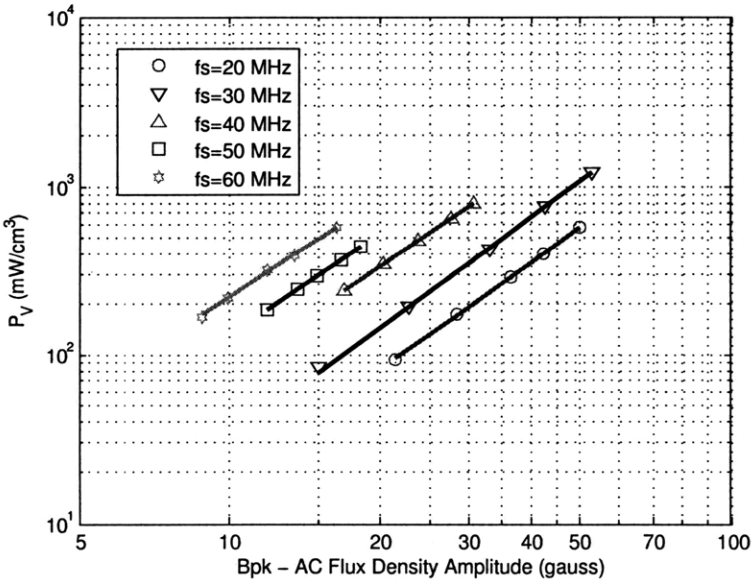

Figure 4.6: 67 material core loss vs ac flux density.

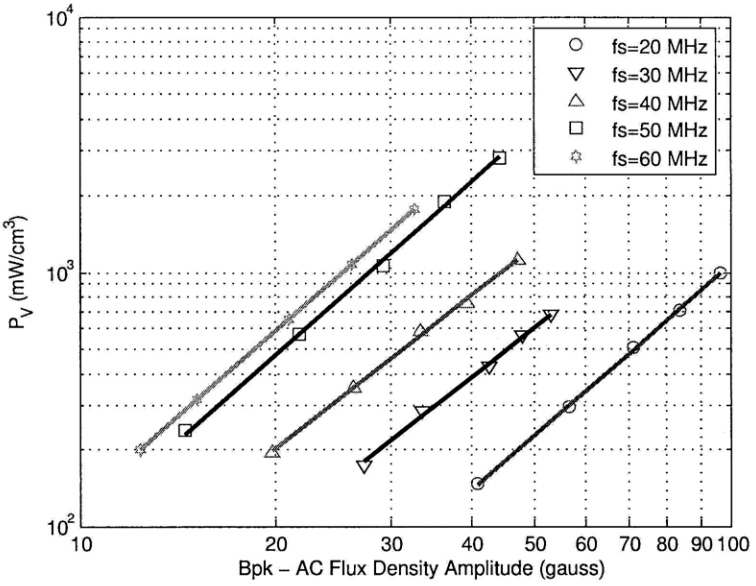

Figure 4.7: N40 material core loss vs ac flux density.

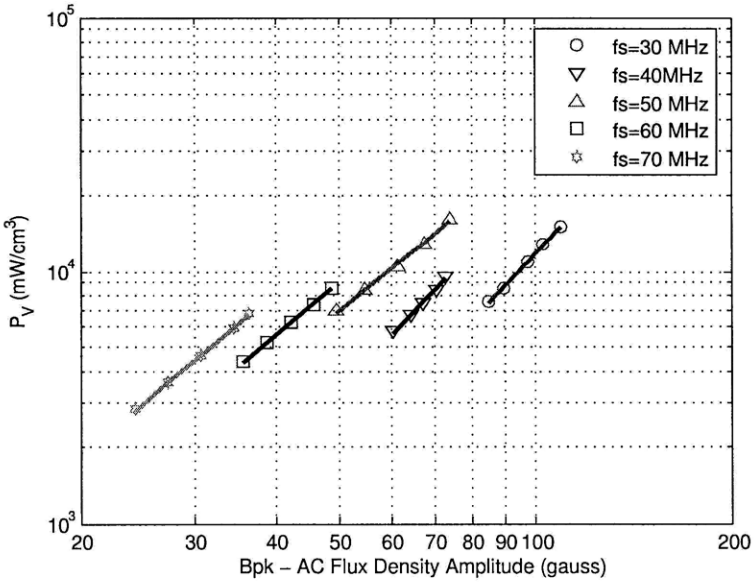

Figure 4.8: -17 material core loss vs ac flux density. Note that because the permeability of this material is low ($\mu_r = 4$), it is difficult to separate core loss from copper loss. Consequently, the core was operated at extremely high loss densities under forced convection cooling in order to facilitate separation of core loss from copper loss. In many practical designs, one might choose to operate at lower loss densities than utilized here.

Table 4.2: Steinmetz parameters for materials

	20 MHz		30 MHz		40 MHz	
Material	K	β	K	β	K	β
M3	8.28×10^{-4}	3.46	6.75×10^{-3}	3.24	1.91×10^{-1}	2.45
P	3.57×10^{-2}	2.29	5.06×10^{-2}	2.33	2.18×10^{-1}	2.18
67	1.42×10^{-1}	2.12	2.10×10^{-1}	2.18	7.40×10^{-1}	2.04
N40	3.64×10^{-2}	2.23	2.27×10^{-1}	2.02	5.18×10^{-1}	2.00
-17	—	—	3.61×10^{-2}	2.76	8.25×10^{-2}	2.72
	50 MHz		60 MHz		70 MHz	
Material	K	β	K	β	K	β
M3	1.03	2.15	1.76	2.11	—	—
P	6.96×10^{1}	2.09	1.34	2.04	—	—
67	1.15	2.05	2.40	1.97	—	—
N40	2.08×10^{-1}	2.58	6.90×10^{-1}	2.25	—	—
-17	1.86	2.10	1.95	2.16	2.35	2.22

The inductor is designed with a commercial magnetic core T502525T from Ceramic Magnetics, which uses magnetic material N40 in Table 4.1. We select this core for two reasons. Firstly, the magnetic-core inductor fabricated with it has an inductance close to that of the original coreless inductor, which is important to maintain the desired resonant condition of the inverter. Secondly, N40 material has a relatively low loss characteristic and the inductor built with it thus has a high quality factor as desired in this application. This toroidal core has dimensions of OD= 12.7 mm, ID= 6.3 mm, Ht= 6.3 mm and V= 0.60 cm^3. We begin

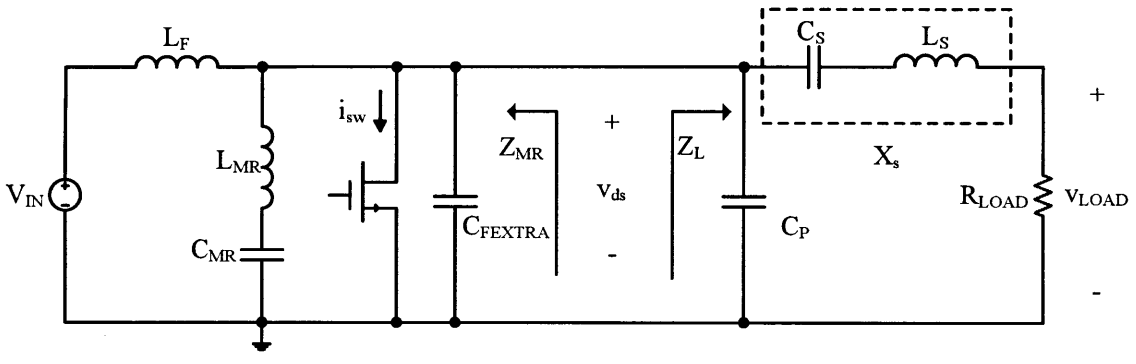

Figure 4.9: Class Φ2 inverter. L_S is a resonant inductor.

the design by calculating the number of inductor turns:

$$N = \left[\sqrt{\frac{2\pi L}{h\mu_r\mu_0 \ln\left(\frac{d_o}{d_i}\right)}} \right] \tag{4.16}$$

Notice N should be the nearest integer in Eq. 4.16. Then we get the estimated inductance of the magnetic-core inductor with N turns:

$$L = \frac{N^2 h\mu_r\mu_0}{2\pi} \ln\left(\frac{d_o}{d_i}\right) \tag{4.17}$$

The original coreless inductor has an inductance of 193 nH. From Eq. 4.16 and 4.17, we calculate $N = 4$ and $L = 199$ nH. The core loss of the magnetic-core inductor can be estimated by Steinmetz equation. The flux density amplitude in the toroidal core is:

$$B_{pk} = \frac{2\mu_r\mu_0 N I_{L-pk}}{\pi(d_o + d_i)} \tag{4.18}$$

The inductor current amplitude I_{L-pk} is 2.4 A at the fundamental frequency of 30 MHz, so $B_{pk} = 61$ G. Table 4.2 shows the Steinmetz parameters $K = 0.227$ and $\beta = 2.02$ for N40 material at 30 MHZ. The power loss density is thus $P_V = KV_{pk}^{\beta} = 917$ mW/cm^3. The resistance component modeling core loss is:

$$R_{core} = \frac{2P_V V_L}{I_{L-pk}^2} \tag{4.19}$$

The core is wound with 4 mil thick copper having width $w_{cu} = 0.20$ cm and length $l_{cu} = 8.8$ cm. If the thickness of the foil is much larger than the skin depth (Eq. 4.10), the copper resistance can be simply approximated from the foil width, length and skin depth:

$$R_{cu} \approx \frac{\rho_{cu} l_{cu}}{\delta_{cu} w_{cu}} \tag{4.20}$$

By (4.19) and (4.20), $R_{core} = 0.19\ \Omega$ and $R_{cu} = 0.06\ \Omega$. Though the estimation of R_{cu} may have significant error, the total error of Q_L calculation is still small because $R_{core} \gg R_{cu}$. Calculated from (4.2), the quality factor is 150, which is high enough to maintain good inverter efficiency.

To verify our design, Fig. 4.10 shows a curve of measured Q_L vs. current drive level at 30 MHz for a 230 nH inductor wound with 4 turns of foil on the core T502525T. This curve is measured using the technique of Section 4.2. Note that the actual inductor has a measured inductance of 230 nH, which is higher than the originally predicted value of 199 nH. The deviation of the measured inductance from the initially predicted value for the design is due

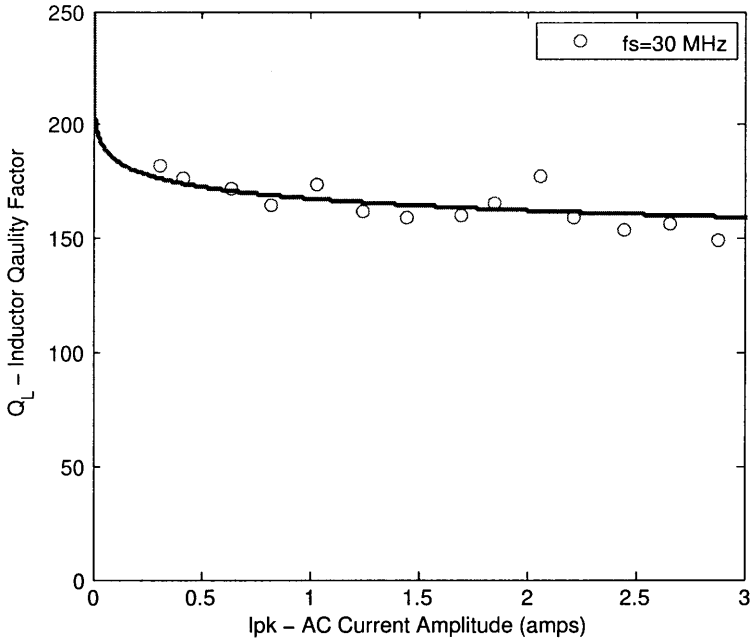

Figure 4.10: The Q_L of fabricated inductor withan N40 toroidal core (OD= 12.7 mm, ID= 6.3 mm, Ht= 6.3 mm) with $N = 4$ turns, and $L = 230$ nH.

to the variation of material permeability with frequency, the stray inductance owing to flux outside the core, including inductance of the single-turn loop around the center hole of the toroid [47], and stray inductance of the measurement leads. Compared to the inductor built with M3 material in Fig. 4.2, Q_L in Fig. 4.10 is very flat for a wide operation range; this can be attributed to the loss parameter β being very close to 2 for N40 material at 30 MHz. At $I_{L-pk} = 2.4$ A, Q_L is about 155 from the curve, which is very close to the value of 150 predicted using Eq. 4.2 and the estimated core loss parameters of Table 4.2. In this design example, the data acquired in Section 4.4 has helped to estimate the loss and quality factor of the magnetic-core inductor accurately.

Fig. 4.11 shows photographs of the Φ2 inverter prototype before and after the replacement with the magnetic-core inductor. Fig. 4.12 shows the experimental waveform of the drain to source voltage V_{ds} and the load voltage V_{LOAD} (proportional to inductor current) of the Φ2 inverter with the coreless and the magnetic-core inductors. The Φ2 inverter operates essentially the same with either inductor, maintaining the desired waveform shape and zero voltage switching (ZVS), which is essential for VHF switching. The load voltage V_{LOAD} of the magnetic-core inductor is a little lower because the magnetic-core inductor has a higher inductance than the original coreless inductor [55].

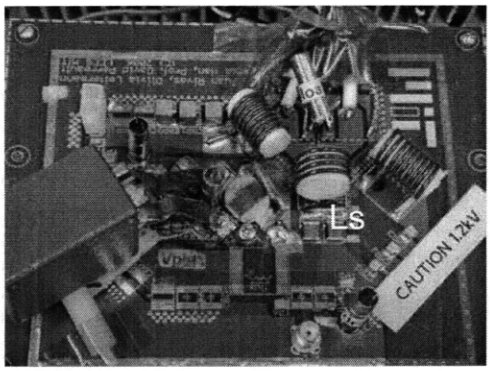

(a) Φ2 inverter with the coreless inductor L_S before the replacement

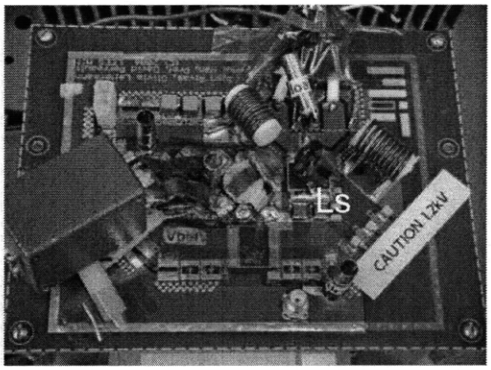

(b) Φ2 inverter with the magnetic-core inductor L_S after the replacement

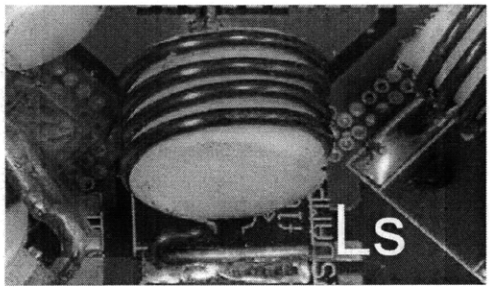

(c) Coreless inductor L_S

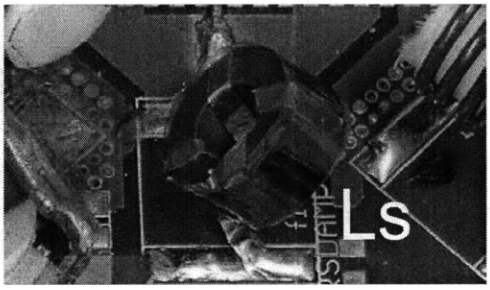

(d) Magnetic-core inductor L_S

Figure 4.11: Photographs of the Φ2 inverter prototype before (a, c) and after (b, d) replacement of the coreless inductor with a magnetic-core inductor.

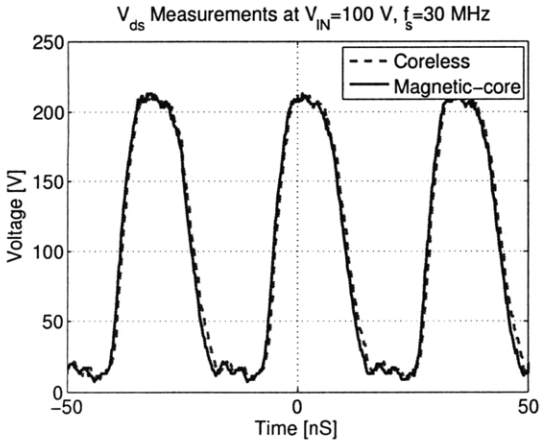

(a) V_{ds}

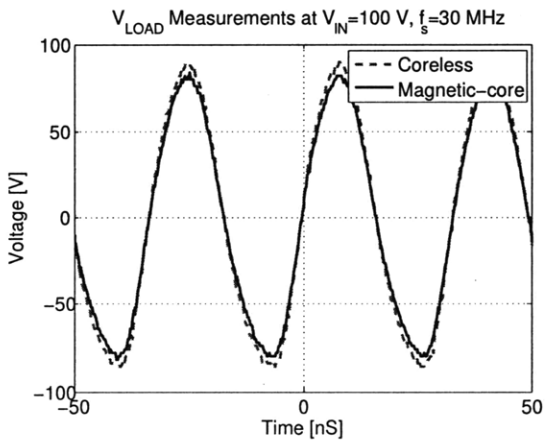

(b) V_{LOAD}

Figure 4.12: Drain to source voltage V_{ds} and inverter load voltage V_{LOAD} for the Φ2 inverter with coreless and magnetic-core inductors L_S.

Table 4.3: Comparison between the coreless inductor and magnetic-core inductor

	Coreless Inductor [55]	Magnetic-core Inductor
Type	Solenoid coreless	Toroidal magnetic core
Design Parameters	4 turns AWG 16 wire on a 5/8 in. diam. Teflon former with 12 turns/in. threads	4 turns copper foil wound on the core T502525T. The core material is N40 from Ceramic Magnetics in Table 4.1. The foil winding has width w_{cu} = 0.079 in and thickness t_{cu} = 4 mil.
Measured Inductance	193 nH	230 nH
Measured Q_L	190	150
Dimensions	Diameter d = 1.60 cm and length l = 0.90 cm	OD= 1.27 cm ID= 0.63 cm and Ht= 0.63 cm
Physical Volume	1.81 cm^3	0.602 cm^3
Energy Density of Physical Volume	0.302×10^{-6} J/cm^3	1.15×10^{-6} J/cm^3
Field Storage Volume	20.2 cm^3	0.602 cm^3
Energy Density of Field Storage Volume	2.71×10^{-8} J/cm^3	1.15×10^{-6} J/cm^3

In Table 4.3, the coreless inductor and the magnetic-core inductor are compared in terms of their parameters and performance. Energy density of the inductors is defined as:

$$E_V = \frac{LI_{L-pk}^2}{2V} \tag{4.21}$$

where V can be the physical volume of the inductor or the storage space of the magnetic field depending on what is of interest. Because most of the flux is kept inside a toroidal core, the storage space of the magnetic field is approximately equal to the physical volume of the inductor in the toroidal magnetic-core design. However, they are unequal for a coreless solenoid inductor. In [73], it is shown that shielding influences the inductance of a solenoidal coil in free space less than 10% if $\frac{d}{d_s} > 0.5$ and $\frac{(l_s - l)}{2} = 0.25 d_s$. d and l are the outside diameter and length of the solenoid, and d_s and l_s are the outside diameter and length of the shield. From this result, we can think of the field storage of a coreless solenoid as approximately limited in a cylindrical space with $d_s = 2d$ and $l_s = 0.5 d_s + l$. Calculated from d and l in Table 4.3, d_s = 32.0 mm, l_s = 25 mm and the volume for magnetic field storage is 20166 mm^3 for the coreless solenoid inductor.

In Table 4.3, the toroidal magnetic-core inductor has a somewhat lower quality factor Q_L than the coreless solenoid (150 vs. 190), but has only one third of the physical volume, and

lower profile. Even accounting for the proportionate scaling of Q_L with linear dimension for the coreless solenoid [3, 74], the magnetic-core inductor provides a substantial volumetric advantage over that achievable with a coreless design in this application. When considering the field energy storage volume of the two designs, the advantage of the magnetic-core design is even more impressive, yielding a factor of 40 higher energy density. Compared to the coreless solenoid, the toroidal magnetic-core inductor keeps most of flux inside, should thus have much better shielding for electromagnetic field, and has reduced EMI/EMC. This illustrates the fact that with suitable magnetic materials, magnetic-core designs are effective in power applications even at several tens of megahertz.

4.6 Conclusion

In this chapter, the loss characteristics of several commercial rf magnetic materials are investigated for power conversion applications at very high frequencies (10 MHz to 100 MHz). An experimental method is proposed that provides a direct measurement of inductor quality factor as a function of current at VHF frequencies, and enables indirect calculation of core loss as a function of flux density. The loss characteristics of several rf magnetic materials are further extracted based on the proposed method, and are tabulated and compared as a function of current at VHF frequencies. Possible sources of error using this method are analyzed, and means to address them are presented. A magnetic-core inductor fabricated using one of evaluated magnetic materials has been applied successfully in a rf resonant power inverter, demonstrating the efficiency of low-permeablity rf materials for power applications in the low VHF range. It is hoped that the presented data and methods will be of value in the design of magnetic components for very high frequency applications.

Chapter 5

Inductor Design Methods with Low-permeability RF Core Materials

---

This chapter presents an inductor design procedure with low-permeability magnetic materials. The design procedure is based on the use of Steinmetz parameters, which have been characterized in Chapter 4. With this procedure, different magnetic materials are compared fairly and fast, and both the quality factor Q_L and the size of a magnetic-core inductor can be predicted before the final design. We compare a magnetic-core inductor design to a coreless inductor design in our design procedure. Some problems, such as optimization of magnetic-core inductors, are also investigated in this chapter. The procedure and methods proposed in this chapter can help to design a magnetic-core inductor with low-permeability rf core materials. The design procedure has been verified by experiments.

5.1 Background

As introduced in Chapters 1 and 4, power electronics operating at very high switching frequency (e.g. $10 - 100$ MHz) are important in many applications including resonant inverters for heating, plasma generation, imaging and communications [1, 11, 18, 21, 38, 55–59], and resonant dc-dc converters [8, 10–13, 15, 38, 41, 60–63]. Magnetic components play an important role in these applications for intermediate energy storage, impedance transformation, and filtering. These magnetic components should have a high quality factor and low loss in order to achieve high efficient power conversion but must also often operate at high flux levels and large flux swings to minimize component size. There is thus a need for magnetic components for operation with high efficiency under large swings above 10 MHz.

For a magnetic-core inductor designed at frequencies lower than 10 MHz, high permeability magnetic material can be used as core and an air gap is usually engaged to prevent the core from saturation [75, 76]. [75, 76] illustrate the design procedure for high-permeability low-frequency inductor with air gap and give the design parameters including core size, number of turns, air gap length and wire size. The winding loss of the magnetic-core inductor can be further reduced by the use of foil conductors and multistrand litz wires [77], optimizing air

gap [78], core dimensional ratio [79], winding shape [80,81] and layer thickness [82], or other techniques such as quasidistributed gap [83]. The high-permeability magnetic materials that are most commonly used in these designs have poor performance at frequencies above a few megahetz [3, 76, 84–88]. There are some low-permeability materials (e.g. permeabilities in the range of $4 - 40$) that can be used effectively at moderate flux swings at frequencies up to many tens of megahertz (e.g. see [84]). However, working with such low-permeability materials - and the ungapped core structures they are typically available in - presents somewhat different constraints and challenges than with typical high permeability designs. Because of very high frequency operation and low-permeability characteristics of materials, the operating flux density is limited by core loss rather than saturation and an air gap is not necessary to prevent the core from saturation in most of applications. As we show in this chapter later, the core loss begins to dominate the total loss and copper loss can be ignored in most of cases. The performance of a very high frequency magnetic-core inductor thus depends on the loss characteristics of low permeability magnetic materials, which have been measured and extracted in Chapter 4. One example in Chapter 4 has been given to design a magnetic-core inductor with low-permeability magnetic material N40. However, there appears to be lacking of a design procedure not only just for a kind of material but also for a selection of low-permeability magnetic materials with different permeability and loss characteristics and all available core sizes. There also appears to be lacking of some considerations for the optimization problems of these magnetic-core inductors under above constraints.

At frequencies over 10 MHz, coreless inductors can be designed and fabricated as in [47]. The copper resistance of a coreless toroidal inductor can be reduced by optimizing the shape of windings [47] and the use of multi-layer winding [89]. As we show in this chapter later, a magnetic-core inductor with low-permeability magnetic material may have a better performance (in terms of size and efficiency) than a coreless inductor. In our design procedure, we also illustrate a method to compare a magnetic-core inductor design to a coreless inductor design.

The scaling of a magnetic-core inductor is a very complex problem involving the winding loss [82, 85, 90–92], core loss and permeability [68, 69, 85–87, 92–94], and heat transfer [87, 88, 95], depending on the core shape, material and size, winding shape, inductor current and operation frequency [3]. The scaling problem is also considered in a variety of work: [3] describes generally the size scaling with frequency for coreless inductors, magnetic-core inductors with high permeability materials, and magnetic-core inductors with low permeability materials. [92] gives a dimensional analysis of an inductor size vs. its quality factor Q_L at a given frequency. [76, 85, 87, 88] investigate how magnetic size scales with frequency. In our design procedure, we study a different scaling problem: given a selection of available cores in different low-permeability materials and the ability to continuously scale

core size, how should we design a magnetic-core or coreless inductor to yield the smallest size for given design specifications? In this chapter, we illustrate this problem with our design constraints.

In this chapter, we propose an inductor design procedure using low-permeability materials. This procedure is based on knowledge of the material loss characteristics, such as collected in [84] for several commercial materials particularly suited for very high frequency inductor design. With methods used in this procedure, different magnetic materials are compared fairly and conveniently, and both the quality factor and the size of a magnetic-core inductor can be evaluated before the final design. Some design questions, such as the size scaling characteristics and the maximum achievable inductor quality factor at a given size are also investigated in this chapter.

Section 5.2 of the chapter introduces the inductor design considerations and questions to be addressed. Section 5.3 illustrates our proposed inductor design procedure and methods employed in it. Optimization of magnetic-core inductors is discussed in Section 5.4. In Section 5.5, we check some important assumptions behind our methods. Section 5.6 shows some experimental results to verify the design procedure in Section 5.3. Section 5.7 concludes the chapter.

5.2 Inductor Design Considerations and Questions

5.2.1 Inductor Design Considerations

In this chapter, we only consider inductor design under a limited set of conditions in order to make the problem tractable. Nevertheless, these conditions are both very reasonable and practical for inductors at very high frequency. The limited conditions we address are as following.

1. Use of ungapped inductors made of low-permeability materials: Materials suited for very high frequency power conversion have relatively low permeability to maintain low loss characteristics. Most commercially available cores made of such materials are ungapped. In ac inductor designs at VHF frequencies, optimal flux densities are so low that saturation is not a consideration, so gapping is not typically required. Compared to an ungapped inductor, a gapped inductor can have reduced core loss, but has a higher copper loss and greater complexity to the fringing effect around the gap. So for reasons of both availability and simplicity, we only consider ungapped designs in this chapter.

2. Single-layer, foil wound designs in the skin depth limit on toroidal core shapes: A toroidal inductor design keeps most of flux inside the core, thus reducing EMI/EMC problems [47]. A foil winding design can reduce current crowding than the ridged surface of a wire-wound toroid [47, 50, 96–98] and reduce the copper loss. Copper foil should be always thicker than its skin depth limit to minimize copper resistance.

3. Design based on knowledge of Steinmetz parameters for materials of interest: Such parameters are often not published or readily available for these materials, but can be obtained using methods such as that of [84] All the examples introduced in this chapter utilize commercial magnetic materials with Steinmetz parameters extracted from measurements in [84].

4. Design assuming sinusoidal excitation at one frequency: In very high frequency resonant inverters/converters, one often think inductors having approximately sinusoidal current at a single frequency. Note that consideration of variable frequency operation, dc currents, and multiple frequency components greatly increases complexity and is not fully understood (e.g. [68, 69])

5.2.2 Inductor Design questions

In this chapter, we answer three important questions about design of very high frequency inductors under the above conditions:

1. Given a selection of available cores in different low-permeability materials and a design requirements (inductance L, current amplitude I_{pk}, and frequency f_s), which magnetic material from an available set will yield maximum quality factor Q_L for a given size?

2. With the magnetic material can yield maximum quality factor Q_L for a given size, how should we design an inductor to meet a given inductance L, quality factor Q_L, current amplitude I_{pk}, switching frequency f_s, and size limitation?

3. Given the ability to continuously scale core size, what design will yield the smallest size for a given L, Q_L, I_{pk} and f_s?

In the next section, we answer these questions based on the above constraints and considerations.

5.3 Inductor Design Procedure and Methods

In this section, we propose a procedure to design an inductor with commercial magnetic cores, given specifications of L, Q_L, I_{pk}, f_s, and a size limitation. We evaluate and compare different magnetic materials and decide which one is the best for possible designs simply based on Steinmetz parameters of each materials. We also answer the questions in Section 5.2, including how to design a given size inductor with the maximum quality Q_L, and how to design a given Q_L inductor with the minimum size. In the following subsections, we firstly illustrate the general inductor design procedure in Section 5.3.1, and then describe elements of the method in detail in Sections 5.3.2 to 5.3.5. In Section 5.3.6, we show how the inductor quality factor Q_L scales as the function of the inductor size.

5.3.1 Inductor Design Procedure

Fig. 5.1 illustrates the proposed design procedure for a magnetic-core inductor with low permeability magnetic materials. Firstly, we decide some basic parameters from power electronics design requirements including L, I_{pk} and f_s, and limitations for maximum size and minimum quality factor Q_L. Secondly, we select the best magnetic material for the design from given magnetic materials based on their permeability and Steinmetz parameters. Thirdly, given the maximum size, we estimate the possible quality factor Q_L of the inductor designed using the best available material. Fourthly, given the minimum Q_L, we estimate the inductor's minimum size. Fifthly, we check the results in the third and fourth steps and see if they satisfy the design requirements. If they do, the inductor design is completed with the selected magnetic material. If they don't, it means the design requirements can't be satisfied even with the best available magnetic material. In that case, one must go back to the first step and revise inductor design requirements.

A key feature of this design procedure is that magnetic materials are compared first and the best material is selected before completing any design, greatly reducing design effort. Some important information such as the maximum quality factor Q_L, and the smallest possible size for a given Q_L can also be acquired before the final design. With this procedure, we may work just with only one size inductor with only one kind of low permeability material instead of thousands of combinations, saving design time and effort. In conclusion, this procedure can reveal the tradeoffs among loss characteristics of several commercial magnetic materials, offer an easy and fast way to compare different commercial magnetic materials and quickly select one among them, estimate the achievable quality factor and size of inductor, and finally design a qualified inductor with the best choice of magnetic material.

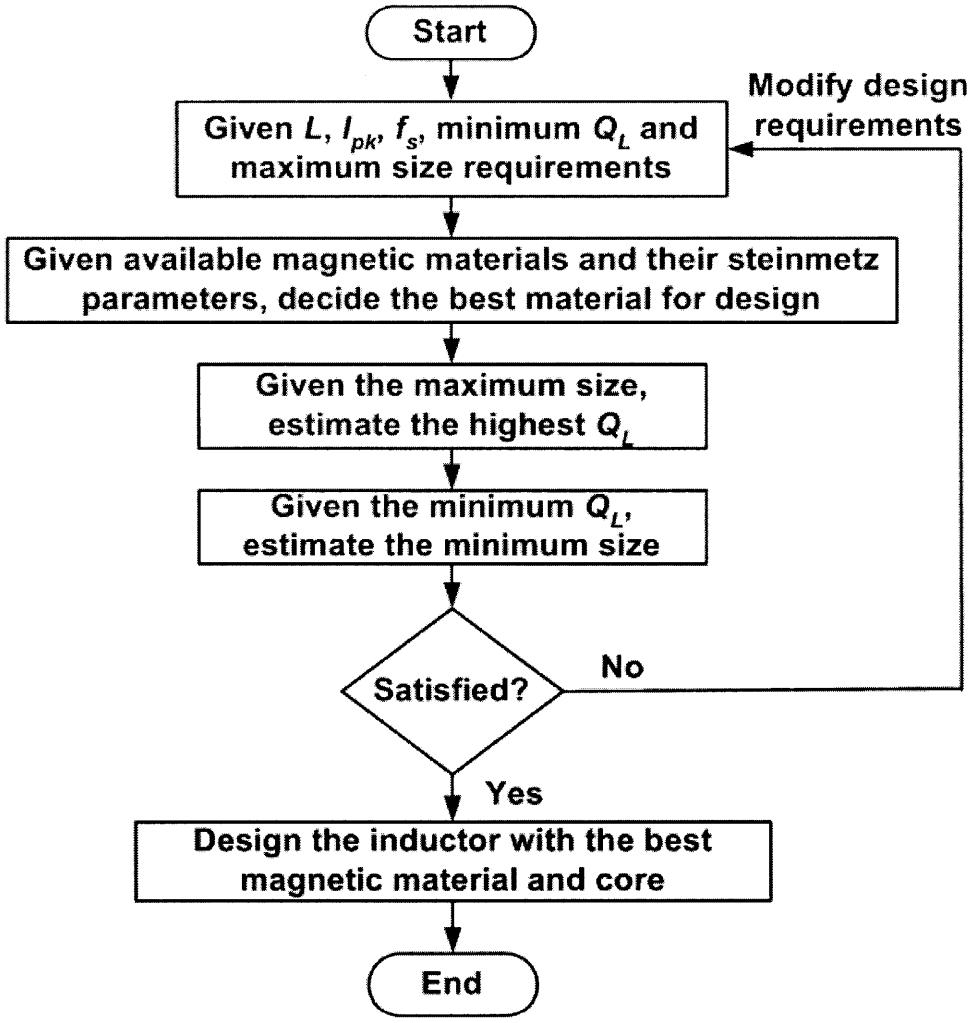

Figure 5.1: Inductor design procedure

5.3.2 Method to Select Among Magnetic Materials

In this subsection, we explain the second step in our inductor design procedure. Given available magnetic materials and their Steinmetz parameters, we would like to compare them and select the best material for design with the limits described in Section 5.3.1. Before introducing our method, we list several critical equations as part of background for very high frequency inductor designs, which we will use frequently.

Losses in magnetics include both dc losses (conductor loss) and ac losses (conductor and core losses). Because most conductors in use are copper, conductor losses are also referred as copper losses in this chapter. In very high frequency power conversion, ac losses usually dominate. The ac losses of an inductor at a single frequency can be evaluated by its quality

factor Q_L, where higher Q_L corresponds to smaller loss. The inductor quality factor Q_L can be calculated as:

$$Q_L = \frac{\omega L}{R_{ac}} \tag{5.1}$$

R_{ac} represents the equivalent total ac resistance of a magnetic-core inductor, which includes both conductor losses and core losses:

$$R_{ac} = R_{cu} + R_{co} \tag{5.2}$$

In Eq. 5.2, R_{cu} represents the equivalent resistance owing to copper loss (conductor loss) and R_{co} represents an equivalent resistance to model core loss of a magnetic-core inductor. For a coreless inductor, there is no core loss and R_{co} is zero.

The Steinmetz equation an empirical means to estimate loss characteristics of magnetic materials [99, 100]. It is empirical in nature, and only estimates losses for sinusoidal drive conditions at a single frequency, though extensions and widely used to try and capture both frequency effects [100–102] and non-sinusoidal waveforms [68,69,86,103,104]. Here we consider the formulation for sinusoidal drive at a single frequency as shown in Eq. 5.3.

$$P_V = K B_{pk}^{\beta} \tag{5.3}$$

B_{pk} is the peak amplitude of (sinusoidal) flux density inside the material and P_V is power loss per unit core volume. K and β are called Steinmetz parameters. In [84], K and β have been calculated and listed in tables for each of several commercial low-permeability rf magnetic materials.

To make a comparison among different design options (including magnetic materials) for a given L, I_{pk}, f_s and maximum size limitation, we begin with a coreless inductor. If we ignore the inductance of a single-turn loop around the center hole of the toroid which is usually small compared to the total inductance, the number of turns of a coreless inductor N_{air} can be calculated from Eq. 5.4 [47]:

$$N_{air} \approx \sqrt{\frac{2\pi L}{h\mu_0 \ln\left(\frac{d_o}{d_i}\right)}} \tag{5.4}$$

d_o, d_i and h are outside diameter, inside diameter and height of the coreless inductor. Averaged flux density B_{pk-air} of the coreless inductor can be calculated by Eq. 5.5:

$$B_{pk-air} = \frac{\mu_0 N_{air} I_{pk}}{0.5\pi(d_i + d_o)} \tag{5.5}$$

Similarly, number of turns N and averaged flux density B_{pk} of a magnetic-core inductor are calculated by Eq. 5.6 and 5.7:

$$N \approx \sqrt{\frac{2\pi L}{h\mu_0\mu_r \ln\left(\frac{d_o}{d_i}\right)}} \tag{5.6}$$

$$B_{pk} = \frac{\mu_0\mu_r N I_{pk}}{0.5\pi(d_i + d_o)} = \mu_r^{0.5} B_{pk-air} \tag{5.7}$$

For a given L and specified dimension in Eq. 5.7, averaged flux density B_{pk} may be different for each magnetic material, which is one the reasons we can't compare their loss characteristics for different magnetic materials at the same flux density B_{pk}. However, B_{pk} of each magnetic material can be related to the coreless inductor flux density B_{pk-air} by its relative permeability μ_r in Eq. 5.7. For a given design specification, all magnetic materials will have the same *normalized flux density*, which is equal to $\mu_r^{-0.5}B_{pk}$. Given a set of Steinmetz parameters, we can draw the curves of P_V vs. *normalized flux density* $\mu_r^{-0.5}B_{pk}$ for all available magnetic materials. We then compare P_V of these materials at the *normalized flux density* $\mu_r^{-0.5}B_{pk} = B_{pk-air}$ and decide which material has the smallest core loss for the specified design.

An example is given in Fig. 5.2, in which design of a magnetic-core inductor at the frequency $f_s = 30$ MHz with inductance $L = 200$ nH and size $d_o = 12.7$ mm, $d_i = 6.3$ mm and $h = 6.3$ mm is considered. Beginning with a coreless inductor, calculate $B_{pk-air} = 13$ G from Eq. 5.4 and 5.5. Using data from [84], loss curves of P_V vs. $\mu_r^{0.5}B_{pk}$ are plotted for the materials N40, P, M3 and 67 [1]. Comparing their P_V at B_{pk-air} for this design, we find that N40 material has the smallest core loss. If the core loss dominates the total loss in Eq. 5.2, the inductor built using N40 magnetic material will achieve the highest Q_L for the specified size and specifications. From Fig. 5.2, we can observe that N40 is better than other magnetic materials and 67 is worse than the others over a wide flux density range. This will help us to design a magnetic-core inductor if its current operating level is unknown or very wide. But we can't simple conclude N40 is always the best material and 67 is the worst material for all possible designs because the Steinmetz parameters vary with the frequency and other materials may have better performance for a different frequency or flux density levels.

[1] -17 material in Tab. 4.1 and 4.2 has a very low relative permeability and low core loss characteristics. Different with other material, the copper loss of -17 material is significant compared to its core loss and can't be ignored in most of cases. The inductor built with -17 material thus has a loss characteristics similar to a hybrid of coreless and magnetic-core inductors. As a special case, -17 is not considered in the design description. However, the design method introduced in this chapter can still be used for -17 material with special considerations of its copper loss.

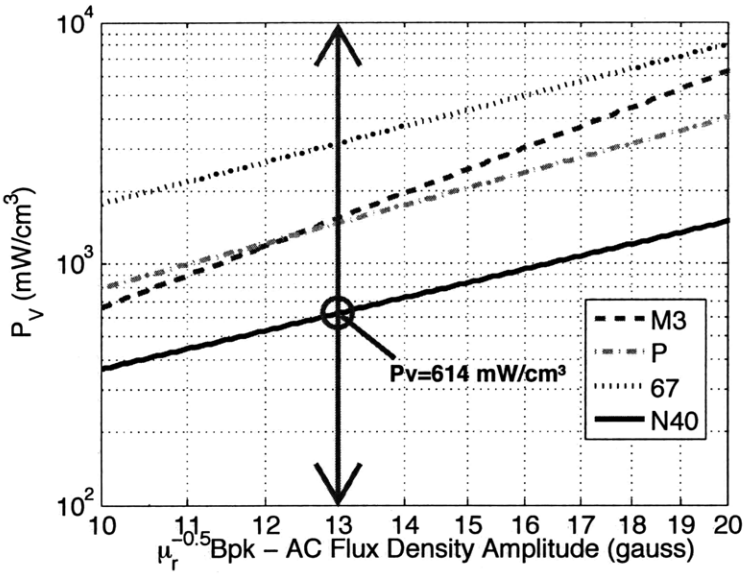

Figure 5.2: Inductor design example (OD= 12.7 mm, ID= 6.3 mm, Ht= 6.3 mm, L = 200 nH, $I_{pk} = 2$ A, $f_s = 30$ MHz and $B_{pk-air} = 13$ G).

Although we know which material may be the best for a magnetic-core inductor design, we don't know if the magnetic-core inductor with the best material is better or worse than a coreless inductor of the same size. There is no core loss for a coreless inductor and thus there is no Steinmetz parameter for it. But we can still mark the copper loss of the coreless inductor on the graph an compare it with core losses of other magnetic materials. To accommodate the coreless design, we define P_{V-air} at B_{pk-air} as the power loss per unit volume for a corless inductor and calculate it by Eq. 5.8:

$$P_{V-air} = \frac{R_{cu-air}}{2V} I_{pk}^2 \tag{5.8}$$

R_{cu-air} is the copper resistance of a coreless inductor. We need to know R_{cu-air} to solve Eq. 5.8. The copper resistance of a magnetic-core inductor R_{cu} (or the copper resistance of a coreless inductor R_{cu-air}) depends heavily on a coreless or magnetic-core inductor winding design pattern and can be estimated by the following methods:

1. In [84], the windings are made of an equal-width foil like conductor, and $R_{cu-single-turn}$ is the ac copper resistance of a single turn inductor:

$$R_{cu} = N^2 R_{cu-single-turn} \approx N^2 \frac{\rho_{cu}}{\pi \delta_{cu}} \left(\frac{2h}{d_i} + \frac{d_o}{d_i} - 1 \right) \tag{5.9}$$

2. In [84], R_{cu} can also be estimated from the foil width, length and skin depth:

$$R_{cu} \approx \frac{\rho_{cu} l_{cu}}{\delta_{cu} w_{cu}} \tag{5.10}$$

3. In [84], to get a more accurate estimation of R_{cu}, a coreless inductor with equal turns is fabricated and its R_{cu} is measured by an impedance analyzer.

4. In [84], R_{cu} can also be estimated by simulation software.

5. In [47], the windings are made of foil-like conductor conforming to the shape the toroid:

$$R_{cu} = N^2 R_{cu-single-turn} \approx N^2 \frac{\rho_{cu}}{\pi \delta_{cu}} \left(\frac{h}{d_i} + \frac{h}{d_o} + 2 \ln \frac{d_o}{d_i} \right) \tag{5.11}$$

All the methods above to estimate the copper loss have considerable error. For example, the fourth method may have up to 30% error in estimation of the copper resistance of a magnetic-core inductor [84]. However, for a magnetic-core inductor at very high frequencies, the core loss usually dominates and R_{co} is much larger than R_{cu}, so the error of the estimation of R_{cu} doesn't significantly influence the final design results such as Q_L of the magnetic-core inductor, but this error will influence the comparison between a magnetic-core inductor and a coreless inductor.

For example, the loss characteristics of a coreless inductor estimated by Eq. 5.9 is included in Fig. 5.3 . We can see N40 is the only magnetic material which has lower loss than the coreless inductor. Thus the magnetic-core inductor built with N40 may have a higher quality factor Q_L than the coreless inductor. The magnetic-core inductor built by other materials (e.g. M3, P and 67) will not be better than the coreless inductor and not be considered in the following steps. Here, we can see our method has help us exclude most of available magnetic materials in the pool from the design, saving time and effort.

From previous measurements in [84], the core loss (R_{co}) usually dominates the total loss of a magnetic-core inductor. However, this statement should be checked to make sure that it is still correct for an individual design. By a similar method, we can define the copper loss per unit volume P_{V-cu} of a magnetic-core inductor and mark it on the graph of P_V vs. $\mu_r^{0.5} B_{pk}$. From Eq. 5.4 and 5.6,

$$N = \mu_r^{-0.5} N_{air} \tag{5.12}$$

$$R_{cu} = N^2 R_{cu-single-turn} = \mu_r^{-1} N_{air}^2 R_{cu-single-turn} = \mu_r^{-1} R_{cu-air} \tag{5.13}$$

$$P_{V-cu} = \frac{R_{cu}}{2V} I_{pk}^2 = \frac{\mu_r^{-1} R_{cu-air}}{2V} I_{pk}^2 = \mu_r^{-1} P_{V-air} \tag{5.14}$$

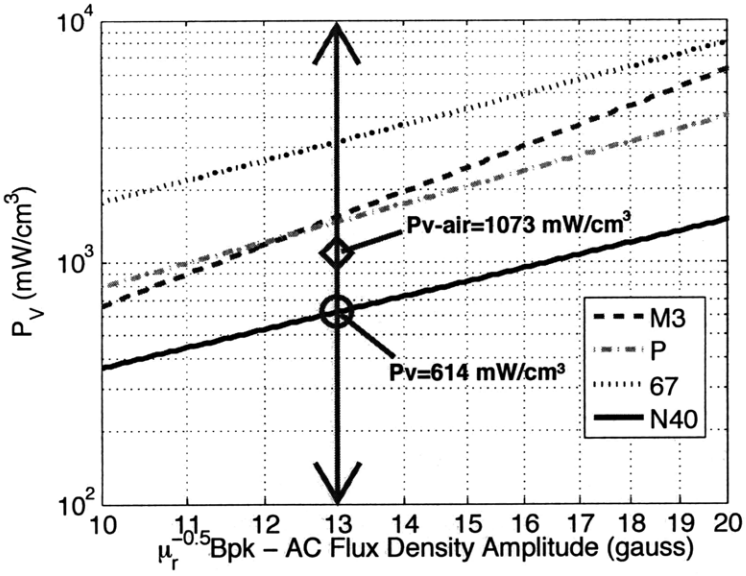

Figure 5.3: Inductor design example including the power loss characteristic of a coreless inductor (OD= 12.7 mm, ID= 6.3 mm, Ht= 6.3 mm, $L = 200$ nH, $I_{pk} = 2$ A, $f_s = 30$ MHz and $B_{pk-air} = 13$ G).

P_{V-air} can be calculated from Eq. 5.8. The copper loss characteristic of a magnetic-core inductor for the example specifications built in N40 magnetic material is marked in Fig. 5.4. We can see in this example that the copper loss of the magnetic-core inductor is much smaller than its core loss (an order of magnitude or more).

5.3.3 Q_L Estimation with Given Maximum Inductor Size

In this subsection, we illustrate the third step in the inductor design procedure: given the maximum size, estimate the highest Q_L of the magnetic-core inductor with the best material selected in the second step. If we ignore the copper loss comparing to the core loss of the magnetic-core inductor, the quality factor Q_L can be estimated by Eq. 5.15 and 5.16:

$$R_{co} \approx \frac{Total\ Core\ Loss}{0.5I_{pk}^2} = \frac{P_V V}{0.5I_{pk}^2} \tag{5.15}$$

$$Q_L \approx \frac{\omega L}{R_{co}} = \omega L \frac{0.5I_{pk}^2}{P_V V} \tag{5.16}$$

E.g., for the magnetic-core inductor build in N40, $P_V = 700$ mW/cm^3 at $B_{pk-air} = 13$ G, and $Q_L \approx 198$ by Eq. 5.16. In this example $R_{co} \approx 0.19$ and $R_{cu} \approx 0.03$, where $R_{co} \gg R_{cu}$,

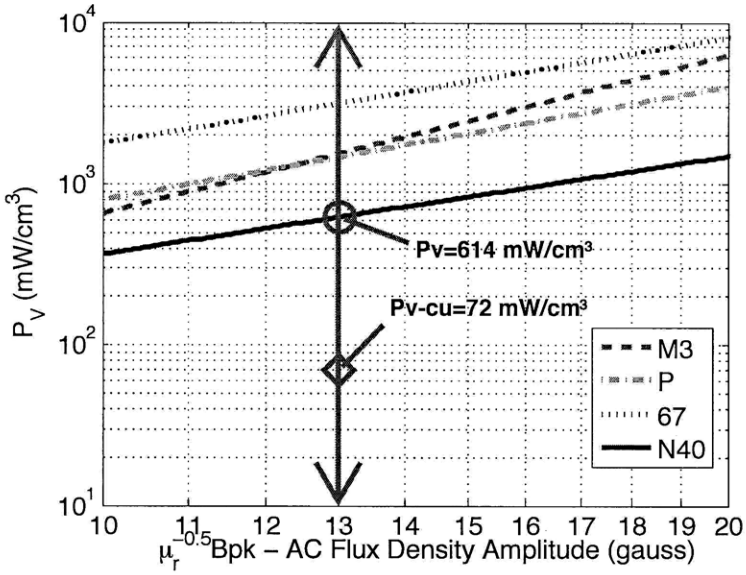

Figure 5.4: Inductor design example including the copper loss characteristic of a magnetic-core inductor (OD= 12.7 mm, ID= 6.3 mm, Ht= 6.3 mm, L = 200 nH, I_{pk} = 2 A, f_s = 30 MHz and B_{pk-air} = 13 G).

where $R_{co} \gg R_{cu}$. Q_L can also be estimated by Eq. 5.2, in which copper loss is included. In the example, $Q_L \approx 171$ by Eq. 5.2 [2].

5.3.4 Size Estimation with Given Minimum Q_L

In this subsection, we illustrate the third step in our inductor design procedure. Given the minimum requirement for quality factor Q_L, we estimate the minimum size achievable given available magnetic materials and their Steinmetz parameters. Because the method introduced in this subsection is not as simple and direct as the method in Section 5.3.2, we begin this subsection with a general description of the method. Then we derivative equations needed in our method for inductor size estimation. As we have done in Section 5.3.2, design examples are given to help understand the method step by step.

We again begin with a coreless inductor design, calculate its size and compare the size of a magnetic-core inductor with it. In our method, we define the scaling factor λ as the dimension ratio of a magnetic-core inductor and the coreless inductor for given L, Q_L, f_s and I_{pk}, and we assume that the relative ratio of the 3 dimensions is kept constant during

[2]The estimation of Q_L here is higher than that in Section 4.5 because of different estimation methods of copper loss.

the scaling. Thus, we scale each dimension (x, y, z), describing the shape of the coreless inductor by a factor λ to get the correspondent dimension of a magnetic-core inductor: The coreless inductor thus has $\lambda = 1$, and the magnetic-core inductor with the minimum λ has the smallest size.

Our method has four main steps:

1. Given L, I_{pk}, f_s and minimum required Q_L, design a coreless inductor and get its dimension parameters d_o, d_i, h.
2. Calculate B_{pk-air} of the coreless inductor, compare its P_{V-air} to P_V of other magnetic materials at B_{pk-air} on the graph of P_V vs. $\mu_r^{-0.5}B_{pk}$ and decide the possible best materials for the inductor design.
3. Calculate the scaling factor λ for the possible best materials.
4. Check the flux density B'_{pk}, core loss $P_{V'}$, and copper loss $P_{V'-cu}$ of the magnetic-core inductor after scaling on the graph of P_V vs. $\mu_r^{-0.5}B_{pk}$.

5.3.4.1 Step I: Calculate Coreless Design

From Eq. 5.4, the inductance L of a coreless inductor can be calculated by the following equation:

$$L = \frac{N_{air}^2 h \mu_0}{2\pi} \ln\left(\frac{d_o}{d_i}\right) \tag{5.17}$$

The equivalent copper resistance of the coreless inductor can be calculated by the following equation:

$$R_{cu-air} = N_{air}^2 R_{cu-single-turn} \tag{5.18}$$

From Eq. 5.17 and 5.18, the quality factor Q_L of a coreless inductor can be calculated by the following equation:

$$Q_L = \frac{\omega L}{R_{cu-air}} = \frac{\mu_0 f_s}{R_{cu-single-turn}} h \ln\left(\frac{d_o}{d_i}\right) \tag{5.19}$$

The single turn copper resistance $R_{cu-single-turn}$ can be estimated by Eq. 5.9 or 5.11.

If we assume $d_i = 0.5d_o$, we can solve the dimension parameters d_o, d_i, h of a coreless inductor from Eq. 5.9 or 5.11, and 5.19 for given f_s and Q_L. In Section 5.4, we show that this assumption is very reasonable because letting $d_i = 0.5d_o$ yields inductor with nearly optimum Q_L and thus the smallest size.

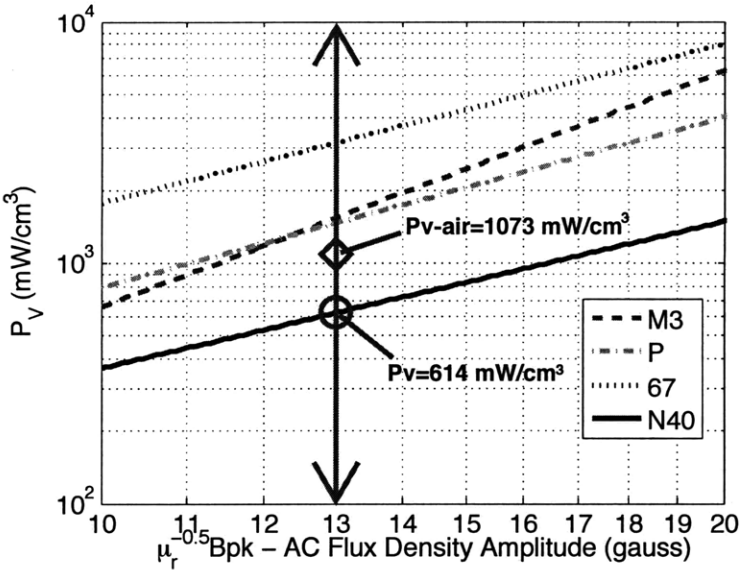

Figure 5.5: Loss plots of inductor design scaling example (OD= 12.7 mm, ID= 6.3 mm, Ht= 6.3 mm, $L = 200$ nH, $I_{pk} = 2$ A, $f_s = 30$ MHz and $B_{pk-air} = 13$ G).

5.3.4.2 Step II: Evaluate Magnetic Materials

After calculating the dimensions of the coreless inductor, its B_{pk-air} and P_{V-air} can be calculated by Eq. 5.5 and 5.8. P_V at B_{pk-air} of all the magnetic materials can be found from the graph of P_V vs. $\mu_r^{-0.5}B_{pk}$. We will prove later that in order to get the scaling factor $\lambda < 1$, the total loss of a magnetic-core inductor should be smaller than the coreless inductor with the same size, thus P_V of the magnetic materials should be smaller than P_{V-air}.

For example, we consider the design of a coreless inductor with $L = 200$ nH, $I_{pk} = 2$ A, $f_s = 30$ MHz, and $Q_L = 116$. We define this coreless inductor as having $\lambda = 1$. Its dimensions are $d_o = 12.7$ mm, $d_i = 6.3$ mm and $h = 6.3$ mm. The question we seek to answer is if we build a magnetic-core inductor with magnetic materials, how small it could be while achieving specified Q_L. We firstly calculate $B_{pk-air} = 13$ G and $P_{V-air} = 1073$ mW/cm^3 and then find P_V for each magnetic material in Fig. 5.6. N40 is the only magnetic material which has P_V smaller than P_{V-air}, thus the magnetic-core inductor made in N40 is the only possible design with the size smaller than the coreless inductor ($\lambda < 1$). Magnetic-core inductors made by other materials will have larger sizes than the coreless inductor and are not considered here. This conclusion is further proved in Eq. 5.28. Just as in Section 5.3.2, we can see here our method in this subsection again helps us to exclude many available magnetic materials in the pool from the complicated problem of inductor size scaling.

5.3.4.3 Step III: Scaling

Here we introduce how to perform the scaling. Before beginning of derivations, we define the following parameters:

1. V, d_o, d_i, h, N, B_{pk}, P_V, P_{V-cu}, R_{co} and R_{cu} are the volume, outside diameter, inside diameter, height, number of turns, peak ac flux density, core loss density, copper loss density, equivalent core resistance, and copper resistance of a magnetic-core inductor before scaling - i.e., having the same size as the coreless inductor ($\lambda = 1$).

2. V', d'_o, d'_i, h', N', B'_{pk}, P'_V, $P_{V'-cu}$, R'_{co} and R'_{cu} are the volume, outside diameter, inside diameter, height, turns number, flux density, core loss density, copper loss density, equivalent core resistance, and copper resistance of the magnetic-core inductor after scaling.

3. V, d_o, d_i, h, N_{air}, B_{pk-air}, P_{V-air} and R_{cu-air} are the volume, outside diameter, inside diameter, height, number of turns, flux density, copper loss density, and copper resistance of the coreless inductor before scaling ($\lambda = 1$)

From the definition above,

$$\lambda = \frac{d'_o}{d_o} = \frac{d'_i}{d_i} = \frac{h'}{h} \tag{5.20}$$

$$V' = \lambda^3 V \tag{5.21}$$

Thus: similar to Eq. 5.6,

$$N' = \sqrt{\frac{2\pi L}{\lambda h \mu_0 \mu_r \ln\left(\frac{\lambda d_o}{\lambda d_i}\right)}} = \lambda^{-0.5} \sqrt{\frac{2\pi L}{h \mu_0 \mu_r \ln\left(\frac{d_o}{d_i}\right)}} = \lambda^{-0.5} N \tag{5.22}$$

Similar to Eq. 5.7 and from Eq. 5.22,

$$B'_{pk} = \frac{\mu_0 \mu_r N' I_{pk}}{0.5\pi(d'_i + d'_o)} = \frac{\mu_0 \mu_r \lambda^{-0.5} N I_{pk}}{0.5\pi(\lambda d_i + \lambda d_o)} = \lambda^{-1.5} B_{pk} \tag{5.23}$$

$$P_{V'} = K B'^{\beta}_{pk} = \lambda^{-1.5\beta} K B^{\beta}_{pk} = \lambda^{-1.5\beta} P_V \tag{5.24}$$

From Eq. 5.9 and 5.11, we observe that $R_{cu-single-turn}$ is constant during scaling. This is because the effective conductor thickness is the skin depth (invariant to scaling). This results in constant "ohms per square", making the total single-turn resistance invariant to

scaling. From Eq. 5.12 and 5.22,

$$\begin{aligned} R'_{cu} &= N'^2 R_{cu-single-turn} = \lambda^{-1} N^2 R_{cu-single-turn} \\ &= \lambda^{-1}\mu_r^{-1} N_{air}^2 R_{cu-single-turn} = \lambda^{-1}\mu_r^{-1} R_{cu-air} \end{aligned} \tag{5.25}$$

Similar to Eq. 5.14, and from Eq. 5.21 and 5.25:

$$P_{V'-cu} = \frac{R'_{cu}}{2V'} I_{pk}^2 = \lambda^{-4}\mu_r^{-1} \frac{R_{cu-air}}{2V} I_{pk}^2 = \lambda^{-4}\mu_r^{-1} P_{V-air} \tag{5.26}$$

For constant Q_L, the total loss is the same for both the coreless inductor and the magnetic-core inductor, thus from Eq. 5.21, 5.24 and 5.26:

$$P_{V'}V' + P_{V'-cu}V' = \lambda^{3-1.5\beta} P_V V_{air} + \lambda^{-1}\mu_r^{-1} P_{V-air} V_{air} = P_{V-air} V \tag{5.27}$$

$$\lambda^{3-1.5\beta} \frac{P_V}{P_{V-air}} + \lambda^{-1}\mu_r^{-1} = 1 \tag{5.28}$$

The scaling factor λ can be calculated by Eq. 5.28, if we know P_V, relative permeability μ_r, and Steinmetz parameter β of the magnetic material, and P_{V-air} of the coreless inductor. Because of the usual case Steinmetz parameter, P_V should be larger than P_{V-air} to get $\lambda < 1$ from Eq. 5.28. This explains why we dont have to consider magnetic materials which have P_V larger than P_{V-air}. Eq. 5.28 is the key equation for calculating achievable design scaling at constant Q_L through the use of an ungapped magnetic core.

Let's continue our example shown in Fig. 5.6. For N40 material, $P_V = 614$ mw/cm^3 at $B_{pk-air} = 13$ G. $\beta = 2.02$ at 30 MHz and $\mu_r = 15$. As calculated in Eq. 5.28, the scaling factor $\lambda = 0.17$.

5.3.4.4 Step IV: Check Design Assumptions

As a last step, we check the flux density B'_{pk}, core loss P'_V, and copper loss $P_{V'-cu}$ of the inductor after scaling on the graph of P_V vs. $\mu_r^{-0.5} B_{pk}$ by Eq. 5.24, 5.26 and 5.29. From Eq. 5.7 and 5.23:

$$\frac{B'_{pk}}{\sqrt{\mu_r}} = \lambda^{-1.5} B_{pk-air} \tag{5.29}$$

In the example, $P'_V = 1.3 \times 10^5$ mW/cm^3 and $P'_{V-cu} = 8.6 \times 10^4$ mW/cm^3 are shown in Fig. 5.6. We can still see that the core loss dominates the total loss. With completion of this last step, we now have an inductor geometry and scaling that achieves the smallest size at the required Q_L.

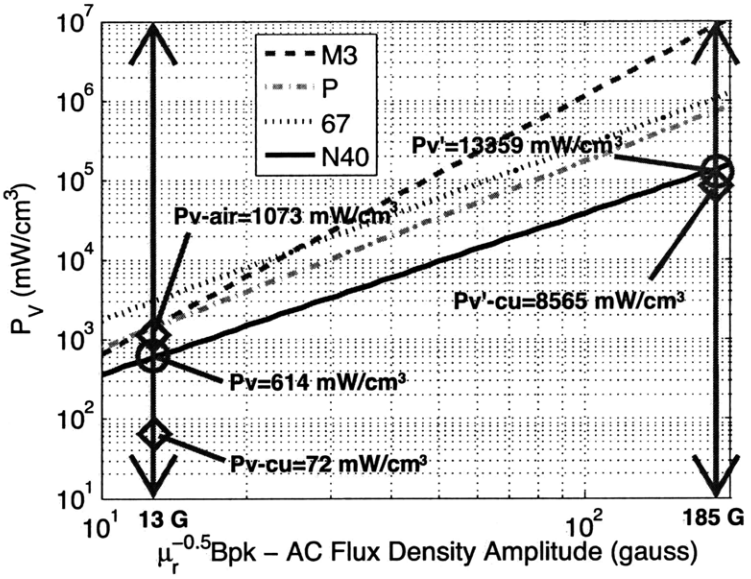

Figure 5.6: The magnetic-core inductor after scaling design

5.3.4.5 Inductor Scaling with Multi-choice of Magnetic Materials

This subsection serves as a supplement of Section 5.3.4.2 and gives an example of solution if there are more than one possible best material which can build a core inductor has smaller size than the coreless inductor and thus $\lambda < 1$.

For example, we consider the design of a coreless inductor with $L = 200$ nH, $I_{pk} = 0.5$ A, $f_s = 30$ MHz, and $Q_L = 116$. We design a coreless inductor as in Section 5.3.4.2 which has $\lambda = 1$ and dimensions of $d_o = 12.7$ mm, $d_i = 6.3$ mm and $h = 6.3$ mm. We firstly calculate $B_{pk-air} = 3.2$ G and $P_{V-air} = 67$ mW/cm^3 and then find P_V for each magnetic material in Fig. 5.7. P, M3 and N40 are magnetic materials which has P_V smaller than P_{V-air}, thus the magnetic-core inductor made in all these three materials are all the possible design with the size smaller than the coreless inductor ($\lambda < 1$). P material has a larger core loss P_V at B_{pk-air} as well as a larger slope ($= \beta$) of the loss curve than N40 material, so we can conclude that the magnetic-core inductor built by P materials after scaling should have a higher loss and lower Q_L than the same size magnetic-core inductor built by N40 material and its scaling factor λ is thus larger than N40. But we can't decide which one is better between M3 and N40 materials for M3 has a lower P_V but a higher slope of the loss curve than N40. We thus M3 and N40 are both possible best materials and calculate their scaling factor λ by Eq. 5.28. We list the calculation results in Tab. 5.1 which also includes P material to confirm our conclusion. From Tab. 5.1, we can see that the magnetic-core inductor built by N40 still has the smallest scaling factor.

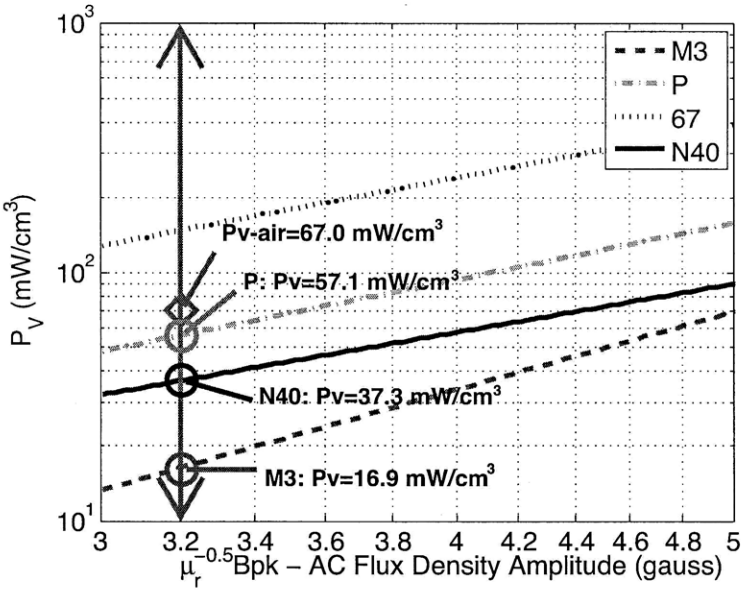

Figure 5.7: Loss plots of inductor design scaling example (OD= 12.7 mm, ID= 6.3 mm, Ht= 6.3 mm, $L = 200$ nH, $I_{pk} = 0.5$ A, $f_s = 30$ MHz and $B_{pk-air} = 3.2$ G).

Table 5.1: Comparison of scaling factor λ among magnetic-core inductors built by P, M3 and N40 materials and designed at $I_{pk} = 0.5$ A and $f_s = 30$ MHz.

Material	P	M3	N40
P_V (mW/cm^3)	57.1	16.9	37.3
μ_r	40	12	15
β	2.33	3.24	2.02
λ by Eq. 5.28	0.77	0.52	0.16

We check the flux density B'_{pk}, core loss P'_V, and copper loss $P_{V'-cu}$ of the magnetic-core inductor built by N40 material after scaling on the graph of P_V vs. $\mu_r^{-0.5}B_{pk}$ by Eq. 5.24, 5.26 and 5.29. In the example, $P'_V = 9621$ mW/cm^3 and $P'_{V-cu} = 6819$ mW/cm^3 are shown in Fig. 5.8. We can still see that the core loss of N40 is the lowest than other materials. If we build a magnetic-core inductor by other materials with the same size after scaling, the inductor will have a lower quality factor and must have a bigger size to satisfy the design requirement for minimum quality factor, which support our conclusion that the magnetic-core inductor built in N40 has the smallest size from another aspect.

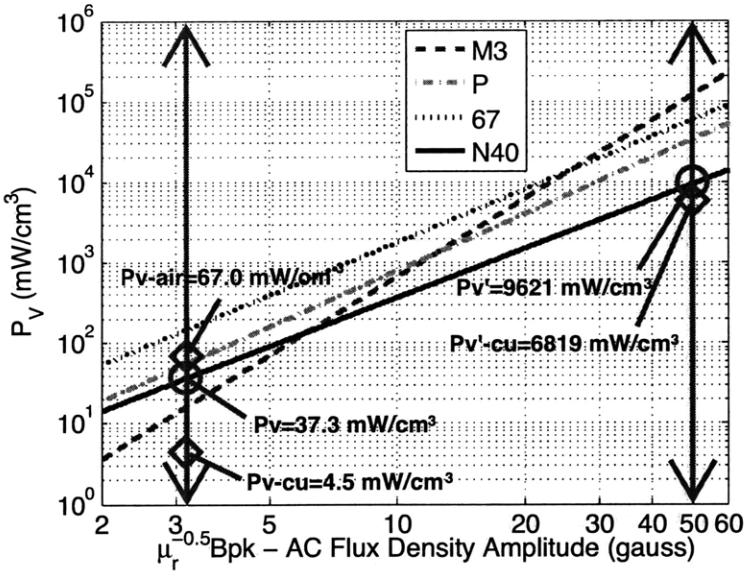

Figure 5.8: The magnetic-core inductor after scaling design

5.3.5 Inductor Design with the Best Magnetic Material

With the satisfied quality factor Q_L and inductor size, the inductor can be designed with the selected best magnetic material. The turns number N can be calculated by Eq. 5.6. In [47, 84], the windings can be made of either a foil-like conductor conforming to the shape or an equal-width foil-like conductor. The copper loss and core loss of the fabricated inductor has been estimated in the above subsections.

To provide a complete answer for the previous design example, we summarize the results of each step in Fig. 5.1:

1. We give the design requirements: L = 200 nH, I_{pk} = 2 A, f_s = 30 MHz, minimum Q_L = 116 and maximum size of OD= 12.7 mm, ID= 6.3 mm and Ht= 6.3 mm.

2. Given available magnetic materials (67, P, M3 and N40) and their Steinmetz parameters, we decide N40 is the best material for design.

3. Given the maximum size, estimate the highest Q_L of a magnetic-core inductor with N40 material about 171.

4. Given the minimum Q_L, estimate the scaling factor λ = 0.17 and the minimum size OD= 2.2 mm, ID= 1.1 mm and Ht= 1.1 mm calculated by Eq. 5.20.

5. We check the results in the third and fourth steps and see if they satisfy the design requirements. If they do, the inductor design is completed with the selected magnetic material. If they don't, it means the design requirements can't be satisfied even with the best available magnetic material. In that case, one must go back to the first step and revise inductor design requirements.

6. If we prefer to a core inductor with the highest Q_L as well as the maximum size, the inductor will have a a turns number $N = 4$ calculated by Eq. 4.16, an inductance $L = 199$ nH calculated by Eq. 4.17, the core size of OD= 12.7 mm, ID= 6.3 mm and Ht= 6.3 mm. Its quality factor Q_L has been estimated in Section 5.3.3. If we prefer to a core inductor with the minimum size, the inductor will have a turns number $N' = 10$ calculated by Eq. 5.22 and the core size are OD= 2.2 mm, ID= 1.1 mm and Ht= 1.1 mm.

Compared to a coreless design, the magnetic-core inductor with N40 material will have 47% higher quality factor Q_L for the same maximum size or 83% size reduction for the same minimum quality factor.

5.3.6 Relationship between Quality Factor Q_L and Inductor Size

The method to calculate the scaling factor λ proposed in Section 5.3.4 has two shortcomings: the first is that we may need to rely on some numerical methods to solve the nonlinear equation Eq. 5.28, and the second is that it doesnt reveal the relationship of a magnetic-core inductors quality factor and its size in a direct and understandable way. In this subsection, we study the inductors quality factor as the function of its scaling factor λ. We still begin with a coreless inductor with a specified L, I_{pk}, maximum size and f_s. We calculate its quality factor Q_{L0} and define its scaling factor $\lambda = 1$. We then calculate its B_{pk-air}, P_{V-air} and find P_V of each magnetic material at B_{pk-air} from the graph of P_V vs. $\mu_r^{-0.5} B_{pk}$. From Eq. 5.32 and 5.33, we finally draw the graph of Q_L vs. λ for each magnetic material, as well as a coreless inductor.

We again begin our derivations with a coreless inductor. We define quality factor Q_{L0} with given maximum size ($\lambda = 1$) and calculate it by the following equation:

$$Q_{L0} = \frac{\omega L}{R_{cu-air}} = \frac{\mu_0 f}{R_{cu-single-turn}} h \ln\left(\frac{d_o}{d_i}\right) \tag{5.30}$$

Because $R_{cu-single-turn}$ is constant during the scaling as described before, the quality factor after scaling can be calculated by the following equation:

$$Q_L(\lambda) = \frac{\omega L}{R_{cu}} = \frac{\mu_0 f}{R_{cu-single-turn}} h\lambda \ln\left(\frac{d_o \lambda}{d_i \lambda}\right) = \lambda Q_0 \tag{5.31}$$

From Eq. 5.31, we can see there is a linear functional relationship between quality factor Q_L and scaling factor λ for a coreless inductor. This general result for coreless design is well known; see the classic scaling rules for coreless solenoids, for example [3, 74, 105–107]. For a magnetic-core inductor, from Eq. 5.25,

$$R'_{cu} = \lambda^{-1}\mu_r^{-1}R_{cu-air} = \frac{\omega L}{\lambda \mu_r Q_0} \tag{5.32}$$

From Eq. 5.21 and 5.24,

$$\begin{aligned} R'_{co} &= \frac{P_{V'}V'}{0.5I_{pk}^2} = \frac{\lambda^{3-1.5\beta}P_V V}{0.5I_{pk}^2} = \lambda^{3-1.5\beta}\frac{P_V}{P_{V-air}}\frac{P_{V-air}V}{0.5I_{pk}^2} \\ &= \lambda^{3-1.5\beta}\frac{P_V}{P_{V-air}}R_{cu-air} = \lambda^{3-1.5\beta}\frac{P_V}{P_{V-air}}\frac{\omega L}{Q_{L0}} \end{aligned} \tag{5.33}$$

From Eq. 5.32 and 5.33,

$$Q_L(\lambda) = \frac{\omega L}{R'_{cu} + R'_{co}} = \frac{Q_{L0}}{\frac{1}{\lambda\mu_r} + \lambda^{3-1.5\beta}\frac{P_V}{P_{V-air}}} \tag{5.34}$$

Starting from a baseline design, from Eq. 5.31 and 5.34, we can plot Q_L vs. λ for magnetic-core inductors made in all available magnetic materials, as well as for a coreless inductor. An example is shown in Fig. 5.9. The baseline design specifications are $L = 200$ nH, $I_{pk} = 2$ A, $f = 30$ MHz, and $Q_L = 116$. At $\lambda = 1$, the coreless inductor has dimensions $d_o = 12.7$ mm, $d_i = 6.3$ mm and $h = 6.3$ mm. For a given Q_L, we can use results such as in Fig. 5.9 to find its scaling factor λ and further decide the inductor size for every magnetic material by Eq. 5.20. Moreover, for a given size (scaling factor λ), we can find the quality factor Q_L that is achievable for each material.

While this approach to explore inductor scaling and sizing is informative. It still has two shortcomings. The first one is that we have to generate a new graph by Eq. 5.31 and 5.34 for each baseline design of interest. The second one is that we can't a priori exclude some magnetic materials from consideration as we did in Section 5.3.4. If we have dozens of magnetic materials, the graph of Q_L vs. λ will become very complicated.

5.4 Optimization of Magnetic-core Inductors

In Section 5.3, different magnetic materials are compared and evaluated with the assumption that magnetic-core inductors made in all these materials have the same relative dimensions as the coreless design on which they are based. However, magnetic-core inductors may

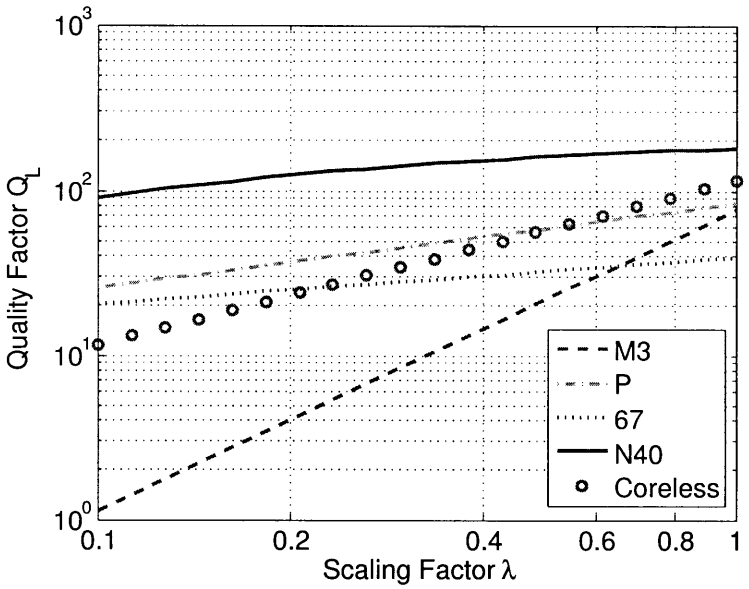

Figure 5.9: Q_L vs. λ for coreless inductor and magnetic-core inductors in different mangetic materials (L = 200 nH, I_{pk} = 2 A and f = 30 MHz). At $\lambda = 1$, the coreless inductor has the dimensions OD= 12.7 mm, ID= 6.3 mm and Ht= 6.3 mm.

have their own relative optimum dimensions for the maximum quality factor Q_L or the minimum size for different materials, thus the methods proposed in Section 5.3 may not be a fair comparison. That is, we need to establish whether or not the best *shape* for an inductor changes significantly with scale or material characteristics. In this section, we study optimization of magnetic-core inductors based on Steinmetz parameters of magnetic materials and make sure that our assumptions in Section 5.3 are reasonable.

As will be seen, the results are quite reasonalbe and the approaches of Section 5.3 lead to near optimum design under a wide range of conditions. We consider two optimization cases. Firstly, we assume a magnetic-core toroidal inductor's d_o and h are restricted to constant (e.g., as stipulated by the specification of a power electronics circuit), and we optimize d_i to get the maximum quality factor Q_L. Secondly, we assume that the *volume* of a magnetic-core inductor constant and we optimize d_o, d_i and h to obtain maximum quality factor. In both optimizations, make the assumption that core losses dominate and neglect copper loss. We do take into account the fact that the flux density inside the core is not uniform when calculating core loss.

5.4.1 Optimization of d_i at Fixed d_o and h

From Eq. 5.6,

$$B_{pk}(r) = \frac{\mu_0 \mu_r N I_{pk}}{2\pi r} = \frac{I_{pk}}{r}\sqrt{\frac{\mu_0 \mu_r L}{2\pi h \ln\left(\frac{d_o}{d_i}\right)}} \tag{5.35}$$

Where r specifies a radius from the center of the core ($\frac{d_i}{2} < r < \frac{d_o}{2}$). $P(d_i)$ is the total core loss as a function of the inside diameter d_i.

$$\begin{aligned} P(d_i) &= \int_{\frac{d_i}{2}}^{\frac{d_o}{2}} P_V \mathrm{d}V = \int_{\frac{d_i}{2}}^{\frac{d_o}{2}} K B_{pk}(r)^{\beta} 2\pi r h \mathrm{d}r \\ &= 2\pi h K \left[I_{pk}\sqrt{\frac{\mu_0 \mu_r L}{2\pi h \ln\left(\frac{d_o}{d_i}\right)}} \right]^{\beta} \int_{\frac{d_i}{2}}^{\frac{d_o}{2}} r^{1-\beta} \mathrm{d}r \end{aligned} \tag{5.36}$$

If $\beta \neq 2$,

$$P(d_i) = \frac{2\pi h K}{2-\beta}\left[I_{pk}\sqrt{\frac{\mu_0 \mu_r L}{2\pi h \ln\left(\frac{d_o}{d_i}\right)}} \right]^{\beta} \left[\left(\frac{d_o}{2}\right)^{2-\beta} - \left(\frac{d_i}{2}\right)^{2-\beta} \right] \tag{5.37}$$

If $\beta = 2$,

$$P(d_i) = \mu_0 \mu_r K L I_{pk}^2 \tag{5.38}$$

From Eq. 5.37 and 5.38, let $d_i = 0.5 d_o$: If $\beta \neq 2$,

$$P(0.5d_o) = \frac{2\pi h K}{2-\beta}\left[I_{pk}\sqrt{\frac{\mu_0 \mu_r L}{2\pi h \ln(2)}} \right]^{\beta} \left[\left(\frac{d_o}{2}\right)^{2-\beta} - \left(\frac{d_o}{4}\right)^{2-\beta} \right] \tag{5.39}$$

If $\beta = 2$,

$$P(0.5d_o) = \mu_0 \mu_r K L I_{pk}^2 \tag{5.40}$$

We normalize the total core loss $P(d_i)$ by the total loss P at $d_i = 0.5 d_o$. From Eq. 5.37 to 5.39, If $\beta \neq 2$,

$$\frac{P(d_i)}{P(0.5d_o)} = \left[\frac{\ln 2}{\ln\left(\frac{d_o}{d_i}\right)} \right]^{0.5\beta} \left[\frac{1 - \left(\frac{d_i}{d_o}\right)^{2-\beta}}{1 - 0.5^{2-\beta}} \right] \tag{5.41}$$

If $\beta = 2$,

$$\frac{P(d_i)}{P(0.5d_o)} = 1 \tag{5.42}$$

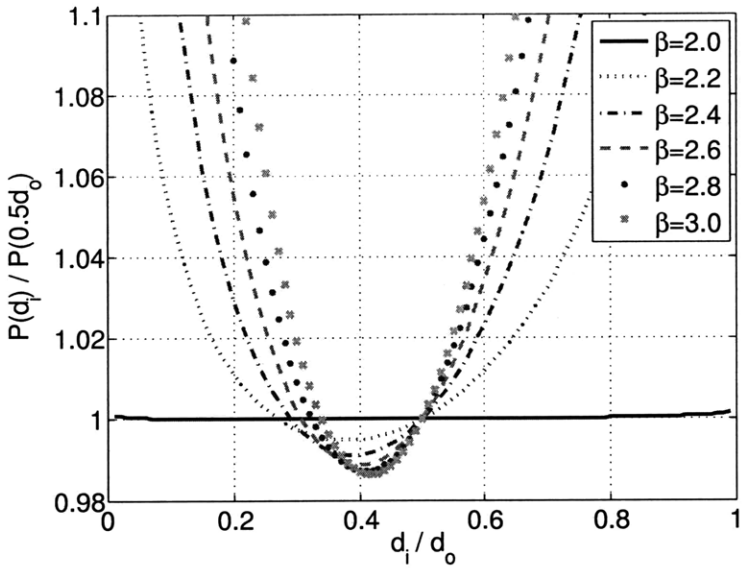

Figure 5.10: Plot of core power loss dissipation in a rectangular cross-section toroidal core as a function of $\frac{d_i}{d_o}$, normalized to that with $\frac{d_i}{d_o} = 0.5$. Results are parameterized in Steinmetz parameter β. It can be seen that over a wide range of β, $\frac{d_i}{d_o} = 0.5$ is very close to the optimum, and that results are not highly sensitive to $\frac{d_o}{d_i}$.

In Eq. 5.41, $\frac{P(d_i)}{P(0.5d_o)}$ only depends on the ratio of $\frac{d_o}{d_i}$ and Steinmetz parameter β. We plot P as a function of $\frac{d_o}{d_i}$ for different β in Fig. 5.10. From Fig. 5.10, we can see that the optimum d_i is around $0.4d_o$, with an exact value that depends β. When d_i varies between $0.22d_o$ and $0.64d_o$, the total core loss P is very flat and the deviation from the minimum core loss is less than 10%. We choose $d_i = 0.5d_o$ instead of $d_i = 0.4d_o$ for the following considerations: firstly, $d_i = 0.5d_o$ is a more typical dimension ratio for commercial magnetic cores (e.g., see Tab 5.2); secondly, as shown in Section 5.5, the error due to the assumption of average flux density is less than 10% if $d_i \leq 0.5d_o$. The error in assuming that the optimum inside diameter is $d_i = 0.5d_o$ is lower than 2% for a wide range of β values. So we can think $d_i = 0.5d_o$ as the nearly-optimum dimension for a wide range of magnetic materials. We can thus compare and evaluate different magnetic materials under the same dimensions and our assumption in Section 5.3 is correct. In Section 5.3.4, we also use the same assumption to investigate Eq. 5.9, 5.11 and 5.19.

5.4.2 For a Constant Volume V, Optimization of Dimensions d_o, d_i and h

In Eq. 5.38, if $\beta = 2$, core loss P is constant, independent of dimensions, If $\beta \neq 2$, similar to Eq. 5.37,

$$P(h, d_o, d_i) = \frac{2\pi h K}{2-\beta}\left[I_{pk}\sqrt{\frac{\mu_0\mu_r L}{2\pi h \ln\left(\frac{d_o}{d_i}\right)}}\right]^{\beta}\left[\left(\frac{d_o}{2}\right)^{2-\beta} - \left(\frac{d_i}{2}\right)^{2-\beta}\right] \tag{5.43}$$

$$h = \frac{4V}{\pi\left(d_o^2 - d_i^2\right)} \tag{5.44}$$

Eliminating h, we find:

$$P(V, d_o, d_i) = \frac{8KV}{(2-\beta)(d_o^2 - d_i^2)}\left[I_{pk}\sqrt{\frac{\mu_0\mu_r L(d_o^2 - d_i^2)}{8V \ln\left(\frac{d_o}{d_i}\right)}}\right]^{\beta}\left[\left(\frac{d_o}{2}\right)^{2-\beta} - \left(\frac{d_i}{2}\right)^{2-\beta}\right] \tag{5.45}$$

$$P\left(V, \frac{d_o}{d_i}\right) = \frac{8KV}{2-\beta}\left(I_{pk}\sqrt{\frac{\mu_0\mu_r L}{2V}}\right)^{\beta}\left[\sqrt{\frac{1-\left(\frac{d_i}{d_o}\right)^2}{\ln\left(\frac{d_o}{d_i}\right)}}\right]^{\beta}\left[\frac{1-\left(\frac{d_i}{d_o}\right)^{2-\beta}}{1-\left(\frac{d_i}{d_o}\right)^2}\right] \tag{5.46}$$

From Eq. 5.46, we know the total loss P only depends on the volume V and the ratio of d_i and d_o. If $\frac{d_i}{d_o}$ constant, we can get:

$$P\left(V, \frac{d_i}{d_o}\right) \propto V^{1-0.5\beta} \tag{5.47}$$

Because $\beta \geq 2$ in most materials, the total core loss P decreases as the inductor's volume V is increased. Larger volume will always help reduce core loss and improve quality factor Q_L in a magnetic-core inductor.

If we normalize P by $P(d_i = 0.5d_o)$:

$$\begin{aligned} P(V, 0.5) &= \frac{2KV}{2-\beta}\left(I_{pk}\sqrt{\frac{\mu_0\mu_r L}{2V}}\right)^{\beta}\left[\sqrt{\frac{1-2^{-2}}{\ln(2)}}\right]^{\beta}\left[\frac{1-2^{\beta-2}}{1-2^{-2}}\right] \\ &\approx \frac{2KV}{2-\beta}\left(I_{pk}\sqrt{\frac{\mu_0\mu_r L}{2V}}\right)^{\beta}\left[\frac{1-2^{\beta-2}}{0.75}\right] \end{aligned} \tag{5.48}$$

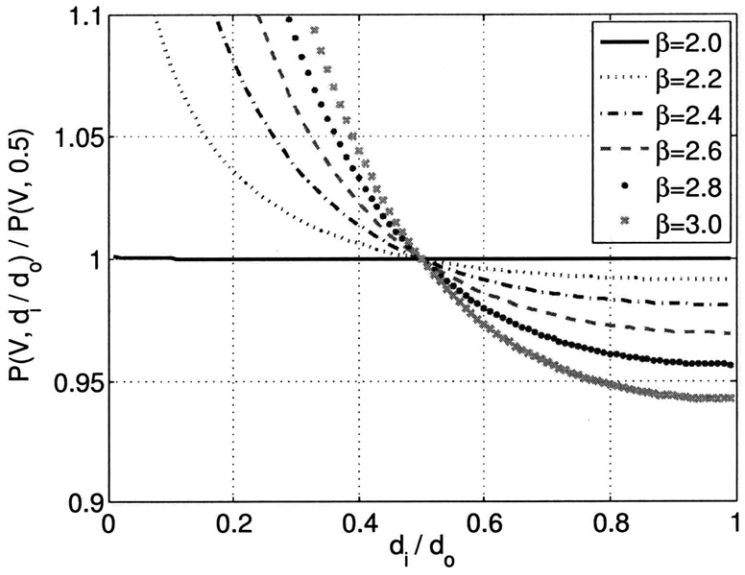

Figure 5.11: Core loss optimization for a constant volume.

For a constant volume V,

$$\frac{P\left(V, \frac{d_i}{d_o}\right)}{P(V, 0.5)} = \left[\sqrt{\frac{1-\left(\frac{d_i}{d_o}\right)^2}{\ln\left(\frac{d_o}{d_i}\right)}}\right]^{\beta} \left[\frac{1-\left(\frac{d_i}{d_o}\right)^{2-\beta}}{1-\left(\frac{d_i}{d_o}\right)^2}\right] \left[\frac{0.75}{1-2^{\beta-2}}\right] \tag{5.49}$$

Notice that in Eq. 5.49 the normalized P only depends on the material's Steinmetz parameter β and the ratio of d_i to d_o, independent of V and other individual dimension parameters (e.g., d_o, d_i, or h). Fig. 5.11 plots the normalized P vs. $\frac{d_i}{d_o}$. For $d_i > 0.3d_o$, the total loss P is flat and almost constant. Thus we can conclude that to a first approximation the total loss P only depends on the inductors volume V, and is independent of its dimensions d_i, d_o, and h when $d_i > 0.3d_o$. In other words, for a given total core loss P, there is only one solution for the volume V that will achieve it, but there are many solutions for the dimensions d_i, d_o, and h that can be used. Moreover, from this result we can conclude that we needn't concern ourselves with the optimum geometry changing with absolute scale (in terms of core loss), so may confidently use the results of Section 5.3 in finding an optimum inductor design.

5.5 Approximations Used in the Proposed Methods

In our inductor design procedure shown in Section 5.3, we average the flux density inside a toroidal core to simplify our calculations. We average flux density B_{pk-air} to find the inductor average P_V (power loss per unit volume) of each magnetic component, and compare them at the average B_{pk-air}. We also use the average P_V to calculate the total core loss and quality factor Q_L further in Eq. 5.15 and 5.16. Because the flux density inside a toroidal core is actually not uniform, we need to know if our approximation is reasonable. In this section, we check the accuracy of this approximation and calculate the error it causes.

For a magnetic-core inductor, the average flux density is:

$$B_{pk} = \frac{\mu_0 \mu_r N I_{pk}}{0.5\pi(d_o + d_i)} = \frac{I_{pk}}{0.25(d_o + d_i)} \sqrt{\frac{\mu_0 \mu_r L}{2\pi h \ln\left(\frac{d_o}{d_i}\right)}} \tag{5.50}$$

The average total core loss:

$$\begin{aligned} P_{AVG}(d_i) &= P_{V-AVG} V = K B_{pk}^{\beta} \pi \left[\left(\frac{d_o}{2}\right)^2 - \left(\frac{d_i}{2}\right)^2\right] h \\ &= \pi h K \left[\frac{I_{pk}}{0.25(d_o + d_i)} \sqrt{\frac{\mu_0 \mu_r L}{2\pi h \ln\left(\frac{d_o}{d_i}\right)}}\right]^{\beta} \left[\left(\frac{d_o}{2}\right)^2 - \left(\frac{d_i}{2}\right)^2\right] \end{aligned} \tag{5.51}$$

In Section 5.3, the total core loss P is calculated without the approximation of uniform flux. We compare P and P_{AVG} and define the error by the following equation:

$$Error = 1 - \frac{P_{AVG}(d_i)}{P(d_i)} \tag{5.52}$$

from Eq. 5.37 and 5.51, if $\beta \neq 2$,

$$Error = 1 - (2 - \beta) 2^{\beta - 1} \frac{\left[1 - \left(\frac{d_i}{d_o}\right)^2\right] \left(1 + \frac{d_i}{d_o}\right)^{-\beta}}{1 - \left(\frac{d_i}{d_o}\right)^{2-\beta}} \tag{5.53}$$

from Eq. 5.38 and 5.51, if $\beta = 2$,

$$Error = 1 - 2 \frac{1 - \left(\frac{d_i}{d_o}\right)^2}{\left(1 + \frac{d_i}{d_o}\right)^2 \ln\left(\frac{d_o}{d_i}\right)} \tag{5.54}$$

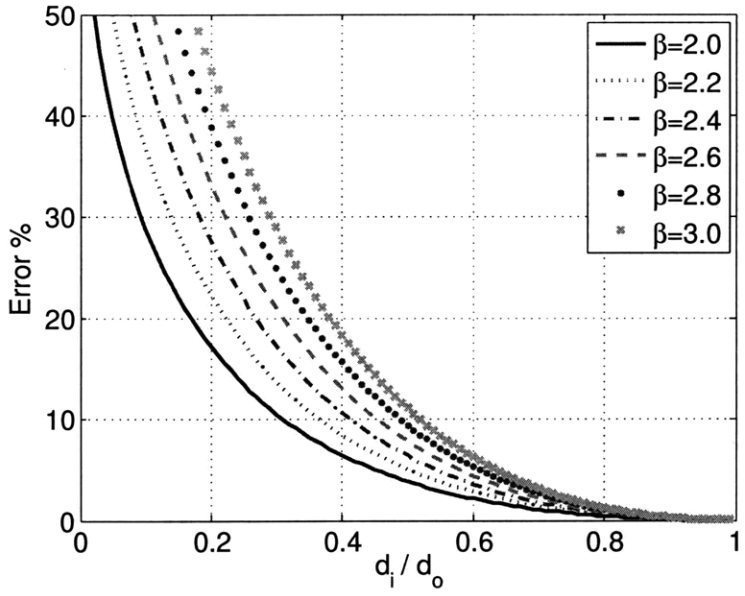

Figure 5.12: The error of average flux density approximation.

We can see *Error* only depends on the magnetic material Steinmetz parameter β and the dimension ratio of d_i to d_o. Error is plotted in Fig. 5.12 for different $\frac{d_i}{d_o}$ and β. We can see it is below 10% if β is less than 3 and $\frac{d_i}{d_o} > 0.52$ which is typical for most of available commercial magnetic cores. We assume an optimum $d_i \approx 0.5 d_o$ in Section 5.4. So the error of this approximation should be lower than 10%, which is reasonable.

5.6 Experimental Verification

We carried several experiments to verify the design procedure illustrated in this chapter. Firstly, we want to verify the design steps 2 and 3 in Fig. 5.1. That is, given available magnetic materials and design requirements (inductance L, current amplitude I_{pk}, and frequency f_s), we want to determine the best material to yield maximum quality factor Q_L for a given size, and estimate the highest Q_L that can be achieved at that size. Design parameters for the example application are repeated here: $d_o = 12.7$ mm, $d_i = 6.3$ mm, $h = 6.3$ mm, $L = 200$ nH, $I_{pk} = 2$ A, and $f_s = 30$ MHz. As predicted in our design procedure, N40 is the best material and the magnetic-core inductor with N40 has quality factor $Q_L = 171$. We designed and fabricated a magnetic-core inductor with copper foil and N40 core to satisfy the design specifications, and measured its inductance and quality factor by experimental methods in [84] and Chapter 4. To make comparison with other designs, we fabricated a coreless inductor and magnetic-core inductors with 67, M3 and P

materials and similar core sizes. We calculated each inductor's turns number N by Eq. 4.16. estimated its inductance L by Eq. 4.17 and estimated, its quality factor Q_L by the method introduced in Section 5.3.3 according to its own dimensions. The results are listed and compared in Table 5.2. We can see the measurement results fit very well with the predicted values and the magnetic-core inductor with N40 material is the best design compared to others as we have predicted in our design procedure.

Table 5.2: Comparison among coreless inductors and magnetic-core inductors designed at $I_{pk} = 2$ A and $f_s = 30$ MHz in different magnetic materials.

Material	N40	M3	P	67	Coreless
Suppliers	Ceramic Magnetics	National Mag--netics Group	Ferronics	Fair-rite	N/A
Permeability	15	12	40	40	1
Designations	T502525T	998	11-250-P	5967000301	N/A
d_o (mm)	12.7	12.7	12.7	12.7	12.7
d_i (mm)	6.3	7.9	7.9	7.2	6.3
h (mm)	6.3	6.4	6.4	5.0	6.3
Turns Number N	4	5	3	3	14
Predicted L (nH)	199	180	219	203	173
Measured L (nH)	230	181	262	235	245
Predicted Q_L	171	74	81	39	116
Measured Q_L	167	65	87	45	96

Secondly, we verified the design step 4 illustrated in Section 5.3.4. That is, given L, I_{pk}, f_s and the minimum Q_L, determine the best material for design and estimate the minimum size achievable for that Q_L requirement. This experiment is much more difficult than the first one because availability of core sizes are limited and fabricating a tiny inductor is hard. If we design a magnetic-core inductor with N40 material which has the scaling factor $\lambda = 0.17$ as calculated in Section 5.3, the inductor after scaling has 10 turns and dimensions $d'_o = 2.16$ mm, $d'_i = 1.07$ mm and $h' = 1.07$ mm. The winding of copper foil has a width of less than 0.34 mm. It is very hard to wind such a narrow copper foil on this tiny core by hand. The magnetic-core inductor with P material in Section 5.3.4.5 has a higher scaling factor λ and thus a larger core size after scaling. So we verified the design of P material illustrated in Section 5.3.4.5 instead of N40. The design parameters are repeated here: $L = 200$ nH, $I_{pk} = 0.5$ A, $f_s = 30$ MHz and $Q_L = 116$. The scaling factor $\lambda = 0.77$ calculated by Eq. 5.28 and shown in Table 5.1. The core dimensions after scaling are $d'_o = 9.78$ mm, $d'_i = 4.85$ mm and $h' = 4.85$ mm. The available core with the closest size has dimensions OD= 9.63 mm, ID= 4.66 mm and Ht= 3.21 mm. Its OD and ID are satisfied, but Ht of this core is about

34% lower than the design requirement. The core's volume V is thus about 34% lower. From Eq. 5.47, the total core loss P is proportional to $V^{1-0.5\beta}$ and the quality factor Q_L is thus reversely proportional to $V^{1-0.5\beta}$ if the core loss dominates the total losses. Given 34% lower V and $\beta = 2.33$ of P material at 30 MHz, the error of Q_L due to Ht is as low as 7%. So this core can satisfy our design requirements. We designed and fabricated a 3-turn magnetic-core inductor with P materials and measure its inductance L and quality factor inductor Q_L. The results are shown in Table 5.3. We can see the measurement results fit very well with predicted value (for the actual size) and Eq. 5.28 is thus verified.

Table 5.3: Magnetic-core inductor designed at $L = 200$ nH, $I_{pk} = 0.5$ A and $f_s = 30$ MHz with the scaling factor $\lambda = 0.77$.

Material	Designation	d'_o (mm)	d'_i (mm)	h' (mm)
P	11-220-P	9.63	4.66	3.21
Turns Number N	Predicted L (nH)	Measured L (nH)	Predicted Q_L	Measured Q_L
3	168	181	110	105

Thirdly, we verified Eq. 5.34 and the relationship of Q_L vs. λ shown in Fig. 5.9. The design parameters are repeated here: $L = 200$ nH, $I_{pk} = 2$ A and $f_s = 30$ MHz. At $\lambda = 1$, the coreless inductor has the dimensions OD= 12.7 mm, ID= 6.3 mm and Ht= 6.3 mm. We design a magnetic-core inductor with N40 material and scaling factor $\lambda = 0.5$. The magnetic-core inductor after scaling thus has dimensions $d'_o = 6.35$ mm, $d'_i = 3.15$ mm and $h' = 3.15$ mm. The available core with closest size has the dimensions OD= 5.84 mm, ID= 3.05 mm and Ht= 4.06 mm. We designed and fabricated a 5-turn magnetic-core inductor with N40 materials and measure its inductance L and quality factor inductor Q_L. The results are shown in Table 5.4. We can see the measurement results fit very well with predicted value (for the actual size) and thus Eq. 5.28 and Fig. 5.9 are verified.

Table 5.4: Magnetic-core inductor designed at $L = 200$ nH, $I_{pk} = 2$ A and $f_s = 30$ MHz with the scaling factor $\lambda = 0.5$.

Material	Designation	d'_o (mm)	d'_i (mm)	h' (mm)
N40	T231216T	5.84	3.05	4.06
Turns Number N	Predicted L (nH)	Measured L (nH)	Predicted Q_L	Measured Q_L
5	198	180	160	154

5.7 Conclusion

In this chapter, we propose an inductor design procedure using low permeability magnetic materials. The design procedure is based on the use of Steinmetz parameters. With this procedure, different magnetic materials are compared fairly and fast, and both the quality factor Q_L and the size of a magnetic-core inductor can be predicted before the final design. We also compare a magnetic-core inductor design to a coreless inductor design in our design procedure. Some problems, such as optimization of magnetic-core inductors, are also investigated in this chapter. The procedure and methods proposed in this chapter can help to design a magnetic-core inductor with low-permeability rf core materials.

Chapter 6

Summary and Conclusions

This thesis focuses on circuit design techniques and passive components for high efficiency power converters operating at very high frequencies. Circuit design techniques investigated in this thesis include resistance compression networks, which serve to substantially decrease the variation in effective resistance seen by a tuned rf inverter as loading conditions change, and lumped (inductor and capacitor) matching networks operating at high efficiency ($> 95\%$). The thesis explores the operation, performance characteristics, and design considerations of these circuits, and presents experimental results demonstrating their performance. The thesis also investigates the loss characteristics of several commercial rf magnetic materials for VHF and describes an inductor design procedure with these materials based on characterization results. The loss characteristics of these materials, which have not previously been available, are illustrated and compared in tables and figures. The thesis proposes an inductor design procedure with low permeability magnetic materials, and provides methods to compare and evaluate different magnetic materials for given design specifications. The proposed design procedure has been verified by experimental results.

6.1 Thesis Summary

Chapter 1 introduces the background and motivation of very high frequency power conversion, outlines the challenges in aspects of circuit design and passive components, summarizes the thesis objectives and contributions to solve these challenges, and illustrates the organization of the whole thesis.

Chapter 2 describes the general attributes of resistance compression networks for radio frequency power conversion. The operation, performance, and design of these networks are explored and experimental results are presented to confirm the analysis. The use of resistance compression to benefit very high frequency dc-dc power converters is demonstrated in a prototype dc-dc converter operating at 100 MHz. We also consider other behavior of resistance compression networks in this chapter, including "phase compression" of the load impedance.

Chapter 3 presents analysis and design considerations for lumped (inductor and capacitor) matching networks operating at high efficiency (e.g., $> 95\%$). Formulas for calculating matching network efficiency are given, and it is shown that efficiency can be expressed as a function of inductor quality factor, capacitor quality factor, and transformation ratio. These formulas are used to evaluate the optimum number of L-section matching stages as a function of conversion ratio. Both simulation and experimental results are presented that validate the analytical formulation.

Chapter 4 investigates the loss characteristics of several commercial rf magnetic materials for use in power conversion applications in the 10 MHz to 100 MHz range. A measurement method is proposed that provides a direct measurement of inductor quality factor Q_L as a function of inductor current at rf frequencies, and enables indirect calculation of core loss as a function of flux density. Possible sources of error in measurement and calculation are evaluated and addressed. The proposed method is used to identify loss characteristics of different commercial rf magnetic core materials. The loss characteristics of these materials, which have not previously been available, are illustrated and compared in tables and figures.

Chapter 5 presents a procedure for designing inductors with low-permeability magnetic materials. The design procedure is based on the use of Steinmetz parameters, which have been characterized in Chapter 4. With this procedure, different magnetic materials can be quickly compared, and both the quality factor Q_L and the size of a magnetic-core inductor can be predicted before the final design. We compare a magnetic-core inductor design to a coreless inductor design in our design procedure. Some problems, such as optimization of ungapped magnetic-core inductors, are also investigated in this chapter. The procedure and methods proposed in this chapter can help to design a magnetic-core inductor with low-permeability rf core materials. The design procedure has been verified by experiments.

6.2 Thesis Conclusion

Together, the developments in this thesis can be used to advance the design of high-frequency power converters. A major limitation of resonant dc-dc converter circuits is the sensitivity of the inverter stage to loading conditions. The resistance compression networks introduced in Chapter 2 serve to substantially decrease the variation in effective resistance seen by a tuned rf inverter as loading conditions change, and expand the range of applications for which high-frequency resonant power conversion is viable.

Resistance compression networks effectively act as a new class of matching network and their efficiency can be analyzed by similar methods as to those presented in Chapter 3.

For example, for analyzing efficiency we could think of the resistance compression network in Fig. 2.1(b) as composed of a low-pass matching network as in Fig. 3.1(a) and a high-pass matching network as in Fig. 3.1(b) in shunt at the left-hand port, and in which the shunt capacitor C_P in Fig. 3.1(a) and the shunt inductor L_P in Fig. 3.1(b) are resonant and cancelled. We get the transformation ratio of the resistance compression network in Fig. 2.1(b):

$$Q_T = Q_s = \frac{Z_0}{R} \tag{6.1}$$

Z_0 and R are defined in Chapter 2, and Q_T and Q_s are defined in Chapter 3. If we assume inductor loss far exceeds capacitor loss, we can calculate the efficiency of the resistance compression network in Fig. 2.1(b) by the following equation:

$$\eta \approx 1 - \frac{Q_T}{2Q_L} = 1 - \frac{Z_0}{2RQ_L} \tag{6.2}$$

From Eq. 6.2, we can see the efficiency of resistance compression networks is also limited by its inductor quality factor Q_L and transformation ratio Q_T, with the added consideration that efficiency varies with the load resistance. We can get similar results for the resistance compression network in Fig. 2.1(b), the four element compression networks in Fig. 2.4, and the resistance compression network with high impedance resonant tank in Fig. 2.16. The results of Chapter 3 thus give us insight into the behavior of the new circuits of Chapter 2.

As analyzed in Chapter 4, the efficiency of matching networks (and thus resistance compression networks) can be improved through magnetics with higher quality factor. However, the quality factor of a coreless inductor is limited by its physical dimensions and very hard to increase without increasing size. As investigated in Chapters 4 and 5, magnetic-core inductors with low-permeability magnetic materials may have a higher quality factor and power density compared to coreless inductors at a given size. Thus the efficiency of matching network and resistance compression networks can be further improved by magnetic-core designs. The application of magnetic-core inductor with N40 material has been successfully demonstrated in Section 4.5 and its performance has been shown to be much superior than that of the original coreless inductor. By methods illustrated in Chapter 5, magnetic-core inductors can be designed with the selected best magnetic material and both the quality factor and size of the magnetic-cored inductors can be estimated.

In conclusion, Chapter 2 and 3 explore the design of passive networks that are key to VHF power conversion. The methods of Chapter 3 illustrate the relationship of the efficiency of such networks and inductor quality factor. Chapters 4 and 5 study the possibility of further increasing inductor quality factor with low-permeability magnetic materials, with materials characterized in Chapter 4 and design methods presented in Chapter 5. Besides impedance transformation and compression, magnetics also have applications such as intermediate

energy storage, wave shaping and filtering in rf power conversion. Similar analysis methods and results in this thesis can also be applied in these applications.

6.3 Recommendations for Future Work

There are several directions for future work in aspects of circuit design technique and passive components for very high frequency power conversion:

1. VHF transformers: As shown in Chapter 3, for a high transformation ratio, the efficiency of impedance transformation can be optimized by a multi-stage matching network. However, this means the transformation stage needs more passive components and occupies more space in the converter. Another disadvantage of matching networks for transformation is that they can be only designed under one specific frequency and one load impedance value. Moreover, when the transformation ratio is high, a single matching network becomes very sensitive to parasitics, error of passive components and error of the frequency [34]. For the above reasons, matching network may not be proper for applications requiring high transformation ratio, wide bandwidth or wide load range transformations. Voltage transformation can be also realized by a resonant transformer. Compared to matching networks, resonant transformers may have a higher efficiency than matching networks, especially when the transformation ratio is high. Unlike transformers are working at low frequency, there is a lack of literature about design of very high frequency transformers, and both the theory and fabrication of these transformers applied in very high frequency resonant dc-dc converters are not very clear. At high frequencies, the impact of parasitics must be carefully considered. Efficiency may be optimized by transformers parameters and extra passive components [108, 109]. Compared to a matching network, a resonant transformer has more parameters to be controlled. Nevertheless, a resonant transformer may enable one to integrate more passive components in the circuit. For example, the transformer may be integrated as part of inverter and rectifier and the volume of converter is further reduced in this way. Magnetic-core transformers may be realized based on the low-permeability magnetic materials we have characterized in this thesis, but the modeling, design, optimization, integration and fabrication techniques of high frequency resonant transformers need to be further explored. A design procedure for a magnetic-core transformer could be developed as an extension of our magnetic-core inductor design procedure described in Chapter 5.

2. Transmission line transformers: Using transmission line transformers is another possible impedance transformation method in rf circuits [29–31]. They have the advantage of wide bandwidth compared to tuned transformers and matching networks. The leakage

inductances and interwinding capacitances are generally absorbed (in a distributed form) into the characteristic impedance of a transmission line. As a result, the high frequency response is less limited by parasitics [29–31]. However, in order to get a high efficiency transformer (i.e. with a large magnetizing inductance for low core loss), the volume may be very large which is unacceptable in most of high frequency dc-dc converters. Moreover, the range of conversion ratios which may be readily achieved is limited with this technique. Nevertheless, transmission line transformer designs merit further development for VHF power applications, and their performance should be compared with other transformation methods.

3. Converter simplification techniques (passive component combination techniques): In order to reduce the volume of dc-dc converters further, the topology of converter should be as simple as possible. As discussed above, passive components, especially inductors and capacitors, often comprise most of the volume of a converter. Within the constraint of satisfying the design requirements, the passive components should be combined, minimized in size, or eliminated. In Fig. 1.1, the converter consists three stages: inverter, impedance transformation and rectifier. These stages can be realized by different circuit modules independently. However, the converter realized in this way employs numerous components, increasing circuit volume. Techniques to combine passive components need to be developed. By these techniques, components in different stages may be combined together and the boundary between different stages will be blurred. The combined component can serve in two or three stages. For example, the inductor in the matching network may be combined with the resonant inductor of the inverter [26, 27]. This inductor may also be combined with the resonant rectifier inductor. Both combinations can eliminate one inductor. In pursuing component reduction and integration of function, great care will be taken to make positive use of unavoidable circuit parasitics and to preserve flexibility of design. The type of approach that could be pursued is exemplified by the reduced-component-count Class E converters described in [15], and by the use of transformer parasitic inductances to implement both the rectifier inductor and part of the resonant inductor. For example, in a Class-Φ-inverter-based dc-dc converter, the resonant transformer with well controlled leakage inductance, magnetizing inductance, and turns ratio may replace the input inductor, resonant inductor, transformation stage and rectifier inductor at the same time [110]. The largest challenge in realizing such a design may be the fabrication of transformer according to the specified leakage inductance, magnetic inductance and turns ratio while keeping low profile and high efficiency. The transformer may be designed and fabricated based on toroidal magnetic-core structures, or planar structures as in [110].

4. EMI evaluation and mitigation: The EMI generated by high frequency resonant dc-dc converters needs to be better characterized and evaluated. The results should be compared to industry standards. The impacts of self-shielding components and system level

shielding on EMI should be investigated. Both self-shielding and un-shielded magnetic components introduced in this thesis should be explored and quantified with EMI considerations in VHF converters.

Appendix A

Layout of Four-element Compression Network

Fig. A.1 shows the layout of the test board for four element compression networks associated with Fig. 2.6 and Fig. 2.7. Capacitors and resistors are soldered on the top side of the printed circuit board and inductors are soldered on the bottom side. Fig. A.2 shows the layout of the resistance compression network and rectifiers for the system demonstrated in section 2.5. The compression network and rectifier are laid out on a separate board (2-sided 0.064″ thick FR4) from the Class E inverter and control circuits. More details about this design and layout may be found in [2].

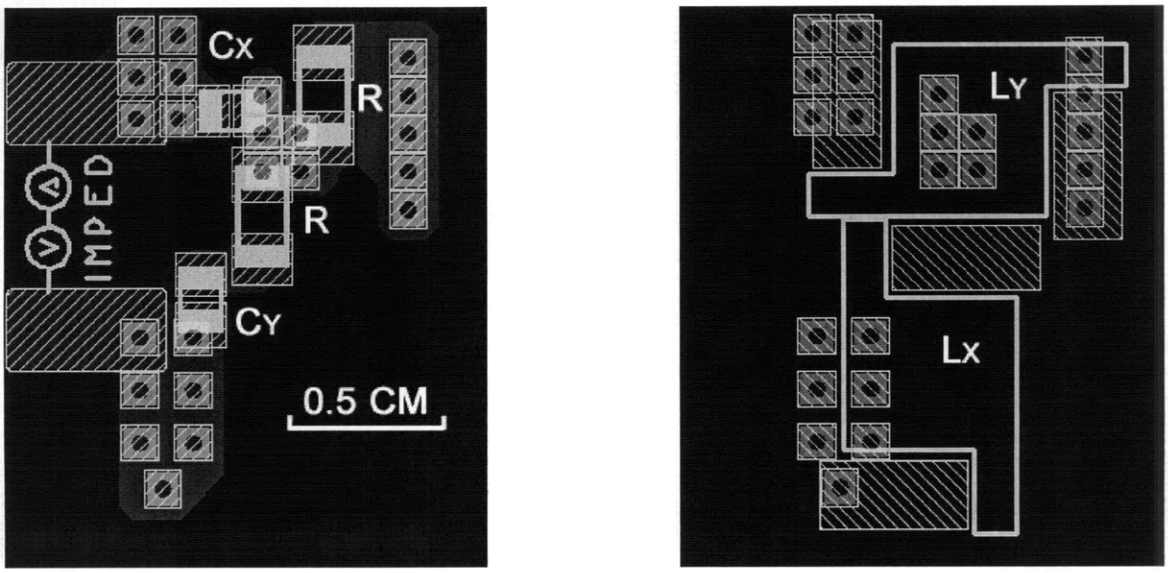

(a) (b)

Figure A.1: The layout of four element compression network test board, top (Fig. A.1(a)) and bottom (Fig. A.1(b)). This layout associated with Fig. 2.6 and Fig. 2.7.

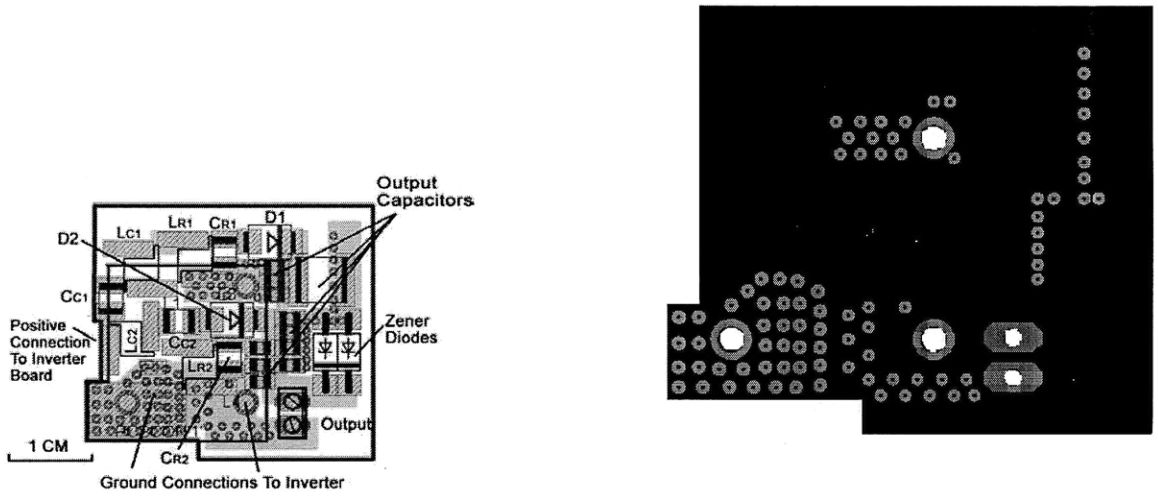

(a) (b)

Figure A.2: The compression network and rectifier PCB layout, top (Fig. A.2(a)) and bottom (Fig. A.2(b)). This layout associated with Fig. 2.16 and Fig. 2.17 [2].

Appendix B

Layout of Back-to-back Matching Network

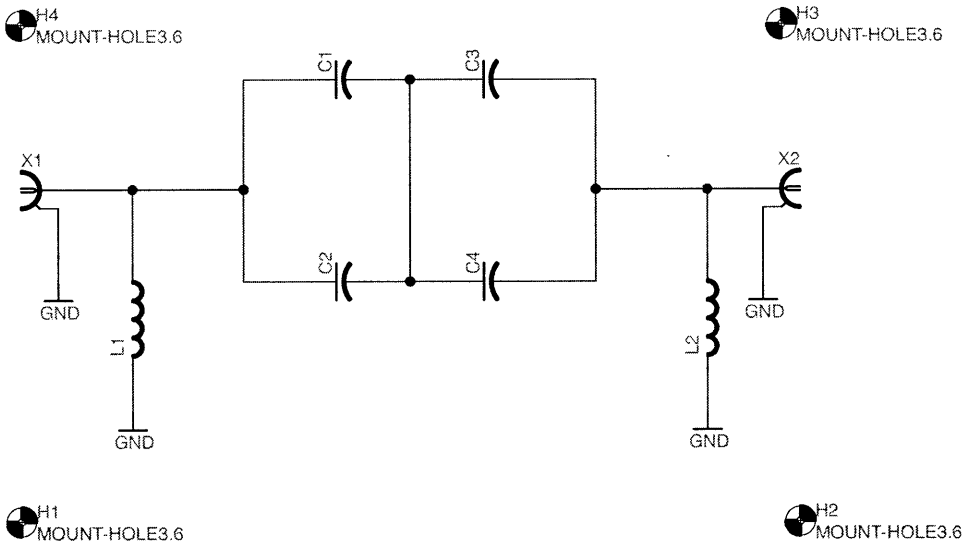

Figure B.1: Back-to-back matching network PCB schematic.

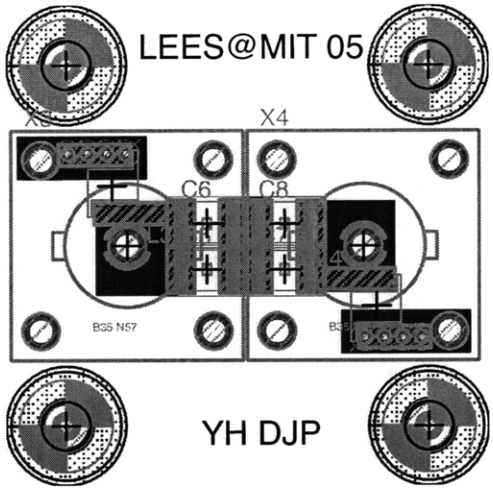

Figure B.2: Back-to-back matching network PCB board. Top layer.

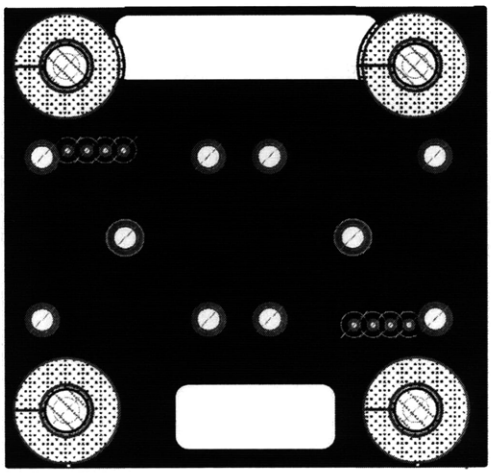

Figure B.3: Back-to-back matching network PCB board. Bottom layer.

Appendix C

Layout of the Circuit for Measuring Inductor Quality Factor

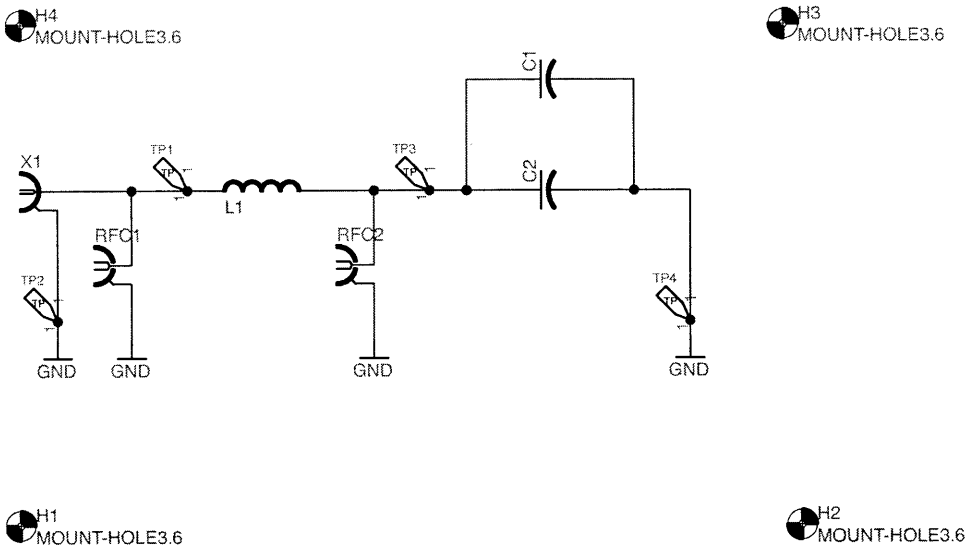

Figure C.1: Circuit for measuring inductor quality factor PCB schematic.

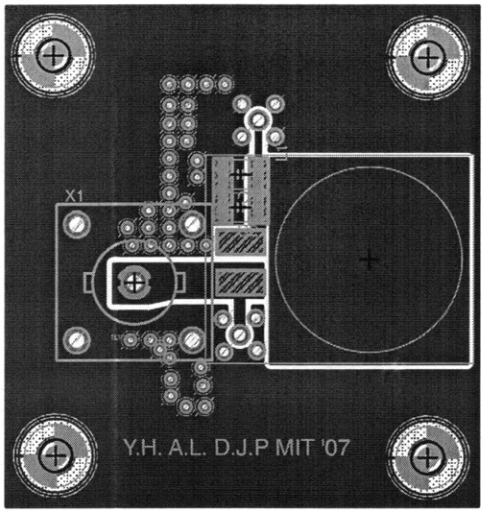

Figure C.2: Circuit for measuring inductor quality factor PCB. Top layer.

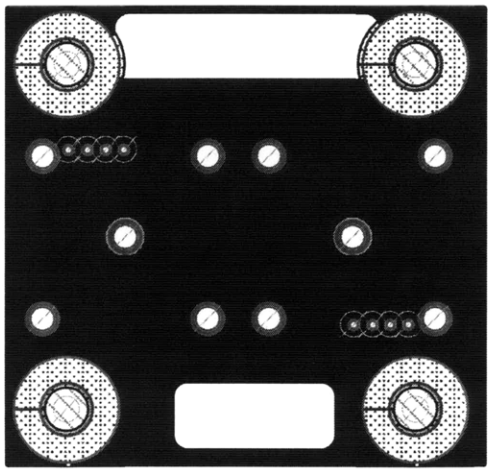

Figure C.3: Circuit for measuring inductor quality factor PCB. Bottom layer.

Appendix D

Finite Element Simulations of Copper Loss of a Magnetic-core Inductor

---

In Section 4.3.2, the conductor resistance R_{cu} of a magnetic-core inductor is estimated by fabricating a coreless inductor with the same dimensions and measuring its R_{cu} by an impedance analyzer. In this appendix, we calculate the error of the estimation using finite element simulations results. We seek to simulate a magnetic-core inductor with the same dimensions as the one with N40 material in Section 4.5 at $f_s = 30$ MHz and $I_{pk} = 2$ A. The inductor has 4-turns and is wound with 0.1 mm thick copper foil having width $w_{cu} = 2.0$ mm. The core has dimensions OD= 12.7 mm, ID= 6.3 mm and Ht= 6.3 mm. The skin depth of copper at 30 MHz is about 0.012 mm, which is very small compared to the core and foil's dimensions. So it will consume a lot of time and computer sources to simulate this kind of inductor in three dimensions.

To accelerate simulations, we simplified the 3D simulation by instead using two 2D simulations in Maxwell 2D. The 2D simulation models are shown in Fig. D.1 and D.2. We assume that the core is lossless and we can specify the relative permeability of the core material in simulations. Each turn of windings is approximated by four pieces of copper foil with infinite length. In Fig. D.1, Cuj-1 (j=1:4) models the piece on the top surface of the core and Cuj-3 models the piece on the bottom surface. The average space between Cuj-1 and Cuj-3 is 4 mm. The original toroidal shape of the core is approximated by a rectangular shape with infinite length in Fig. D.1. To reduce the error near the end of the rectangular core, the pieces Cu2-1/3 and Cu3-1/3 are repeated. In Fig. D.2, Cuj-2 models the piece on the inner surface and Cuj-4 models the piece on the outer surface. We simulated the copper loss of each piece for the core material with different permeability. Because these winding turns are symmetrical, we just need to record the simulation results of Cu1-k (k=1:4) in Table D.1, and we have R_{cu}(Cuj-k)=R_{cu}(Cu1-k) for j=2:4. We define the error between a magnetic-core inductor and a coreless inductor as:

$$Error\% = 1 - \frac{R_{cu}(\mu_r = 1)}{R_{cu}(\mu_r > 1)} \tag{D.1}$$

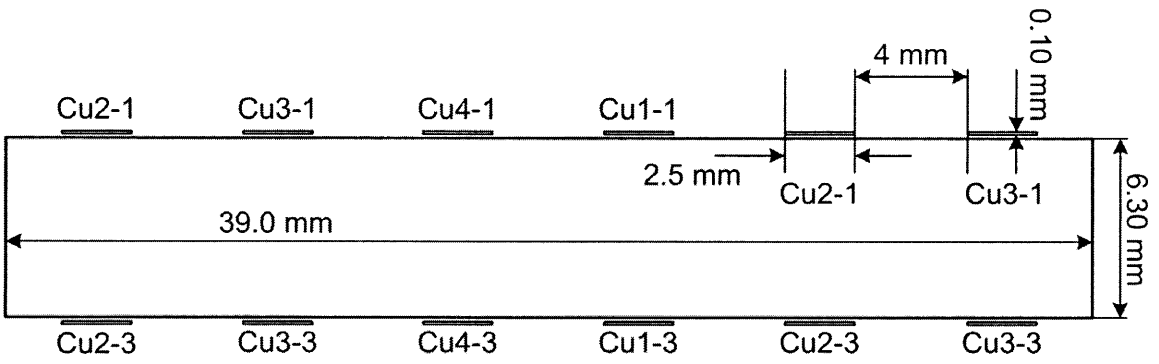

Figure D.1: 2D model of copper-foil windings on the top and bottom surfaces of an inductor.

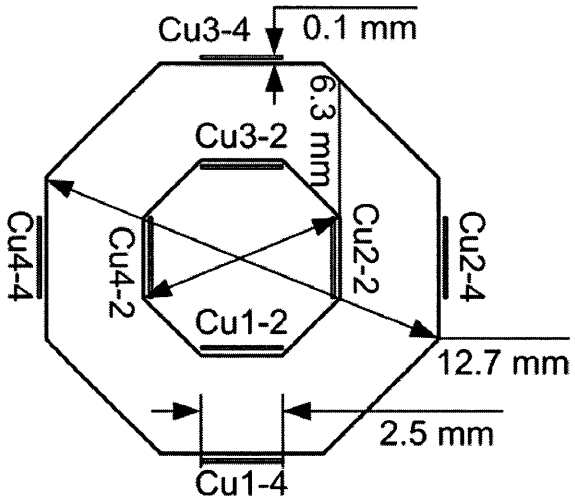

Figure D.2: 2D model of copper-foil windings on the inner and outer surfaces of an inductor.

From these finite element simulation results, we can see that the R_{cu} of a magnetic-core inductor is close to that of a coreless inductor for $\mu_r < 4$. When $\mu_r \geq 4$, R_{cu} for a coreless inductor can be lower than the R_{cu} of a magnetic-core inductor by up to 30% in average.

Table D.1: Finite simulation results of copper losses of a coreless inductor and magnetic-core inductor with variant permeabilities.

	Cu1-1		Cu1-2		Cu1-3		Cu1-4		Net *Error*
Permea--bility μ_r	R_{cu} (Ω/m)	*Error* (%)	R_{cu} (Ω/m)	*Error* (%)	R_{cu} (Ω/m)	*Error* (%)	R_{cu} (Ω/m)	*Error* (%)	for the whole winding (%)
1	0.75	0	0.78	0	0.75	0	0.60	0	0
2	0.83	9.6	0.82	4.9	0.83	9.6	0.73	18	11
4	0.85	12	0.84	7.1	0.87	14	0.83	28	16
10	0.96	22	0.87	10	0.95	21	0.95	37	23
20	0.97	23	0.88	11	0.98	23	1.00	40	25
40	0.98	23	0.88	11	1.00	25	1.01	41	25

Bibliography

[1] N. Sokal. Class-E rf power amplifiers. *QEX*, pages 9–20, Jan./Feb. 2001.

[2] D. Jackson. Design and characterization of a radio-frequency dc–dc power converter. Master's thesis, Massachusetts Institute of Technology, Jun. 2005.

[3] D. Perreault, J. Hu, J. Rivas, Y. Han, O. Leitermann, R. Pilawa-Podgurski, A. Sagneri, and C. Sullivan. Opportunities and challenges in very high frequency power conversion. *24th Annu. IEEE Applied Power Electronics Conf. and Expo.*, pages 1–14, Feb. 2009.

[4] J. Rivas, R. Wahby J. Shafran, and D. Perreault. New architectures for radio-frequency dc–dc power conversion. *35th IEEE Power Electronics Specialists Conf.*, pages 4074–4084, Jun. 2004.

[5] S. Djukić, D. Maksimović, and Z. Popović. A planar 4.5-GHz DC-DC power converter. *IEEE Trans. Microw. Theory Tech.*, 47(8):1457–1460, Aug. 1999.

[6] R. Pilawa-Podgurski, A. Sagneri, J. Rivas, D. Anderson, and D. J. Perreault. Very high frequency resonant boost converters. *38th IEEE Power Electronics Specialists Conf.*, pages 2718–2724, Jun. 2007.

[7] R. Pilawa-Podgurski. Design and evaluation of a very high frequency dc/dc converter. Master's thesis, Massachusetts Institute of Technology, Feb. 2007.

[8] W. Bowman, F. Balicki, F. Dickens, R. Honeycutt, W. Nitz, W. Strauss, W. Suiter, and N. Ziesse. A resonant dc-to-dc converter operating at 22 Megahertz. *3rd Annu. IEEE Applied Power Electronics Conf. and Expo.*, pages 3–11, Feb. 1988.

[9] A. Goldberg and J. Kassakian. The application of power MOSFETs at 10 MHz. *16th IEEE Power Electronics Specialists Conf.*, pages 91–100, Jun. 1985.

[10] R. Gutmann. Application of RF circuit design principles to distributed power converters. *IEEE Trans. Ind. Electron. Contr. Instrum.*, 27(3):156–164, Aug. 1980.

[11] D. Hamill. Class DE inverters and rectifiers for dc-dc conversion. *27th IEEE Power Electronics Specialists Conf.*, 1:854–860, Jun. 1996.

[12] J. Jóźwik and M. Kazimierczuk. Analysis and design of class-e^2 dc/dc converter. *IEEE Trans. Ind. Electron.*, 37(2):173–183, Apr. 1990.

[13] R. Redl and N. Sokal. A 14-MHz 100-watt class E resonant converter: principle, design considerations and measured performance. *17th IEEE Power Electronics Specialists Conf.*, pages 68–77, 1986.

[14] R. Redl, B. Molnar, and N. Sokal. Class E resonant regulated dc–dc power converters: analysis of operations and experimental results at 1.5 MHz. *IEEE Trans. Power Electron.*, PE-1(2):111–120, Apr. 1986.

[15] R. Steigerwald. A comparison of half-bridge resonant converter topologies. *IEEE Trans. Power Electron.*, 3(2):174–182, Apr. 1988.

[16] M. Albulet. *RF Power Amplifiers.* Noble, Atlanta, GA, 2001.

[17] S. El-Hamamsy. Design of high-efficiency RF class-D power amplifier. *IEEE Trans. Power Electron.*, 9(3):297–308, May 1994.

[18] S. Kee, I. Aoki, A. Hajimiri, and D. Rutledge. The class-E/F family of ZVS switching amplifiers. *IEEE Trans. Microw. Theory Tech.*, 51(6):1677–1690, Jun. 2003.

[19] H. Koizumi, T. Suetsugu, M. Fujii, K. Shinoda, S. Mori, and K. Iked. Class DE high-efficiency tuned power amplifier. *IEEE Trans. Circuits Syst. I*, 43(1):51–60, Jan. 1996.

[20] H. Krauss, C. Bostian, and F. Raad. *Solid-State Radio Engineering.* Wiley, New York, 1980.

[21] N. Sokal and A. Sokal. Class E-A new class of high-efficiency tuned single-ended switching power amplifiers. *IEEE J. Solid-State Circuits*, 10(3):168–176, Jun. 1975.

[22] V. Tyler. A new high-efficiency high-power amplifier. *Marconi Rev.*, 21(130):96–109, 1958.

[23] S. Zhukov and V. Kozyrev. Push-pull switching oscillator without commutating losses. *Poluprovodnikovye Pribory v. Tekh. Elektros.*, 15:95–107, 1975.

[24] R. Gutmann and J. Borrego. Power combining in an array of microwave power rectifiers. *IEEE Trans. Microw. Theory Tech.*, MTT-27(12):958–968, Dec. 1979.

[25] W. Nitz, W. Bowman, F. Dickens, F. Magalhaes, W. Strauss, W. Suiter, and N. Zeisse. A new family of resonant rectifier circuits for high frequency DC-DC converter applications. *3rd Annu. IEEE Applied Power Electronics Conf. and Expo.*, pages 12–22, 1988.

[26] Y. Han, O. Leitermann, D. Jackson, J. Rivas, and D. Perreault. Resistance compression networks for resonant power conversion. *36th IEEE Power Electronics Specialists Conf.*, pages 1282–1292, Jun. 2005.

[27] Y. Han, O. Leitermann, D. Jackson, J. Rivas, and D. Perreault. Resistance compression networks for radio-frequency power conversion. *IEEE Trans. Power Electron.*, 22(1):41–53, Jan. 2007.

[28] W. Everitt and G. Anner. *Communication Engineering*, chapter 13. McGraw-Hill Book Company, 3rd edition, 1956.

[29] C. Ruthroff. Some broad-band transformers. *IRE*, 48:1337–1342, 1959.

[30] J. Sevick. *Transmission line transformers.* Noble Publishing Associates, 4th edition, 2001.

[31] C. Trask. Designing wide-band transformers for HF and VHF power amplifiers. *QEX*, pages 3–15, Mar./Apr. 2005.

[32] W. Everitt and G. Anner. *Communication Engineering*, chapter 11. McGraw-Hill Book Company, 3rd edition, 1956.

[33] C. Bowick. *RF Circuit Design*, chapter 3. Newnes, London, UK, 1997.

[34] Y. Han and D. J. Perreault. Analysis and design of high efficiency matching networks. *IEEE Trans. Power Electron.*, 21(5):1484–1491, Sep. 2006.

[35] Y. Lee and Y. Cheng. A 580 KHz switching regulator using on-off control. *J. Inst. Electron. Rad. Eng.*, 57(5):221–226, Sep./Oct. 1987.

[36] J. Warren, III. Cell modulated dc/dc converter. Master's thesis, Massachusetts Institute of Technology, Sep. 2005.

[37] J. Warren, III, K. Rosowski, and D. J. Perreault. Transistor selection and design of a VHF DC-DC power converter. *IEEE Trans. Power Electron.*, 23(1):27–37, Jan. 2008.

[38] J. Rivas. *Radio frequency dc-dc power conversion.* PhD thesis, Massachusetts Institute of Technology, Sep. 2006.

[39] J. Rivas, D. Jackson, O. Leitermann, A. Sagneri, Y. Han, and D. Perreault. Design considerations for very high frequency dc-dc converters. *37th IEEE Power Electronics Specialists Conf.*, pages 2287–2297, Jun. 2006.

[40] J. Rivas, R. Wahby, J. Shafran, and D. Perreault. New architectures for radio-frequency DC-DC power conversion. *IEEE Trans. Power Electron.*, 21(2):380–393, Mar. 2006.

[41] A. Sagneri. Design of a very high frequency dc-dc boost converter. Master's thesis, Massachusetts Institute of Technology, Feb. 2007.

[42] J. Hu, A. Sagneri, J. Rivas, Y. Han, S. Davis, and D. Perreault. High frequency resonant SEPIC converter with wide input and output voltage ranges. *39th IEEE Power Electronics Specialists Conf.*, pages 1397–1406, Jun. 2008.

[43] J. Hu. Design of a low-voltage low-power dc-dc HF converter. Master's thesis, Massachusetts Institute of Technology, Feb. 2008.

[44] A. Shirvani, D. Su, and B. Wooley. A cmos RF amplifer with parallel amplification for efficient power control. *IEEE J. Solid-State Circuits*, 37(6):684–693, Jun. 2002.

[45] J. Rivas, O. Leitermann, Y. Han, and D. Perreault. A very high frequency dc-dc converter based on a class ϕ_2 resonant inverter. *39th IEEE Power Electronics Specialists Conf.*, pages 1657–1666, Jun. 2008.

[46] T. Lee. *The Design of CMOS Radio-Frequency Integrated Circuits*, chapter 3. Cambridge University Press, Cambridge, UK, 2nd edition, 2004.

[47] C. Sullivan, W. Li, S. Prabhakaran, and S. Lu. Design and fabrication of low-loss toroidal air-core inductors. *38th IEEE Power Electronics Specialists Conf.*, pages 1757–1759, Jun. 2007.

[48] W. Brown. The history of power transmission by radio waves. *IEEE Trans. Microw. Theory Tech.*, MTT-32(9):1230–1242, Sep. 1984.

[49] P. Godoy, D. Perreault, and J. Dawson. Outphasing energy recovery amplifier with resistance compression for improved efficiency. *IEEE Trans. Microw. Theory Tech.*, (In press).

[50] J. Phinney, J. Lang, and D. Perreault. Multi-resonant microfabricated inductors and transformers. *35th IEEE Power Electronics Specialists Conf.*, pages 4527–4536, Jun. 2004.

[51] M. Kazimierczuk and K. Puczko. Exact analysis of class E tuned power amplifier at any Q and switch duty cycle. *IEEE Trans. Circuits Syst.*, CS-34(2):149–159, Feb. 1987.

[52] D. Perreault, J. Rivas, Y. Han, and O. Leitermann. Resistance compression networks for resonant power conversion. US Patent No. 7,535,133, May 2009.

[53] E. Gilbert. Impedance matching with lossy components. *IEEE Trans. Circuits Syst.*, 22(2):96–100, Feb. 1975.

[54] L. Rade. *Mathematics Handbook for Science and Engineering*, page 49. Springer, New York, 5th edition, 2004.

[55] J. Rivas, Y. Han, O. Leitermann, A. Sagneri, and D. Perreault. A high-frequency resonant inverter topology with low-voltage stress. *IEEE Trans. Power Electron.*, 23(4):1759–1771, Jul. 2008.

[56] R. Frey. High voltage, high efficiency MOSFET rf amplifiers - design procedure and examples. Application Note APT0001, Advanced Power Technology, 2000.

[57] R. Frey. A push-pull 300-watt amplifier for 81.36 MHz. Application Note APT9801, Advanced Power Technology, 1998.

[58] R. Frey. 500w, class E 27.12 MHz amplifier using a single plastic MOSFET. Application Note APT9903, Advanced Power Technology, 1999.

[59] M. Iwadare and S. Mori. Even harmonic resonant class E tuned power amplifer without rf choke. *Electron. and Commun. in Japan (Part I: Commun.)*, 79(2):23–30, Jan. 1996.

[60] R. Pilawa-Podgurski, A. Sagneri, J. Rivas, D. Anderson, and D. Perreault. Very-high-frequency resonant boost converters. *IEEE Trans. Power Electron.*, 24(6):1654–1665, Jun. 2009.

[61] S. Ajram and G. Salmer. Ultrahigh frequency dc-to-dc converters using GaAs power switches. *IEEE Trans. Power Electron.*, 16(5):594–602, Sep. 2001.

[62] W. Tabisz and F. Lee. Zero-voltage-switching multi-resonant technique-a novel approach to improve performance of high frequency quasi-resonant converters. *19th IEEE Power Electronics Specialists Conf.*, pages 9–17, Apr. 1988.

[63] F. Lee. High-frequency quasi-resonant converter technologies. *Proceedings of the IEEE*, 76(4):377–390, Apr. 1988.

[64] J. Rivas, Y. Han, O. Leitermann, A. Sagneri, and D. Perreault. A high-frequency resonant inverter topology with low voltage stress. *38th IEEE Power Electronics Specialists Conf.*, pages 2705–2717, Jun. 2007.

[65] G. Bertotti. General properties of power losses in soft ferromagnetic materials. *IEEE Trans. Magn.*, 24(1):621–630, Jan. 1988.

[66] J. Goodenough. Summary of losses in magnetic materials. *IEEE Trans. Magn.*, 38(5):3398–3408, Sep. 2002.

[67] W. Roshen. A practical, accurate and very general core loss model for nonsinusoidal waveforms. *IEEE Trans. Power Electron.*, 22(1):30–40, Jan. 2007.

[68] J. Li, T. Abdallah, and C. Sullivan. Improved calculation of core loss with nonsinusoidal waveforms. *36th Annual Meeting of IEEE Industry Applications Society*, 4:2203–2210, Sep./Oct. 2001.

[69] K. Venkatachalam, C. Sullivan, T. Abdallah, and H. Tacca. Accurate prediction of ferrite core loss with nonsinusoidal waveforms using only steinmetz parameters. *2002 IEEE Workshop on Computers in Power Electronics*, pages 36–41, Jun. 2002.

[70] A. Goldberg. *Development of magnetic components for 1-10 MHz dc/dc converters.* PhD thesis, Massachusetts Institute of Technology, Sep. 1988.

[71] IEEE standard for test procedures for magnetic cores. Standard 393-1991, IEEE, Mar. 1992.

[72] Cores made of soft magnetic materials–measuring methods. International Standard 62044-1, IEC, 2002-2005.

[73] T. Simpson. Effect of a conducting shield on the inductance of an air-core solenoid. *IEEE Trans. Magn.*, 35(1):508–515, Jan. 1999.

[74] T. Lee. *Planar Microwave Engineering: A Practical Guide to Theory, Measurement, and Circuits*, chapter 6. Cambridge University Press, 2004.

[75] R. Erickson and D. Maksimović. *Fundamentals of Power Electronics*, chapter 14. Springer Science and Business Media Inc., 2nd edition, 2001.

[76] R. Erickson and D. Maksimović. *Fundamentals of Power Electronics*, chapter 15. Springer Science and Business Media Inc., 2nd edition, 2001.

[77] C. Sullivan. Optimal choice for number of strands in a litz-wire transformer winding. *IEEE Trans. Power Electron.*, 14(2):283–291, Mar. 1999.

[78] N. Kutkut and D. Divan. Optimal air-gap design in high-frequency foil windings. *IEEE Trans. Power Electron.*, 13(5):942–949, Sep. 1998.

[79] R. Jensen and C. Sullivan. Optimal core dimensional ratios for minimizing winding loss in high-frequency gapped-inductor windings. *18th Annu. IEEE Applied Power Electronics Conf. and Expo.*, pages 1164–1169, Feb. 2003.

[80] J. Hu and C. Sullivan. Optimization of shapes for round-wire high-frequency gapped-inductor windings. *33th Annual Meeting of IEEE Industry Applications Society*, pages 907–911, Oct. 1998.

[81] J. Hu and C. Sullivan. Analytical method for generalization of numerically optimized inductor winding shapes. *30th IEEE Power Electronics Specialists Conf.*, pages 568–573, Jun. 1999.

[82] W. Hurley, E. Gath, and J. Breslin. Optimizing the ac resistance of multilayer transformer windings with arbitrary current waveforms. *IEEE Trans. Power Electron.*, 15(2):369–376, Mar. 2000.

[83] J. Hu and C. Sullivan. AC resistance of planar power inductors and the quasidistributed gap technique. *IEEE Trans. Power Electron.*, 16(4):558–567, Jul. 2001.

[84] Y. Han, G. Cheung, A. Li, C. Sullivan, and D. Perreault. Evaluation of magnetic materials for very high frequency power applications. *39th IEEE Power Electronics Specialists Conf.*, pages 4270–4276, Jun. 2008.

[85] W. Odendall and J. Ferreira. Effects of scaling high-frequency transformer parameters. *IEEE Trans. Ind. Applicat.*, 35(4):932–940, Jul./Aug. 1999.

[86] J. Reinert, A. Brockmeyer, and R. De Doncker. Calculation of losses in ferro- and ferrimagnetic materials based on the modified steinmetz equation. *IEEE Trans. Ind. Applicat.*, 37(4):1055–1061, Jul./Aug. 2001.

[87] C. Xiao. *An investigation of fundamental frequency limitations for HF/VHF power conversion.* PhD thesis, Virginia Polytechnic Institute and State University, Jul. 2006.

[88] W. Gu and R. Liu. A study of volume and weight vs. frequency for high-frequencytransformers. *24th IEEE Power Electronics Specialists Conf.*, pages 1123–1129, Jun. 1993.

[89] M. Nigam and C. Sullivan. Multi-layer folded high-frequency toroidal inductor windings. *23th Annu. IEEE Applied Power Electronics Conf. and Expo.*, pages 682–688, Feb. 2008.

[90] P. Dowell. Effects of eddy currents in tranformer windings. *Proc. IEE*, Aug.(113):1387–1394, 1966.

[91] J. Spreen. Electrical terminal representation of conductor loss in transformers. *IEEE Trans. Power Electron.*, 5:424–429, Oct. 1990.

[92] A. Rand. Inductor size vs Q: A dimensional analysis. *IEEE Trans. Compon. Parts*, pages 31–35, 1963.

[93] W. Shen, F. Wang, D. Boroyevich, and C. Tipton. Loss characterization and calculation of nanocrystalline cores for high-frequency magnetics applications. *IEEE Trans. Power Electron.*, 23:475–484, Jan. 2008.

[94] T. Nakamura. Snoek's limit in high-frequency permeability of polycrystalline Ni-Zn, Mg-Zn, and Ni-Zn-Cu spinel ferrites. *Journal of Applied Physics*, 88:348–353, Jul. 2000.

[95] W. Odendaal and J. Ferreira. A thermal model for high-frequency magnetic components. *IEEE Trans. Ind. Applicat.*, 35:924–931, Jul/Aug 1999.

[96] R. Browne, S. Hann, J. Klaassens, J. Lodder, and D. Verheul. Computer-aided design of toroidal air-core inductors for high energy levels. *IEEE Trans. Ind. Electron.*, 35(2):329–337, May 1988.

[97] P. Murgatroyd. The optimal form of coreless inductors. *IEEE Trans. Magn.*, 25(3):2670–2677, May 1989.

[98] V. Ermolov, T. Lindstrom, H. Nieminen, M. Olsson, M. Read, T. Ryhanen, S. Silanto, and S. Uhrberg. Microreplicated rf toroidal inductor. *IEEE Trans. Microw. Theory Tech.*, 52(1):29–37, Jan. 2004.

[99] C. Steinmetz. On the law of hysteresis. *Proc. of the IEEE*, 72:197–221, Feb. 1984.

[100] R. Erickson and D. Maksimović. *Fundamentals of Power Electronics*, chapter 13. Springer Science and Business Media Inc., 2nd edition, 2001.

[101] S. Mulder. Power ferrite loss formulas for transformer design. *Power Conversion and Intelligent Motion*, 21(7):22–31, July 1995.

[102] E. Snelling. *Soft ferrites, properties and applications.* Butterworths, 2nd edition, 1988.

[103] M. Albach, T. Durbaum, and A. Brockmeyer. Calculating core losses in transformers for arbitrary magnetizing currents a comparison of different approaches. *27th IEEE Power Electronics Specialists Conf.*, 2:1463–1468, Jun. 1996.

[104] A. Brockmeyer. *Dimensionierungswekzeug f"ur magnetische Bauelemente in Stromrichteranwendungen.* PhD thesis, Aachen University of Technology, 1997.

[105] R. Medhurst. H.f. resistance and self-capacitance of single-layer solenoids. *Wireless Engineer*, pages 35–43, Mar. 1947.

[106] R. Medhurst. Q of solenoid coils. *Wireless Engineer*, page 281, Sep. 1947.

[107] M. Callendar. Q of solenoid coils. *Wireless Engineer (Correspondence)*, page 185, Jun. 1946.

[108] I. Aoki, S. Kee, D. Rutledge, and A. Hajimiri. Distributed active transformer-a new power-combining and impedance-transformation technique. *IEEE Trans. Microw. Theory Tech.*, 50:316–331, Jan. 2002.

[109] I. Aoki, S. Kee, D. Rutledge, and A. Hajimiri. Fully integrated CMOS power amplifier design using the distributed active-transformer architecture. *IEEE J. Solid-State Circuits*, 37(3):371–383, Mar. 2002.

[110] A. Sagneri, D. Anderson, and D. Perreault. Transformer synthesis for VHF converters. *2010 International Power Electronics Conference*, (submitted).